Photoluminescence Quenching and Location Estimation of InGaAs/GaAs Quantum Dots under Nanoprobe Indentation

(InGaAs/GaAs 量子ドットのナノインデンテーションによる発光停止と位置推定)

2010 年 9 月

埼玉大学大学院理工学研究科 (博士後期課程)

人間支援・生産科学コース (主指導教官 荒居 善雄)

徐 利 霞

Photoluminescence Quenching and Location Estimation of InGaAs/GaAs Quantum Dots under Nanoprobe Indentation

By

Lixia Xu

A dissertation submitted in partial fulfillment of the requirement for the degree of Doctor of Philosophy

Examining Committee:

Prof. Yoshio ARAI
Dr. Kazunari OZASA
Prof. Wakako ARAKI
Prof. Kenichiro HORIO
Prof. Kensuke KAGEYAMA

Doctor Course in Production Science
Graduate School of Science and Engineering
Saitama University
Japan

September 2007

CONTENTS

ABSTRACT

In this thesis, the low-temperature (10 K) photoluminescence (PL) of self-assembled InGaAs/GaAs quantum dots (QDs) was studied under the elastic indentation of a flat cylindrical or dome-shaped nanoprobe that generates localized strain fields around itself. As the indentation force increases with the flat cylindrical nanoprobe indented at a fixed position, the intensity of the enhanced fine PL peak from a single QD was observed to firstly increase, followed by a decrease, and be finally quenched, while the energy of the PL peak was linearly blueshifted with the force. The PL peak energy shift per unit force, i.e., the blueshift rate, was measured in the range from 22.7 to 87.8 meV/mN. The observed force at which a PL peak disappears, i.e., the quenching force varies from QD to QD. This variation is ascribed to the diversely distributed strain fields in and around each QD and therefore can be related to the QD location with respect to the nanoprobe center. In the case of using the dome-shaped nanoprobe for the indentation with a horizontal scan, the PL emissions from some of observed QDs were firstly blueshifted then symmetrically redshifted with the movement of the probe position during the scan. This symmetric blue- and red-shift was not observed in the indentation of scan of the flat cylindrical probe.

In order to clarify the mechanism of PL quenching and the influence of probe tip shape on the PL emissions from QDs, a numerical simulation of the strain distribution is carried out by a 3-dimensional finite element method, depending on the shape of nanoprobe used in the experiments. The modification of the energy band structure resulting from strain is then calculated based on the deformation potential theory.

With a quantitative relationship between the blueshift rate and the QD's distance from the probe center, derived from the simulation, we proposed a method to estimate the location of the embedded QDs from the experimentally measured blueshift rate. The observed QDs were determined to be located around the nanoprobe edge, which coincides with the observation that only the PL emitted from the QDs located under the probe edge is enhanced and observable under nanoprobe indentation. The estimation method presented in this study provides a reliable and simple way to estimate the location of the embedded QDs with respect to the probe center by nanoprobe indentation.

Based on the estimation of the locations of QDs under the indentation of the flat cylindrical nanoprobe, the observed PL quenching was analyzed quantitatively to be ascribed

to two possible mechanisms, the crossover between the Γ and X or L band of InGaAs and the electron-repulsion resulting from the strain-induced potential gradient. The crossover between the Γ and X or L band of InGaAs was deduced to be possible only on the basis of assuming low X or L band gap energy of InAs and high bowing parameter for the X or L band gap energy of InGaAs. On the other hand, if the electron-repulsion resulting from the strain-induced potential gradient was responsible for the PL quenching, an indentation-induced potential height at quenching was derived to be from 43.5 to 133.5 meV.

Calculations in the case of dome-shaped nanoprobe have shown that the change in the probe tip shape modified the generated strain field in and around single QD, thus resulting in the different behavior of PL emissions observed in the indentation experiments. With the PL results from the indentation of scan of dome-shaped probe, the locations of those QD, whose PL emissions exhibited symmetric blue- and red-shift, were directly obtained from the experiment at which the PL emissions from those QDs reached the maximum values. This is an advantageous improvement in the estimation of the location of embedded QDs achieved by using the dome-shaped probe, which can not be realized in the case of flat cylindrical probe.

Acknowledgements

My doctoral study at Saitama University will soon come to an end, and at the completion of my doctoral thesis: I wish to express my sincere appreciation to all those who have offered me invaluable help during my three years of stay in Saitama University in Japan.

Firstly, I would like to express my heartfelt gratitude to my supervisors, Prof. Yoshio ARAI and Dr. Kazunari OZASA, for their constant encouragement and guidance whether during the study or in daily life. They have walked me through all the stages of the completion of the doctoral study. Without their consistent and illuminating instructions, this thesis could not have been possible. Equal appreciation should also be given to Prof. Wakako ARAKI and Dr. Toyomi UCHIYAMA for their valuable suggestions and generous help in the study and daily life.

Secondly, I should give my hearty thanks to the frontier research program at RIKEN, at where I performed all the experiments.

Thirdly, I really appreciate my dissertation committee members, Prof. Kenichiro HORIO and Prof. Kensuke KAGEYAMA, for their patient review of this thesis and their precious comments.

I also would like to express my sincere thanks to the members of strength of materials laboratory, especially Dr. Yuan-hua Liang, Mr. Hiroki Kakoi, and Mr. Ogawa. Thanks them for their help during the study.

The completion of my doctoral study in Japan can not be achieved without the help from all my dear friends. Special thanks should be given to my supervisors in master degree, Prof. Yi Huang, and Prof. Gang Liu. Without their help and encouragement, the dream to achieve a foreign doctoral degree could not come true.

I also gratefully acknowledge the financial support from the Ministry of Education, Science, Sports and Culture from Japan Government during the three years.

Lastly, my thanks would go to my beloved family especially my boyfriend Mr. Bo Wang for their loving considerations and great confidence in me all through these years. Thank you all so much being my supports all the time.

List of Figures

List of Tables

List of Symbols

Symbol	Definition
a_c	Γ-conduction band component of hydrostatic deformation potential
a_{GaAs}	Lattice constant of GaAs
$a_{In_{0.52}Ga_{0.48}As}$	Lattice constant of $In_{0.52}Ga_{0.48}As$
a_v	Valence band component of hydrostatic deformation potential
b	Biaxial deformation potential
c_{11}, c_{12}, c_{44}	Elastic constants of materials
d	Shear deformation potential, or the distance from the QD center to the probe center
E	Young's modulus
E_g^L	L-band gap energy
E_g^X	X-band gap energy
E_g^Γ	Γ-band gap energy
$\overline{E}_g$	Photon energy measured in the PL
F	Indentation force
F_q	Quenching force
H_ε^v	Strained Hamiltonian of the valence band
L	Bottom length of dome-shaped nanoprobe
P_ε	Element in the strained Hamiltonian, $P_\varepsilon = a_v\left(\varepsilon_{xx}+\varepsilon_{yy}+\varepsilon_{zz}\right)$
Q_ε	Element in the strained Hamiltonian, $Q_\varepsilon = b\left[\varepsilon_{zz}-\frac{1}{2}\left(\varepsilon_{xx}+\varepsilon_{yy}\right)\right]$
R	Radius of flat cylindrical nanoprobe
r	Radius of dome-shaped nanoprobe
R_ε	Element in the strained Hamiltonian, $R_\varepsilon = \frac{\sqrt{3}}{2}b\left(\varepsilon_{xx}-\varepsilon_{yy}\right)-id\varepsilon_{xy}$
S_ε	Element in the strained Hamiltonian, $S_\varepsilon = -d\left(\varepsilon_{zx}-i\varepsilon_{yz}\right)$
V_0	Volume of single QD or surrounding GaAs

VBO	Valence band offset between InGaAs and GaAs
x	The first variable in the Cartesian coordinate, the x value of the probe indentation position
x'	The x' value of QD location relative to the center of nanoprobe
y	The second variable in the Cartesian coordinate, the y value of the probe indentation position
y'	The y' value of QD location relative to the center of nanoprobe
z	The third variable in the Cartesian coordinate, the z value of the probe indentation position
z'	The z' value of QD location relative to the center of nanoprobe
ε_{h}	Hydrostatic strain, $\varepsilon_{\mathrm{h}} = \varepsilon_{xx} + \varepsilon_{yy} + \varepsilon_{zz}$
$\overline{\varepsilon}_{\mathrm{h}}$	Volume averaged hydrostatic strain
ε_{ij}	Strain components, i, j take x, y, z
$\overline{\varepsilon}_{ij}$	Strain components based on the volume averaging
ε_{ij}^{*}	Eigenstrain due to lattice mismatch
ε_{s}	Biaxial strain, $\varepsilon_{\mathrm{s}} = \varepsilon_{zz} - \left(\varepsilon_{xx} + \varepsilon_{yy}\right)/2$ when the x, y axes are taken as the biaxial strain axes
$\overline{\varepsilon}_{\mathrm{s}}$	Volume averaged biaxial strain
υ	Poisson's ratio
Δ_0	Spin-orbit splitting energy
$\Delta E_{\mathrm{c}}^{L}$	Energy shift of L-conduction band due to strain
$\Delta E_{\mathrm{c}}^{X}$	Energy shift of X-conduction band due to strain
$\Delta E_{\mathrm{c}}^{\Gamma}$	Energy shift of Γ-conduction band due to strain
$\Delta E_{\mathrm{g}}^{\Gamma}$	Energy shift of Γ-band gap due to strain
$\Delta E_{\mathrm{v}}^{\Gamma}$	Energy shift of valence band due to strain
$\Delta \overline{E}_{(\mathrm{c,v,g})}^{(\Gamma,X,L)}$	Energy shifts of the Γ-, X-, and L- conduction band, valence band and band gap based on volume-averaging
$\Delta \overline{E}_{\mathrm{g}} / \Delta F$	Blueshift rate of QD, shift of PL peak energy per unit force

θ	The angle of the QD center relative to the x' axis
Ξ_d^L	Hydrostatic deformation potential for the L-conduction band
Ξ_u^L	Shear deformation potential for the L-conduction band
Ξ_d^X	Hydrostatic deformation potential for the X-conduction band
Ξ_u^X	Biaxial deformation potential for the X-conduction band

List of Publications

Journal Papers:

1. Kazunari Ozasa, Mizuo Maeda, Masahiko Hara, Hiroki Kakoi, **Lixia Xu**, Yuan-hua Liang, and Yoshio Arai, "Direct-to-indirect transition observed in quantum dot photoluminescence with nanoprobe indentation", **Journal of Vacuum Science Technology B** 27(2), 934-938 (2009).
2. **Lixia Xu**, Yoshio Arai, Kazunari Ozasa, Hiroki Kakoi, Yuan-hua Liang, and Wakako Araki, "Estimation of the location of embedded InGaAs/GaAs quantum dots by measuring strain-induced blueshift of photoluminescence", **Physica E** 42, 2441-2445 (2010).

International Conferences:

1. Kazunari Ozasa, Mizuo Maeda, Masahiko Hara, Hiroki Kakoi, **Lixia Xu**, Yuan-hua Liang, and Yoshio Arai, "Gamma-X Crossover Observed in Quantum Dot Photoluminescence by Nanoprobe Indentation", International Conference on Nanoscience + Technology (ICN+T), Keystone, Colorado *USA*, July 20-25, 2008.
2. **Lixia Xu**, Kazunari Ozasa, Hiroki Kakoi, Yuan-hua Liang, Yoshio Arai, and Wakako Araki, "Gamma-X crossover in InGaAs/GaAs quantum dots due to the indentation of a flat cylindrical nanoprobe", The 14th International Conference on Modulated Semiconductor Structure (MSS-14), Kobe Japan, July 19-24, 2009.
3. **Lixia Xu**, Takahiro Ogawa, Wakako Araki, Yoshio Arai, Kazunari Ozasa, Mizuo Maeda, and Masahiko Hara, "Estimation of the location of embedded InGaAs/GaAs quantum dots by measuring the photoluminescence under nanoprobe indentation", The 6th International Conference on Quantum Dots (Quantum Dot 2010), East Midlands Conference Centre, Nottingham UK, April 26-30, 2010.

Domestic Conferences:

1. 尾笹一成, 前田瑞夫, 原正彦, 栂井洋希, **Lixia Xu**, Yuan-hua Liang, 荒居善雄, "ナノプローブ歪による InGaAs 量子ドットの間接遷移化", 日本物理学会第 64 回年次大会，池袋 日本，3 月 27 日-30 日，2009.

Chapter 1
Introduction

1.1 Self-assembled quantum dots

1.1.1 Quantization of quantum dots

A semiconductor quantum dot (QD) is made up of a small volume of one semiconductor material, with dimensions typically a few nanometers, buried with a second semiconductor material. Usually, the quantum dot material has the band gap be much narrower than that of the matrix material. The semiconductor quantum dots, together with the semiconductor wires and wells, and a variety of materials with reduced geometry, such as nanocrystals and clusters, nanotubes, nanoropes, nanoribbons and etc., constitute the family of nanostructures. They can be free standing, capped by protective layers, or embedded in matrices.

The most significant characteristic of the nanostructures (including quantum dots) is the effect of size quantization, which controls most of the properties of nanostructures and their devices, including electronic, magnetic, optical, transport, superconductive, ferroelectric, and electron-lattice properties. A focused interest in understanding the nanostructures is to modify the structures so that they can have the properties unavailable in the bulk materials using the quantization effect. In a quantum dot (zero-dimensional nanostructure), the particles, including the electrons in the conduction bands and the holes in the valence bands, are confined in all three dimensions, resulting in the different behaviors of these particles from those in the bulk material. Generally, the size of quantum dots is from several to 100 nanometers, depending on the type of quantum dot and the fabrication processing. Since the size of quantum dots is comparable to the carrier de Broglie wavelength, the quantization effect dominates in the quantum dot. Considering a *quantum box* with an infinite potential separation between the inside of the box and the outside, solving the Schrodinger equation gives the discrete confinement energy within this quantum box as [1]:

$$E_j = \frac{\pi^2\hbar^2}{2m^*}\left(\frac{n_x^2}{L_x^2}+\frac{n_y^2}{L_y^2}+\frac{n_z^2}{L_z^2}\right),\quad n_{x,y,z}=1,2,3...,\quad j=0,1,2..., \tag{1.1}$$

where L_x, L_y, and L_z are the lengths of the quantum box, and m^* is the effective mass of

the carrier. The energy level corresponding to $n_x = n_y = n_z = 1$ is the ground state energy level E_0.

In addition to causing the discrete energy levels in the quantum dot, the quantization effect also changes the number of electronic states available per unit energy, i.e. density of states (DOS), which is defined by

$$\rho(E) = \mathrm{d}n(E)/\mathrm{d}E, \tag{1.2}$$

where $n(E)$ is the number of electronic states at the energy level of E. For a bulk semiconductor, the DOS can be expressed as [2]

$$\rho(E) = g_s g_v \frac{(2m^*)^{3/2}}{4\pi^2\hbar^3} E^{1/2}, \tag{1.3}$$

where $g_s = 2$ is the spin degeneration, g_v is the valley degeneration, and m^* is the effective mass of the carrier. In a semiconductor quantum well (QW) (two-dimensional nanostructure), the carriers are confined in the z-direction perpendicular to the well interface, there thus are several quantized energies E_n along the z-direction. The DOS for the n[th] subband is then [2]:

$$\rho(E) = g_s g_v \frac{m^*}{2\pi\hbar^2} \sigma(E - E_{2n}), \tag{1.4}$$

where $\sigma(E - E_{2n})$ is a step function. In a semiconductor quantum wire (one-dimensional nanostructure), where the carriers are confined in two directions, the DOS for the n[th] subband is [2]

$$\rho(E) = g_s g_v \frac{m^*}{\pi\hbar^2} \left[\frac{h^2}{2m^*(E - E_{1n})} \right]^{1/2} \sigma(E - E_{1n}). \tag{1.5}$$

In a semiconductor quantum dot (QD) (zero-dimensional nanostructure), the carriers are confined in all three directions, and the energy levels are discrete in all three directions. The three-dimensional confinement gives a discrete delta-function-like DOS, which is given by [2]:

$$\rho(E) = g_s g_v \sum_{n=n_x,n_y,n_z} \delta(E - E_{0n}). \tag{1.6}$$

The density of states (DOS) for bulk material, a quantum well, a quantum wire, and a quantum dot are shown in Fig. 1.1.

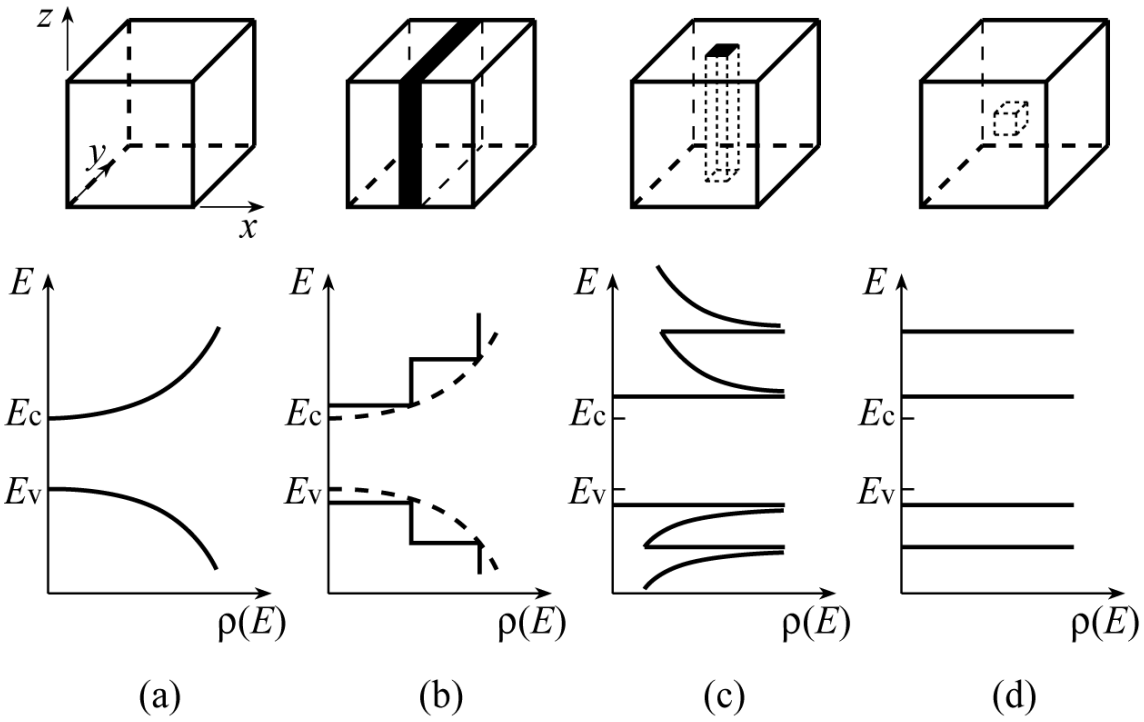

FIG. 1.1 Comparison of the quantization of density of states: (a) bulk, (b) quantum well, (c) quantum wire, (d) quantum dot. Top row: schematic morphology, bottom row: density of electronic states.

Because of the discrete energy levels and a consequent discrete density of states in the dot, the electronic structure of the quantum dots is totally different from that of a bulk semiconductor. In a bulk semiconductor, the absorption of radiation by the semiconductor will not take place until the energy is equal or larger than the band-gap energy of the material ($h\upsilon \geq E_g$). This is because the electrons must absorb enough energy (at least E_g) to be excited from somewhere in the valence band to somewhere in the conduction band. A continuum of allowed states within the valence and conduction bands allows absorption to continue at higher radiation energies. The transition from no absorption to complete absorption would be expected to be very sharp, since there are no allowed states in the band gap under ideal conditions. However, this transition is not as sharp as expected, because of the impurities and defects in the semiconductor which cause trap states and surface states within the band gap, as shown in Fig. 1.2 (a). Figure 1.2 (b) illustrates the energy band structure of a

semiconductor quantum dot. Because of the electronic confinement by the dot, discrete energy levels (E_{c0}, E_{c1}, ... for confined electrons, E_{v0}, E_{v1}, ... for confined holes) are formed within the dot. In other words, the electrons/holes can only be stable in the dot at discrete energy levels. This makes the incident radiation must have the energy equal to the separation between discrete states to excite the electrons/holes from one state to another, or the recombination of electrons and holes can only emit the photon with the energy equal to the difference between the discrete energy levels of conduction and valence band, as shown in Fig. 1.2 (b).

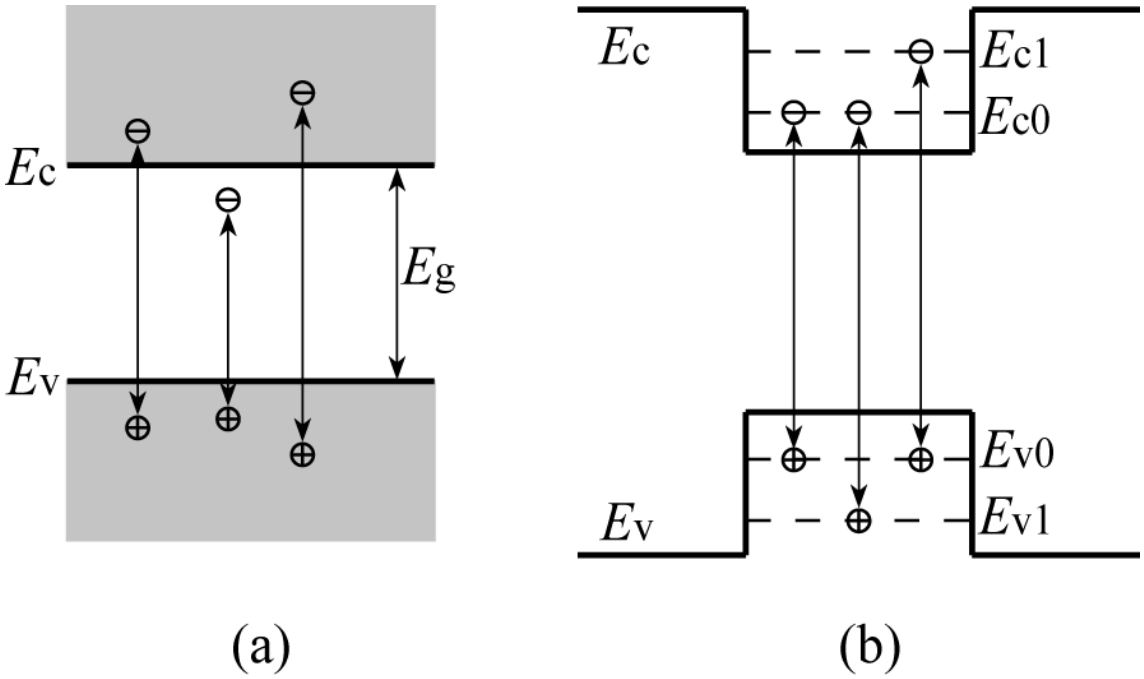

FIG. 1.2 Electronic structure of (a) bulk semiconductor and (b) a semiconductor quantum dot

As described above, the energy levels in the quantum dots are discrete due to the three-dimensional confinement, resulting that the physical properties of QDs in many respects resemble those of an atom. The atom-like discrete energy levels in the dots make the QDs be beneficial for applications involving the detection or emission of light. The discrete energy levels existing in the QD allow only electrons/holes of certain discrete energies to exist. This means photodetectors can be fabricated using QDs that will be sensitive to a very narrow linewidth of light. Similarly, this means lasers can be fabricated outputting light with a very fine linewidth. Nowadays, the semiconductor quantum dots have been widely applied in

quantum dot laser [3-5], quantum dot infrared photodetector [6-8], single electron transistor [9], evident tags in biotechnology and life science [10, 11], superior anti-counterfeiting device, quantum communication and computing [12] and etc.

In order to make the quantum dots applicable in the detection or emission devices as mentioned above, i.e. ensuring the quantization effect, the quantum dots should fulfill the following requirements:

(a) Appropriate QD size, to provide sufficiently deep confined energy levels with sufficient separation between different discrete states;

(b) High uniformity, to narrow the inhomogeneous energetic broadening for fine performance of QD-based devices;

(c) Coherent materials of dot and matrix without defects.

(a) QD size

There are both lower and higher limits for the QD size. The lower limit of the QD size is given by the condition that at least one energy level of an electron or hole or both should be present in the dot. Assuming a spherical QD, the critical diameter $D_{\min}$ is given by [13]

$$D_{\min} = \frac{\pi\hbar}{\sqrt{2m_e^*\Delta E_c}}, \tag{1.7}$$

where m_e^* is the effective mass of electron, and ΔE_c is the band offset of the conduction bands. If the diameter of the spherical QD is equal or slightly larger than the critical diameter $D_{\min}$, the separation between the confined electron energy level and the barrier energy is very small. As a result, the electrons confined in the dot will deplete induced by the thermal evaporation at finite temperatures. Taking the GaAs/$Al_{0.4}Ga_{0.6}As$ heterostructure (with a conduction band offset ~0.3 eV) as an example, the diameter of the spherical QD should be larger than 4 nm.

The higher limit of the QD size is that the separation between the neighboring discrete energy levels should be sufficiently large, to prevent the carriers from jumping between different energy levels because of thermal evaporation. If electron levels are considered, the upper limits of the sizes of GaAs/AlGaAs QDs and InAs/AlGaAs QDs are approximately 12 nm and 20 nm, respectively.

(b) Uniformity

The degree of the uniformity of the QDs' size, shape, and chemical composition determines the degree of the variation of the energy levels. Such variation is typically Gaussian. For a device such as a quantum dot laser, which relies on the integrated gain in a narrow energy range, the inhomogeneous energetic broadening should be as small as possible. In other words, one needs to ensure the smallest possible size and shape dispersion values for a given average size of the QDs.

(c) Material quality

The density of defects, such as dislocation, in a QD material and its interface to the surrounding matrix should be as low as possible. QD fabrication using self-assembled growth seems to be predestined to achieve this goal.

1.1.2 Self-organization of quantum dots

As described in Sec. 1.1.1, the most significant and advantageous characteristic of quantum dots is the effect of quantization, to realize which the size of the QD must be limited to a scale of nanometer. This limitation proposed a challenging task to the semiconductor researchers that new methods had to be developed to fabricate such small structures. To a certain extent, the development history of the fabrication technique of nanostructures is the development history of the QDs and QD-based devices.

By the end of the 1980's, the most straightforward way to fabricate a quantum dot is to cut a quantum well into separated boxes with nanoscale, i.e. patterning of quantum wells. At that time, the scientists had succeeded in fabricating semiconductor layers (quantum wells) having atomic scale precision in width [14], with the development of the advanced crystal growth methods, such as Molecular Beam Epitaxy (MBE) and Metal-Organic Chemical Vapor Deposition (MOCVD). Till now, patterning still attracts much attention because of its advantages in controlling the QDs' shape, size and arrangement and in applying a variety of processing techniques.

In the last few years, quantum dots have been successfully realized using self-organization effects, i.e. self-assembled quantum dots. Nowadays, a main part of the research on quantum dots is performed on this type of dots. The self-assembled formation can be briefly expressed as: under certain growth conditions, when a thin layer of a semiconductor

is grown on top of a substrate which has a different lattice constant, then in attempt to minimize the total strain energy between the bonds, the thin layer spontaneously *self-assembles*/*self-organizes*/*self-orders* into quantum dots. Since the InGaAs/GaAs QDs researched in this thesis is formed by the self-organization, we will briefly introduce the growth modes of the self-organized heterostructures in the following.

There are three well-known modes of heteroepitaxial growth: Frank-van der Merwe (1949), Volmer-Weber (1926) and Stranski-Krastanow (1937). They represent layer-by-layer growth (FvdM, 2D), island growth (VW, 3D), and layer-by-layer followed by 3D islands (SK). These growth modes are deduced from equilibrium considerations of the surface and interface energies for lattice matched/mismatched systems. Figure 1.3 illustrates these three growth modes. Which one of these growth modes will dominate in the epitaxial growth depends on the material system used and on the growth conditions. In general, the FvdM mode occurs most often for the lattice-matched combination of semiconductor materials with a high deposition temperature. If the deposited semiconductor is slightly mismatched to the substrate semiconductor, SK growth mode dominates in the process. For highly mismatched combinations of semiconductor materials, the deposited material often crystallizes in the VW mode.

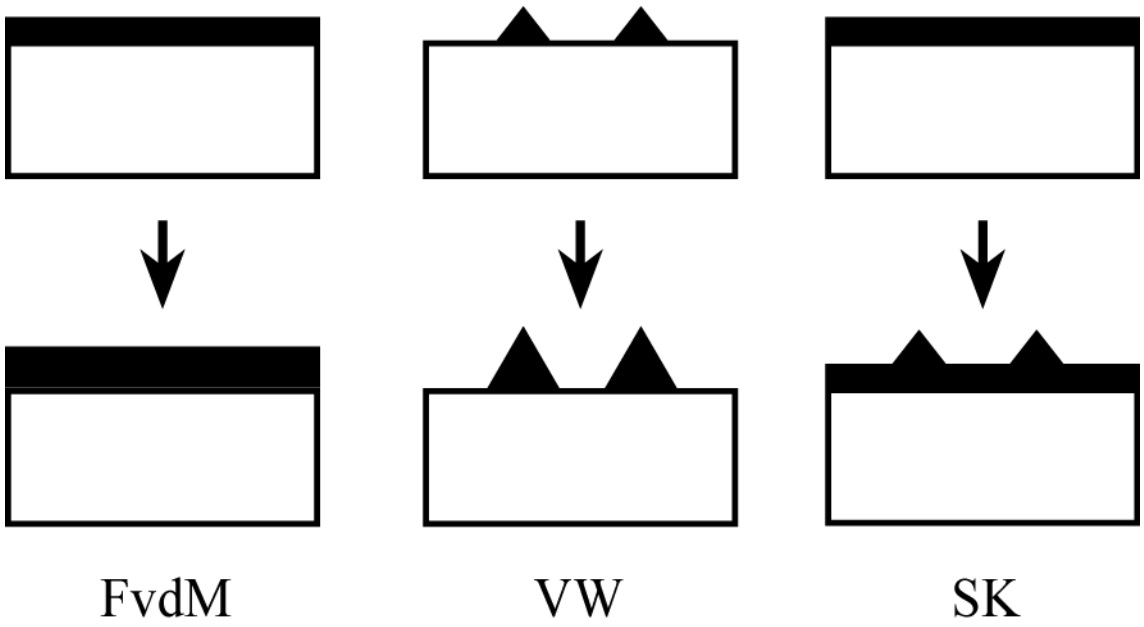

FIG. 1.3 Schematic diagrams of the three growth modes: Frank-van der Merwe (FvdM), Volmer-Weber (VW), and Stranski-Krastanow (SK).

Considering the self-assembled InGaAs/GaAs QDs under investigation in this thesis, the SK mode occurs in the epitaxial growth. Since the lattice constant of InGaAs is larger than that of GaAs (unstrained InAs of 6.0583 Å, unstrained GaAs of 5.6533 Å), the InGaAs, in order to fit onto the substrate of GaAs, is compressively strained with biaxial strain fields created during the deposition. The built-up strain/stress makes the InGaAs two-dimensional growth to be unstable, as the thickness of deposited layer increases. When the layer thickness increases up to a *critical layer thickness*, the two-dimensional growth of InGaAs layer is deteriorated. Then, the instability of the two-dimensional layer growth may be relaxed by the formation of *misfit dislocation* [15]. However, it is recognized that these layers are unstable against shape changes [16], while they are metastable against the formation of dislocations [17]. In other words, the strained layers prefer to relief their stress by the formation of quantum dots to the formation of misfit dislocation in the lattice. Microscopy has shown that the dots take the shape of pyramids, or square based 'tetrahedron' [18, 19] in the self-organization mode. The formation of 3D islands of QDs reliefs the strains in and around the dots, resulting in a decrease in the total energy of the strained epilayer/substrate system, and therefore makes the formation of coherent islands on an initially flat heteroepitaxial surface to be possible and stable.

Based on the growth modes mentioned above (FvdM, VM, and SK modes), various techniques, such as Molecular Beam Epitaxy (MBE), Metal-Organic Chemical Vapour Deposition (MOCVD) (with alternative name of Metal-Organic Vapour Phase Epitaxy (MOVPE)), Chemical Beam Epitaxy (CBE), Liquid Phase Epitaxy (LPE) and etc., have been well developed in recent years to fabricate low-dimensional nanostructures (such as quantum dots). Experiments have shown that the size, shape and density of the quantum dots are less dependent on the mismatch than on the deposition conditions[20]. The density of dots increases with both decreasing temperature and increasing growth rate or deposited amount. The size of dots is mainly controlled by the strain field around the dots, increase in the strain filed increasing dot size. Considering this strain field as a barrier preventing the material from diffusing towards the dots, the smaller dots will be favored to grow faster than the larger ones, thus narrowing the size distribution.

1.1.3 Observation and measurement of quantum dots

Besides the fabrication method, another challenge for the research of quantum dots is to observe/measure the physical, electronic, and optical properties of quantum dots in such a small scale. The primary observation/measurement methods can be divided into three types. The first type is *direct imaging* methods, such as scanning tunneling microscopy (STM), atomic force microscopy (AFM), transition electron microscopy (TEM), and scanning transition electron microscopy. The second type is *diffraction* methods, such as reflective high-energy electron diffraction (RHEED), reflectance anisotropy spectroscopy (RAS), and X-ray diffraction (XRD). The third type is *optical* methods, such as photoluminescence spectroscopy (PL), near-field scanning optical microscopy (NSOM), cathodeluminescence (CL), and scanning tunneling luminescence (STL).

The *direct imaging* and *diffraction* methods are widely used to investigate the physical characterization of QDs, such as the QDs size, shape, density, spatial homogeneity, and array ordering. The STM together with the AFM technique provide a spatial resolution at an atomic level, and therefore are favored by the scientists as the first choices to observe the nanostructures. However, STM and AFM can only be used to study the QDs on the top surface [21-23] or cross-section specimens of buried QDs where the dots are exposed on the surface of the specimen [24]. In addition, these two techniques can not be performed at the growth temperature either, but at cooled temperature after the fabrication of the nanostructures. In other words, STM and AFM are unable to monitor the physical characterization of the nanostructures during real time in the growth, which is sometimes critical to investigate the nanostructures formation. To overcome the first shortcoming of STM and AFM, the TEM, in particular, high-resolution transition electron microscopy (HRTEM), can be used, which can provide information of the quantum dots embedded in a matrix. As for the second shortcoming of STM and AFM, RHEED is the most convenient way of real-time monitoring of QDs formation. The transformation of the two-dimensional surface into a corrugated 3D islands structure is evidenced by a change in the RHEED pattern from streaky to spotty [25-27]. RHEED is thus a very valuable tool for *in situ* monitoring of the 3D quantum dots formation.

The *optical* methods focus on studying the optical properties of QDs, and also provide an indirect investigation of the physical and electronic properties of QDs. Taking the PL measurement as an example, the position of the PL line contains information about the size of the QDs and about the depth of the confinement potentials. The increase in the QD size and in

the depth of the confinement potential results in a redshift of the PL line. The broadening of the PL spectrum is related to the width of the QD size distribution. More details of the PL measurement will be discussed in Sec. 1.5.

1.2 Strain effect on semiconductor band structure

1.2.1 Strain in lattice-mismatched epitaxy

According to the FvdM/SK growth mode, as described in Sec. 1.1.2, strain is built into the deposited layer by growing a lattice mismatched semiconductor on the top surface of the substrate, while the growth of the layer still maintains crystallinity and long-range order. Therefore, strain is ineluctable and plays a key role in the lattice-mismatched epitaxial growth, thus in the organization of self-assembled quantum dots. If the deposited layer is coherent with the substrate perfectly, the lattice constant of the deposited layer in the direction parallel to the interface is forced to equal to the lattice constant of the substrate. Consequently, the lattice constant of the layer perpendicular to the substrate will be changed by the Poisson effect. If the parallel lattice constant is forced to shrink, compressive strain is produced, and the perpendicular lattice constant will expand. Conversely, if the parallel lattice constant of the deposited layer is force to expand under tensile strain, the perpendicular lattice constant will shrink. Figure 1.4 illustrates these two cases of deposition.

Considering the growth of the epitaxial layer on a [001] oriented substrate, the six strain components can be expressed as [1]:

$$\begin{aligned} &\varepsilon_{xx} = \varepsilon_{yy} \neq \varepsilon_{zz}, \\ &\varepsilon_{xy} = \varepsilon_{yz} = \varepsilon_{zx} = 0. \end{aligned} \tag{1.8}$$

In Eq. (1.8), the parallel strain components, ε_{xx} and ε_{yy}, can be evaluated from:

$$\varepsilon_{xx} = \varepsilon_{yy} = \varepsilon = \frac{a_s - a_l}{a_l}, \tag{1.9}$$

where a_s and a_l are the lattice constants of the substrate and the deposited layer, respectively. Noting that there is no stress in the direction of growth, the perpendicular strain, ε_{zz}, is simply proportional to the parallel strain, ε_{xx}, through the Poisson ratio:

$$\varepsilon_{zz} = -\upsilon\varepsilon_{xx}, \tag{1.10}$$

where the constant υ is the Poisson's ratio of the deposited material. In the case of $a_l > a_s$, e.g. InGaAs layer grown on GaAs substrate, compressive biaxial strain ($\varepsilon_{xx} = \varepsilon_{yy} < 0,\ \varepsilon_{zz} > 0,\ \varepsilon_{xy} = \varepsilon_{yz} = \varepsilon_{zx} = 0$) is generated, as illustrated in Fig. 1.4 (a).

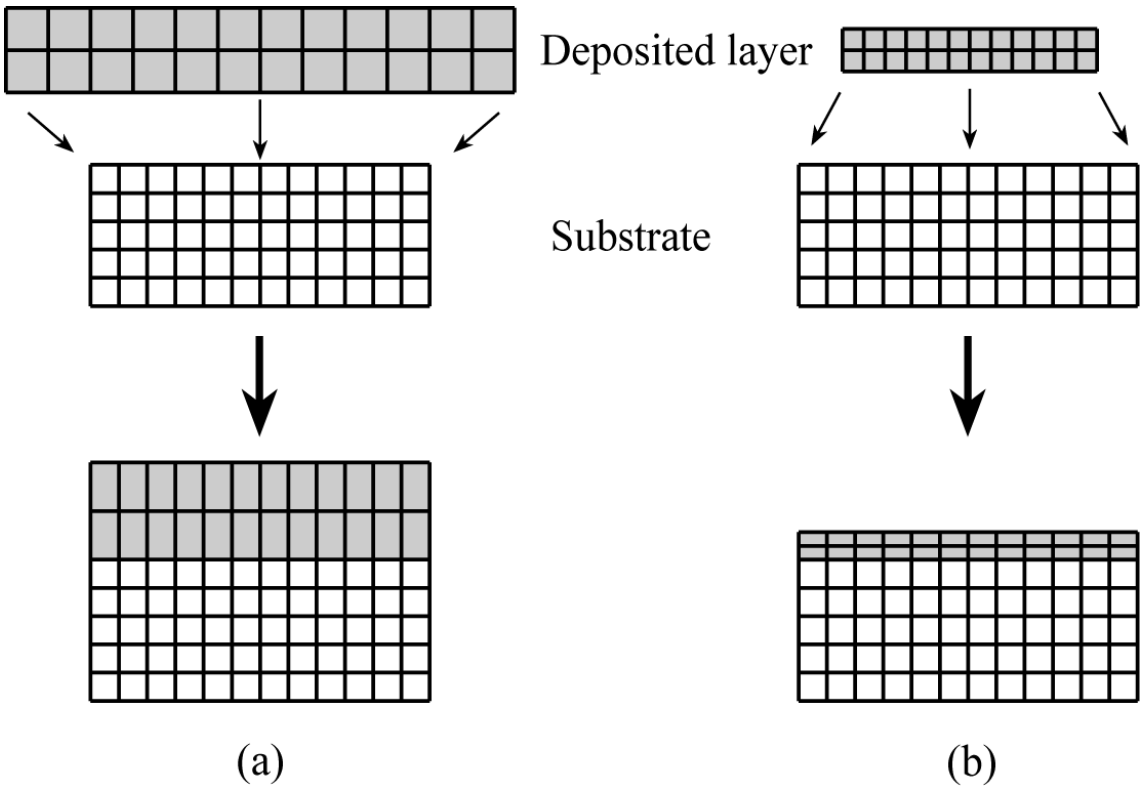

FIG. 1.4 (a) Biaxial compressive and (b) biaxial tensile strain caused by the epitaxial growth of a layer with a lattice constant larger and smaller than that of the substrate, respectively.

Of course, the strain distribution in the 3-dimensional quantum dots is much more complicated than that in the epitaxial growth layer, because of the rearrangement of the strain/stress distribution in the formation of 3D islands. The details about the lattice-mismatched strains in the self-assembled InGaAs/GaAs QDs will be explained in Sec. 4.1.

1.2.2 Band structure of unstrained semiconductor

The built-in strains in the self-assembled quantum dots significantly modify the band structures, and consequently influence the electronic and optical properties of the QDs. In order to understand the effect of strain on the semiconductor band structure, it is important to

examine the band structure in the absence of strain. For the Ⅲ - Ⅴ direct bandgap semiconductors, e.g., InAs, GaAs, etc., the electronic and optical properties of the material are primarily governed by the electron states at the minimum of the conduction band and by the hole states at the maximum of the valence band, where the $\mathbf{k}\cdot\mathbf{p}$ method is extremely useful. The $\mathbf{k}\cdot\mathbf{p}$ method, coupled with the use of symmetry, shows that the band structure in the vicinity of a point in $\mathbf{k}$ space depends on a few parameters, such as band gaps and carrier masses, which may be accurately determined by experiment.

In the $\mathbf{k}\cdot\mathbf{p}$ model, the one-particle Schrodinger equation is written as

$$H\psi = E\psi\,, \tag{1.11}$$

where H is the Hamiltonian, that can be expressed as a sum of the kinetic and potential energy:

$$H = \frac{p^2}{2m} + V(\mathbf{r})\,. \tag{1.12}$$

ψ is the electronic wave function, E is the total energy, $\mathbf{r}$ is the position vector, m is the particle mass, and $V(\mathbf{r})$ is the potential of the atoms in the semiconductor. Since the potential $V(\mathbf{r})$ is periodic in a crystal, we can express this periodicity in the form of $V(\mathbf{r}+\mathbf{R}) = V(\mathbf{r})$, where $\mathbf{R}$ is a lattice vector. The wave function can be written as $\psi(\mathbf{r}) = e^{i\mathbf{k}\cdot\mathbf{r}}u_{n\mathbf{k}}(\mathbf{r})$, where $u_{n\mathbf{k}}(\mathbf{r})$ is a Bloch function, $\mathbf{k}$ lies in the first Brillouin zone, and n is the band index running over a complete set of bands. The Bloch function has the same periodicity as the potential, so that $u_{n\mathbf{k}}(\mathbf{r}+\mathbf{R}) = u_{n\mathbf{k}}(\mathbf{r})$.

The momentum components can be written as:

$$p_x = -i\hbar\frac{\partial}{\partial x},\ p_y = -i\hbar\frac{\partial}{\partial y},\ p_z = -i\hbar\frac{\partial}{\partial z}\,. \tag{1.13}$$

Substituting Eq. (1.13) into Eq. (1.12), the Hamiltonian can be obtained as:

$$H = -\frac{\hbar^2}{2m}\left(\frac{\partial^2}{\partial x^2} + \frac{\partial^2}{\partial y^2} + \frac{\partial^2}{\partial z^2}\right) + V(\mathbf{r})\,. \tag{1.14}$$

With the wave function written in the Bloch form, $\psi(\mathbf{r}) = e^{i\mathbf{k}\cdot\mathbf{r}}u_{n\mathbf{k}}(\mathbf{r})$, we obtain:

$$\left(\frac{p^2}{2m}+\frac{\hbar}{m}\mathbf{k}\cdot\mathbf{p}+\frac{\hbar^2k^2}{2m}+V(\mathbf{r})\right)u_{n\mathbf{k}}(\mathbf{r})=E_n(\mathbf{k})u_{n\mathbf{k}}(\mathbf{r}). \tag{1.15}$$

For any given $\mathbf{k}$, the set of all $u_{n\mathbf{k}}(\mathbf{r})$ is having the same periodicity as $V(\mathbf{r})$. Hence, if we choose $\mathbf{k}=\mathbf{k}_0$, the wave function for any $\mathbf{k}$ may be expressed in terms of the wave function for $\mathbf{k}_0$,

$$u_{n\mathbf{k}}(\mathbf{r})=\sum_m c_{mn}\left(\mathbf{k}-\mathbf{k}_0\right)u_{m\mathbf{k}_0}(\mathbf{r}). \tag{1.16}$$

We call this the $\mathbf{k}_0$ representation. H_{k_0} can be defined as:

$$H_{k_0}=\frac{p^2}{2m}+\frac{\hbar}{m}\mathbf{k}_0\cdot\mathbf{p}+\frac{\hbar^2k_0^2}{2m}+V(\mathbf{r}). \tag{1.17}$$

Then,

$$H_{k_0}u_{n\mathbf{k}_0}=E_n(\mathbf{k}_0)u_{n\mathbf{k}_0}, \tag{1.18}$$

and

$$\left(H_{k_0}+\frac{\hbar}{m}\left(\mathbf{k}-\mathbf{k}_0\right)\cdot\mathbf{p}+\frac{\hbar^2}{2m}\left(k^2-k_0^2\right)\right)u_{n\mathbf{k}}(\mathbf{r})=E_n(\mathbf{k})u_{n\mathbf{k}}(\mathbf{r}), \tag{1.19}$$

At the Γ point ($\mathbf{k}_0=0$), the Schrodinger equation becomes:

$$\sum_m c_{mn}\left(\mathbf{k}\right)H\left(\mathbf{k}\right)\left|u_{m0}(\mathbf{r})\right\rangle=E_n(\mathbf{k})\sum_m c_{mn}\left(\mathbf{k}\right)\left|u_{m0}(\mathbf{r})\right\rangle, \tag{1.20}$$

where $H\left(\mathbf{k}\right)$ is :

$$H\left(\mathbf{k}\right)=\frac{p^2}{2m}+\frac{\hbar}{m}\mathbf{k}\cdot\mathbf{p}+\frac{\hbar^2k^2}{2m}+V(\mathbf{r}). \tag{1.21}$$

We can convert Eq. (1.20) to a matrix eigenvalue equation by substituting Eq. (1.16) in Eq. (1.20), and multiplying from the left by $\left\langle u_{n0}(\mathbf{r})\right|$. We obtain:

$$\sum_m\left\langle u_{n0}(\mathbf{r})\right|H\left(\mathbf{k}\right)\left|u_{m0}(\mathbf{r})\right\rangle c_{mn}\left(\mathbf{k}\right)=E_n(\mathbf{k})c_{mn}\left(\mathbf{k}\right), \tag{1.22}$$

and

$$\langle u_{n0}(\mathbf{r})|H(\mathbf{k})|u_{m0}(\mathbf{r})\rangle = \langle u_{n0}(\mathbf{r})|\frac{p^2}{2m}+V(\mathbf{r})|u_{m0}(\mathbf{r})\rangle + \langle u_{n0}(\mathbf{r})|\frac{\hbar^2k^2}{2m}|u_{m0}(\mathbf{r})\rangle + \langle u_{n0}(\mathbf{r})|\frac{\hbar}{m}\mathbf{k}\cdot\mathbf{p}|u_{m0}(\mathbf{r})\rangle$$
$$= E_n(0)\delta_{nm} + \frac{\hbar^2k^2}{2m}\delta_{nm} + \frac{\hbar}{m}\mathbf{k}\cdot\langle u_{n0}(\mathbf{r})|\mathbf{p}|u_{m0}(\mathbf{r})\rangle \tag{1.23}$$

The matrix element $\frac{\hbar}{m}\mathbf{k}\cdot\langle u_{n0}(\mathbf{r})|\mathbf{p}|u_{m0}(\mathbf{r})\rangle$ must be determined by experiment for different materials. Although Eq. (1.23) as it stands is correct for any $\mathbf{k}$, it is most useful when $\mathbf{k}$ is near $\mathbf{k}_0 = 0$ (Γ point), so that the nondiagonal part of the Hamiltonian, $\frac{\hbar}{m}\mathbf{k}\cdot\mathbf{p}_{nm}$, can be treated as a perturbation.

In order to solve the Schrodinger equation (Eq. (1.22) and (1.23)), certain perturbation theories, such as that proposed by Lowdin [28], are usually used with an attempt to diagonalize the Hamiltonian completely. Since it is beyond the scope of this thesis to derive the Hamiltonian, we will directly use the detailed Hamiltonian forms in the calculations. Before introducing the Hamiltonian forms, we'd better have a brief overview of the band structures.

In general, the band structures of the semiconductors, which have the diamond/zincblende crystal structure like InAs, GaAs, Si, Ge, etc., are more complicated in the valence band than they are in the conduction band. The states at the Γ conduction band minimum have a central cell periodic part which is spherically symmetric. It is described as being made up of s-type states at the band edges, i.e. the 'Bloch' wave function has the symmetry of an atomic s orbital. For the states near the X and near the L conduction band minima, the anisotropy of the wave function is strong. This anisotropy is described by appropriate combination of the s-, p_x-, p_y-, p_z-type functions. For the valence band edge states, the central cell part of the wave function is primarily p-type. Detailed microscopic calculations[1] show that there are two valence bands degenerate at the Γ point, and close by (a few tens to a few hundreds of meV below) there is a third band. The first two are called heavy-hole (HH) and light-hole (LH) bands, and they become degenerate for finite values of the wave vector $\mathbf{k} = k_x, k_y, k_z$: the energy of the former descends at a slower rate as the wave vector moves away from the Γ point, which corresponds to a larger effective mass, hence the name. The third band is called the spin-orbit split-off (SO) band.

The 4×4 and 6×6 Hamiltonians were derived by Luttinger and Kohn [29] using $\mathbf{k}\cdot\mathbf{p}$

perturbation theory. The former takes into account the mixing of the HH and LH bands, while the latter also includes the mixing with the SO bands. Both forms have been applied to QDs [30-32]. Considering the interaction between conduction and valence bands, the 8×8 Hamiltonian was developed by Pidgeon and Brown [33]. Other higher band Hamiltonians have also been developed depending on the energy range of interest. It has been proven that the $\mathbf{k}\cdot\mathbf{p}$ method is very easy and convenient to improve the calculation precision simply by adding the number of bands in the Hamiltonian. This is one reason why the $\mathbf{k}\cdot\mathbf{p}$ method has been so widely used in the calculation of the band structures of semiconductors.

In many cases, the 6×6 Hamiltonian leads to good accuracy, as be used in our calculation. The states in the valence band (HH, LH, and SO bands) can be described in terms of angular momentum states $|J,m_J\rangle$ (J is the total angular momentum, equal to $3\hbar/2$ or $\hbar/2$, and m_J is the projection of the angular momentum along the *z*-axis, equal to $\pm3/2$ or $\pm1/2$), and spin state ($\uparrow=+1/2$, $\downarrow=-1/2$). The list of the $|J,m_J\rangle$ basis states is given as [1]:

$$
\begin{aligned}
\text{HH states: } |3/2,3/2\rangle &= \frac{1}{\sqrt{2}}\left(|p_x\rangle+i|p_y\rangle\right)\uparrow,\\
|3/2,-3/2\rangle &= \frac{1}{\sqrt{2}}\left(|p_x\rangle-i|p_y\rangle\right)\downarrow;\\
\text{LH states: } |3/2,1/2\rangle &= \frac{1}{\sqrt{6}}\left(|p_x\rangle+i|p_y\rangle\right)\downarrow-\frac{\sqrt{2}}{\sqrt{3}}|p_z\rangle\uparrow,\\
|3/2,-1/2\rangle &= -\frac{1}{\sqrt{6}}\left(|p_x\rangle-i|p_y\rangle\right)\uparrow-\frac{\sqrt{2}}{\sqrt{3}}|p_z\rangle\downarrow;\\
\text{SO states: } |1/2,1/2\rangle &= \frac{1}{\sqrt{3}}\left(|p_x\rangle+i|p_y\rangle\right)\downarrow+\frac{1}{\sqrt{3}}|p_z\rangle\uparrow,\\
|1/2,-1/2\rangle &= -\frac{1}{\sqrt{3}}\left(|p_x\rangle-i|p_y\rangle\right)\uparrow+\frac{1}{\sqrt{3}}|p_z\rangle\downarrow.
\end{aligned}
\tag{1.24}
$$

In this $|J,m_J\rangle$ basis, the 6×6 Hamiltonian that describes the HH, LH and SO bands can be obtained as [1, 34, 35]:

$$H^{\mathrm{v}} = -\begin{bmatrix} P+Q & -S & R & 0 & \frac{\sqrt{2}}{2}S & -\sqrt{2}R \\ -S^{\dagger} & P-Q & 0 & R & \sqrt{2}Q & -\frac{\sqrt{6}}{2}S \\ R^{\dagger} & 0 & P-Q & S & -\frac{\sqrt{6}}{2}S^{\dagger} & -\sqrt{2}Q \\ 0 & R^{\dagger} & S^{\dagger} & P+Q & \sqrt{2}R^{\dagger} & \frac{\sqrt{2}}{2}S^{\dagger} \\ \frac{\sqrt{2}}{2}S^{\dagger} & \sqrt{2}Q & -\frac{\sqrt{6}}{2}S & \sqrt{2}R & P+\Delta_0 & 0 \\ -\sqrt{2}R^{\dagger} & -\frac{\sqrt{6}}{2}S^{\dagger} & -\sqrt{2}Q & \frac{\sqrt{2}}{2}S & 0 & P+\Delta_0 \end{bmatrix} \begin{matrix} \left|\frac{3}{2}, \frac{3}{2}\right\rangle \\ \left|\frac{3}{2}, \frac{1}{2}\right\rangle \\ \left|\frac{3}{2}, -\frac{1}{2}\right\rangle \\ \left|\frac{3}{2}, -\frac{3}{2}\right\rangle \\ \left|\frac{1}{2}, \frac{1}{2}\right\rangle \\ \left|\frac{1}{2}, -\frac{1}{2}\right\rangle \end{matrix}, \tag{1.25}$$

where

$$\begin{aligned} P &= \left(\frac{\hbar^2}{2m}\right)\gamma_1\left(k_x^2+k_y^2+k_z^2\right), \\ Q &= \left(\frac{\hbar^2}{2m}\right)\gamma_2\left(k_x^2+k_y^2-2k_z^2\right), \\ R &= \left(\frac{\hbar^2}{2m}\right)\sqrt{3}\left[-\gamma_2\left(k_x^2-k_y^2\right)+2i\gamma_3 k_x k_y\right], \\ S &= \left(\frac{\hbar^2}{2m}\right)2\sqrt{3}\gamma_3\left(k_x-ik_y\right)k_z, \end{aligned} \tag{1.26}$$

$\gamma_{1,2,3}$ are the Luttinger parameters, and Δ_0 is the spin-orbit splitting energy (the spacing between the HH/LH band and the SO band at the Γ point). The elements indicated with a superscript of $\dagger$ are the corresponding conjugate complexes.

In order to find eigenenergies for a specified $\mathbf{k}$, solutions can be sought to $\det\left|H-EI\right|=0$, which gives a sixth-order polynomial of the energy E. Only numerical solutions can be searched, unless two identical third-order polynomials are available, allowing analytic solution. Considering the Γ point, where the $\mathbf{k}$ is $k_x=k_y=k_z=0$, the Hamiltonian in Eq. (1.25) becomes:

$$H^{\mathrm{v}}\left(\mathbf{k}=0\right)=-\begin{bmatrix} 0 & 0 & 0 & 0 & 0 & 0 \\ 0 & 0 & 0 & 0 & 0 & 0 \\ 0 & 0 & 0 & 0 & 0 & 0 \\ 0 & 0 & 0 & 0 & 0 & 0 \\ 0 & 0 & 0 & 0 & \Delta_0 & 0 \\ 0 & 0 & 0 & 0 & 0 & \Delta_0 \end{bmatrix}. \tag{1.27}$$

This Hamiltonian has a fourfold degenerate eigenvalue $E=0$, and a twofold degenerate eigenvalue $E=-\Delta_0$. This result is consistent with the concept that there are HH and LH bands degenerate at $\mathbf{k}=0$, and an SO band displaces by Δ_0 from them.

1.2.3 Effect of strain on the band structure

The existence of strains in the nanostructures, such as those generated in the epitaxial growth as addressed in Sec. 1.2.1, modifies the energies at the band edges of the material. To calculate the strain-induced modification in the band edge energies, the deformation potential theory [36] is a powerful method, in which the hydrostatic strain (ε_{h}), biaxial strain (ε_{s}), and shear strain components (ε_{xy}, ε_{yz}, and ε_{zx}) are of great importance. The hydrostatic strain is defined as $\varepsilon_{\mathrm{h}}=\varepsilon_{xx}+\varepsilon_{yy}+\varepsilon_{zz}$ representing the relative volume change of the unit cell, and the biaxial strain is $\varepsilon_{\mathrm{s}}=\varepsilon_{zz}-\left(\varepsilon_{xx}+\varepsilon_{yy}\right)/2$ when the *x*, *y* axes are taken as the biaxial strain axes. Since the hydrostatic strain only gives a volume change without affecting the crystal symmetry, all the band edges will be shifted due to ε_{h}. However, the biaxial stain, as well as the shear strain component, usually decreases the symmetry of a strain-free crystal, resulting in a splitting in the degenerate band edges, such as the *X*-/*L*-conduction band and the valence band.

The strain-induced modifications of the valence band, for example, can be analyzed based on the strain-dependent Hamiltonian. Each element in the Hamiltonian is modified by the strains as follows [34, 35]:

$$
\begin{aligned}
&P \to P + P_\varepsilon, \quad P_\varepsilon = a_\mathrm{v}\left(\varepsilon_{xx} + \varepsilon_{yy} + \varepsilon_{zz}\right) \\
&Q \to Q + Q_\varepsilon, \quad Q_\varepsilon = b\left[\varepsilon_{zz} - \frac{1}{2}\left(\varepsilon_{xx} + \varepsilon_{yy}\right)\right] \\
&R \to R + R_\varepsilon, \quad R_\varepsilon = \frac{\sqrt{3}}{2} b\left(\varepsilon_{xx} - \varepsilon_{yy}\right) - id\varepsilon_{xy} \\
&S \to S + S_\varepsilon, \quad S_\varepsilon = -d\left(\varepsilon_{zx} - i\varepsilon_{yz}\right)
\end{aligned}
\tag{1.28}
$$

where a_v and b, and d are the Pikus-Bir deformation potentials, describing the influence of hydrostatic, biaxial, and shear strain, respectively. Still considering the Γ point (i.e. the maximum of the valence band), which is of most interest, the strained Hamiltonian becomes [34, 35].

$$
H_\varepsilon^\mathrm{v} = -\begin{bmatrix}
P_\varepsilon + Q_\varepsilon & -S_\varepsilon & R_\varepsilon & 0 & \frac{\sqrt{2}}{2}S_\varepsilon & -\sqrt{2}R_\varepsilon \\
-S_\varepsilon^\dagger & P_\varepsilon - Q_\varepsilon & 0 & R_\varepsilon & \sqrt{2}Q_\varepsilon & -\frac{\sqrt{6}}{2}S_\varepsilon \\
R_\varepsilon^\dagger & 0 & P_\varepsilon - Q_\varepsilon & S_\varepsilon & -\frac{\sqrt{6}}{2}S_\varepsilon^\dagger & -\sqrt{2}Q_\varepsilon \\
0 & R_\varepsilon^\dagger & S_\varepsilon^\dagger & P_\varepsilon + Q_\varepsilon & \sqrt{2}R_\varepsilon^\dagger & \frac{\sqrt{2}}{2}S_\varepsilon^\dagger \\
\frac{\sqrt{2}}{2}S_\varepsilon^\dagger & \sqrt{2}Q_\varepsilon & -\frac{\sqrt{6}}{2}S_\varepsilon & \sqrt{2}R_\varepsilon & P_\varepsilon + \Delta_0 & 0 \\
-\sqrt{2}R_\varepsilon^\dagger & -\frac{\sqrt{6}}{2}S_\varepsilon^\dagger & -\sqrt{2}Q_\varepsilon & \frac{\sqrt{2}}{2}S_\varepsilon & 0 & P_\varepsilon + \Delta_0
\end{bmatrix}. \tag{1.29}
$$

Obviously, the strained Hamiltonian is much more complicated than the unstrained case (Eq. 1.27).

In the case of biaxial strain, like that generated in the growth of lattice-mismatched epitaxy (Sec. 1.2.1), all shear strain components are zero, while the non-zero strains are $\varepsilon_{xx} = \varepsilon_{yy}$, $\varepsilon_{zz} = -\upsilon\varepsilon_{xx}$. Substituting Eq. (1.8) into Eqs. (1.28) and (1.29), the shifts of the valence band are obtained as

$$
\begin{aligned}
&\Delta E_\mathrm{HH} = -P_\varepsilon - Q_\varepsilon \\
&\Delta E_\mathrm{LH} = -P_\varepsilon + \frac{1}{2}\left(Q_\varepsilon - \Delta_0 + \sqrt{\Delta_0^2 + 2\Delta_0 Q_\varepsilon + 9Q_\varepsilon^2}\right), \\
&\Delta E_\mathrm{SO} = -P_\varepsilon + \frac{1}{2}\left(Q_\varepsilon - \Delta_0 - \sqrt{\Delta_0^2 + 2\Delta_0 Q_\varepsilon + 9Q_\varepsilon^2}\right)
\end{aligned}
\tag{1.30}
$$

where ΔE_{HH}, ΔE_{LH}, and ΔE_{SO} are the strain-induced shifts of the heavy hole (HH), light hole (LH), and spin-orbit (SO) band, respectively.

Detailed calculations of the strain-induced shifts in the conduction and valence bands and the energy shift in the InGaAs/GaAs QDs will be discussed in Chapter 4.

1.3 Nanoprobe indentation

In order to calculate the strain-induced modifications in the band structure using the deformation potential theory, one should firstly get clear the strain fields existing in the semiconductor structures. There are several different ways to introduce strains into the semiconductor structure. One way is to grow an epitaxial lattice-mismatched layer of a semiconductor material on top of a substrate. As described in Sec. 1.2.1, the epitaxial layer is forced to acquire the in-plane lattice constant of the substrate, and the perpendicular lattice constant will then also change. Compressive or tensile biaxial strain field will be created ($\varepsilon_{xx} = \varepsilon_{yy} \neq \varepsilon_{zz}$, $\varepsilon_{xy} = \varepsilon_{yz} = \varepsilon_{zx} = 0$), depending on whether the lattice constant of the deposited layer is larger or smaller than that of the substrate. Another way is to subject a semiconductor to hydrostatic pressure in a diamond anvil cell. In this case, hydrostatic strain field is introduced ($\varepsilon_{xx} = \varepsilon_{yy} = \varepsilon_{zz}$, $\varepsilon_{xy} = \varepsilon_{yz} = \varepsilon_{zx} = 0$), and the cubic unit cell becomes compressed equally in all three directions. The third way is to press a nanoprobe on the top surface of a semiconductor, introducing localized strain fields with all strain components being non-zero. The fourth way is to apply a uniaxial stress along some direction, e.g. *z*, while leaving the surfaces perpendicular to the other two axes free. As a result, biaxial strain field with compressive strain along *z* and tensile strain along *x* and *y* ($\varepsilon_{xx} = \varepsilon_{yy} \neq \varepsilon_{zz}$, $\varepsilon_{xy} = \varepsilon_{yz} = \varepsilon_{zx} = 0$) is generated if uniaxial pressure is applied. For the self-assembled quantum dots, the first way usually takes place during the organization of dots, inducing the lattice-mismatched strains. The other three ways, however, are used as external means to produce the strain fields, which have been extremely important in understanding the band structures of semiconductors and in measuring the deformation potentials of semiconductor materials.

Comparing all the strain-introduction methods mentioned above, we can see that the nanoprobe indentation is the unique method in generating a localized strain field as well as in introducing shear strain components. The generated inhomogeneous strain field results in the optical response of QDs under the strain effect behaving differently from QD to QD.

Consequently, through the optical response from each QD, the discrete energy levels in each dot, which is one of the most important features of the QDs, can be successfully investigated. The traditional hydrostatic pressure experiment, for example, only allows the measurement of the optical response of the whole QD sample, which actually reflects the overlap of the discrete energy levels from all QDs. On the other hand, the introduced shear strain components by the indentation make it possible to evaluate the influence of shear strains on the band structures of semiconductors, which can not be realized by the other strain-introduction methods.

In the past decade, the method of nanoprobe indentation has been well developing, and a series of researches have been reported [37-47]. The method was proposed by Robinson *et al* [37] for the first time studying a sample consisting of the self-assembled InAlAs QDs. PL emission lines from single QDs with large linear blueshift under the indented pressure were successfully collected by using the near-field scanning optical microscope (NSOM). Furthermore, the PL from all QDs were observed to be quenched at relative high pressures, probably caused by the inhomogeneous strain-induced potential gradient, direct-to-indirect transition or valence band mixing. Unfortunately, the simple estimates of the indentation force, the indentation-induced strain/stress fields, and the strain effect on the optical properties of the QDs were insufficient in this report, so that the experimentally measured blueshift of the single QD PL did not agree well with the theoretical estimates and the mechanism of the observed PL quenching has not been determined exactly either. Later, the methods to estimate the indentation depth (indented force), the strain field and the strain-induced modifications of the optical properties of QDs were improved by Johnson *et al* [41], which gave a more reasonable estimate of the strain-induced optical shift observed by Robinson. Dislocation activity was proposed to be responsible for the observed emission quenching, but without any experimental evidence. Similar nanoindentation experiments were also performed for different quantum dots systems [38-40, 42-44]. Both the blueshift of the luminescence/photoluminescence from single QD and change of the (integrated) intensity with the increase of applied pressure, behaving as first increasing, then decreasing and finally disappearing, were reported. The blueshift of luminescence/PL with the pressure was believed to be primarily caused by the upward shift of the Γ conduction band induced by the generated strain fields. The disappearances of the luminescence/PL at relative high pressures, however, were ascribed to different mechanisms in different reports, such as $\Gamma - X$

crossover in Ref. 38, carrier diffusion out of dot due to strain-induced potential gradient in Ref. 39 and 40, or tunneling of hole-accumulation away from the QD layer in Ref. 42. In order to quantitatively understand the PL behaviors of QDs under the indentation, as one knows, the key issues of great importance will be the precise measurement of the indented force, the complete understanding of the indented strain fields, and the evaluation of the strain-induced modifications of the optical properties of QDs. In all the above-mentioned reports relating to the nanoindentation work [37-44], however, one or more of these key information is lack. This is mainly because that the tip of the probe was not fabricated precisely [37, 39-42, 44] or the three-dimensional indentation-induced strain fields in QDs were not correctly reflected in the two-dimensional analysis [37-40, 42-44].

Recently, Liang *et al* [45] improved the system of nanoprobe indentation, in which the applied indentation force was precisely measured by a high-sensitivity loadcell placed under the QD sample. Furthermore, a three-dimensional finite element method (FEM) has also been developed to calculate the strain fields in the QDs, including the lattice-mismatched strains and the indentation-induced strains. The calculated strain-induced energy shift in the QDs agreed quantitatively with the experimentally obtained PL blueshift. Later, based on this developed nanoindentation system and strain calculation method, they succeeded in identifying the location of individual QD, as reported in Ref. 46 and 47. The identification of single QD location may probably make great contribution to the development of single-QD devices. The mechanism for the PL quenching observed in their work was excluded to be the generation of dislocation as reported in Ref. 41, because the quenched PL peaks appeared again when the indentation force was unloaded [47]. The work in this thesis will be based on the work of Liang *et al*, aiming for further investigation of the exact mechanism for the observed PL quenching.

1.4 PL measurement of quantum dots

In Sec. 1.2.3, the theoretical evaluation of the strain effects on the semiconductor (QDs) band structures was addressed. To evaluate these influences experimentally, like under the nanoprobe indentation, one of the most efficient means is to study the optical properties of strained quantum dots, such as measuring the photoluminescence (PL) spectrum emitted from the QDs under the strain states. As mentioned in Sec. 1.1.3, the PL spectrum provides indirect information about the electronic properties of QDs (energy levels of confined electrons/holes),

while the electronic properties of QDs are strongly dependent on the band structure. Therefore, by analyzing the PL spectra emitted from the QDs before and after the strain effects, one can easily investigate the consequence of strains on the optical properties of QDs, and can thus evaluate the effect of strains on the invisible electronic band structures experimentally.

The principle of PL measurement is to create energetic electrons and holes by optical excitation with photon energy, $h\upsilon_1$, above the bandgap of the quantum structure. In general, a light source, usually a laser, is used for excitation. Absorbing the excitation photon, an electron-hole pair generates in the barrier semiconductor material. If the temperature is sufficiently low (e.g. less than 25 K for GaAs), the energetic charge carriers will relax to the band edges (conduction band edge for electrons and valence band edge for holes) in the barrier material in a very short time. Then the carriers move by diffusion and are finally captured in the potential well created by a quantum dot, where they relax to their respective lowest energy states. The electron-hole pair (e-h pair) in the dot forms a bound state, creating a particle called exciton. The recombination of an exciton will give rise to a sharp-line luminescence, with an energy, $h\upsilon_2$, equal to the difference between the ground states of electrons and holes minus the binding energy of the exciton. Figure 1.5 illustrates the process of luminescence formation in a quantum dot structure. In a direct band gap QD, a photon will be emitted if the exciton recombination occurs. The emitted light (photons) can be collected and analyzed by a spectrometer.

If the carrier relaxation in the dot is fast compared with the exciton recombination, PL only from the lowest energy state will be obtained, as shown in Fig. 1.5, provided that the excitation power density is not too high. With increasing the density of the excitation power, PL from excited states appears. If carrier relaxation is not too fast, there is a probability that one will observe PL emission from excited states, even at a relatively lower excitation power density. The strength of these lines depends on the ratio between the relaxation time and the recombination time. Furthermore, the region of the self-assembled QD sample illuminated by the laser usually contains several tens of QDs. Due to the naturally occurring dot-dot size, shape, and morphology fluctuations in the self-assembled QDs, complicated overlap of the inter-band optical response from ensembles of QDs arises, resulting in a large inhomogeneous broadening of the PL linewidth. In contrast, individual self-assembled QDs possess a discrete, homogeneously broadened optical spectrum reflecting their fully quantized electronic

structure. Therefore, the PL measurement is widely used to research the band structures of unstrained/strained semiconductor structures.

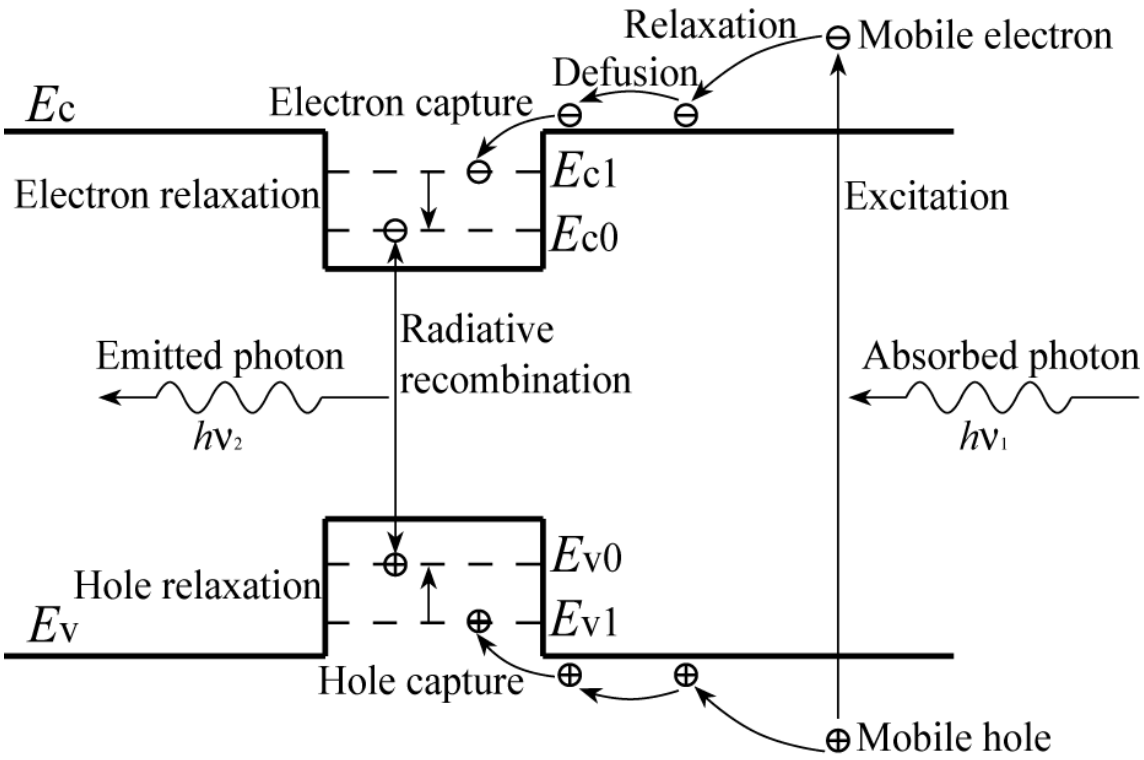

FIG. 1.5 The process of luminescence formation in a QD structure.

1.5 Scope and objectives

The objectives of this thesis are three. The first objective is to make clear the effect of strains on the optical properties of self-assembled InGaAs/GaAs QDs, especially on the indirect band edges, based on the previous researches on the nanoindentation and strain calculations. In the previous works, the simultaneous measurement of the indentation force and the PL emission from QDs under the indentation has already been successfully realized, as well as the three-dimensional simulation of the strain fields in the QDs. However, the consequence of strains on the indirect band edges has not yet been examined in their works. Therefore, the present work will focus on the strain-induced modifications in the indirect band edges in addition to the direct band edges. The second objective is to determine the location of single QD through the measurement of PL emission under the indentation of flat cylindrical or

dome-shaped probe. The third objective is to figure out the possible mechanism for the PL quenching observed with the indentation of the flat cylindrical nanoprobe. The quenching force, measured as the indentation force at which the PL from QDs disappears, varies from QD to QD. This variation is related to the location of individual QD. By analyzing the relationship between the strain fields/strain-induced energy shifts in the band edges and the location of individual QDs using the flat cylindrical nanoprobe, the possible mechanisms for the observed PL quenching are examined. Therefore, the achievement of the first two objectives is the prerequisite for realizing the third objective.

In order to achieve the above three objectives, the experiments of nanoprobe indentation and the calculations of the strain fields in the QDs as well as the strain consequence on the band edges energies are inevitable. Followings are the experimental method and simulation details we have preformed in this study.

Experimental part:

(1) To fabricate the tip of nanoprobe precisely with different shapes, flat cylindrical probe or dome-shaped probe;

(2) To indent the nanoprobe onto the QD sample, changing the probe either in the vertical position (indentation force) or in the horizontal position (relative position of probe to the sample) during the indentation, and collect the PL emissions from the QDs sample;

(3) To analyze the collected PL spectra, obtaining the dependence of the PL energy/intensity on the indentation force or on the indentation position of the probe;

(4) To trace the PL peaks from single QDs with the change of the indentation force or the indentation position of the probe;

(5) To integrate the PL peak intensity emitted from individual QD at each indentation force step, and measure the quenching force at which the integrated PL intensity becomes zero.

Simulation part:

(1) To simulate the three-dimensional strain fields in and around the QDs, depending on the shape, size of the nanoprobe used in the experiments;

(2) To calculate the energy shifts of the direct and indirect band edges induced by the

strains using the deformation potential theory;

(3) To compare the blueshift of the PL peak energy with the indentation-force/indentation-position measured in the experiments to the simulated values, and estimate the location of individual QDs through the comparisons;

(4) To examine the possible mechanisms for the observed PL quenching by comparing the experiment/simulation results in the flat cylindrical probe case.

1.6 Overview of the thesis

In this thesis, we proposed methods to estimate the location of embedded InGaAs/GaAs QDs, and examined the possible mechanisms for the PL quenching observed in the nanoindentation. A series of indentation experiments using probes with different tip shapes and numerical calculations of the strains/strain-induced energy shifts were carried out.

In Chapter 2, the experimental setup and methodologies were introduced, including the preparation of the QD samples, the fabrication of the probes with different tip shapes, the experiment setups and the different types of indentation experiments depending on different experimental purposes.

In Chapter 3, the PL spectra emitted from the QDs sample, collected in different types of indentation experiments, were analyzed. The PL peak energy from single QD acted as a function of the applied indentation force or the indentation position of the probe. The dependence of the PL energy on the indentation force was used to measure the quenching force experimentally, as well as the blueshift rate for each QD. The measured blueshift rate will be used to estimate the location of each QD in Chapter 5 in the case of flat cylindrical probe. The dependence of the PL energy on the probe's indentation position was used to identify the QDs location using our previous method, the flat cylindrical probe case of which was performed in order to examine the precision of the estimation method proposed in this study. We also achieved a great improvement in estimating the QD location by using the dome-shaped probe.

In Chapter 4, strain fields in and around the QDs, including both the lattice mismatched and indented strains, were simulated based on the three-dimensional finite element models. The obtained strain fields were then used to calculate the energy shifts in the band structures by the deformation potential theory. The strains/energy shifts results showed strong

dependences on the QDs location.

In Chapter 5, methods were proposed to estimate the location of the embedded QDs by using the nanoprobes with different tip shapes. The effect of the tip shapes on the PL emissions from QDs was also discussed.

In Chapter 6, the possible mechanisms for the PL quenching observed under the indentation of the flat cylindrical nanoprobe were examined based on the quantitative calculations of the band-edge energy shifts. The observed PL quenching was ascribed to one of two possible mechanisms, the crossover between the Γ and X or L band of InGaAs or the electron-repulsion resulting from the strain-induced potential gradient.

In Chapter 7, the general conclusions and recommendation for the future work were given.

References

[1] P. Harrison, "*Quantum wells, wires, and dots*", John Wiley & Sons LTD, 2nd Edition, 259 (2005)

[2] V. G. Stoleru, "*(In,Ga)As/GaAs Quantum-Dot Nanostructures: Strain Distribution and Electronic Structure*", Doctor dissertation of University of Virginia, 3-7 (2002).

[3] N. Kirstaedter, "*Low threshold, large T0 injection laser emission from (InGa)As quantum dots*", Electronic letters 30(17), 1416-1417 (1994).

[4] N. N. Ledentsov, "*Direct formation of vertically coupled quantum dots in Stranski-Krastanow growth*", Physical Review B 54(12), 8743 (1996).

[5] H. Saito, "*Room-temperature lasing operation of a quantum-dot vertical-cavity surface-emitting laser*", Applied Physics Letters 69(21), 3140-3142 (1996).

[6] A. M. Adawi, "*Strong in-plane polarized intraband absorption in vertically aligned InGaAs/GaAs quantum dots*", Applied Physics Letters 82(20), 3415-3417 (2003).

[7] S. Krishna, "*Quantum dots in a well infrared photodetector*", Journal of Physics D: Applied Physics 38(13), 2142-2150 (2005).

[8] M. Razeghi, "*Transport and photodetection in self-assembled semiconductor quantum dots*", Nanotechnology 16(2), 219-229 (2005).

[9] H. Hashiba, V. Antonov, L. Kulik, A. Tzalenchuk, P. Kleinschmid, S. Giblin, and S. Komiyama, "*Isolated quantum dot in application to terahertz photon counting*", Physical Review B 73, 081310(R) (2006).

[10] M. Ozkan, "*Quantum dots and other nanoparticles: what can they offer to drug discovery?*", Drug Discovery Today 9(24), 1065 (2004).

[11] P. X. Guo, and C. M. Wei, "*Quantum dots for robust and simple assays using single particles in nanodevices*", Nanomedicine: Nanotechnology, Biology, and Medicine 1, 122-124 (2005).

[12] S. D. Bartlett, T. Rudolph, and R. W. Spekkens, "*Reference frames, superselection rules, and quantum information*", Reviews of Modern Physics 79 (2), 555-55 (2007).

[13] D. Bimberg, M. Grundmann, and N. N. Ledentsov, "*Quantum Dot Heterostructures*", John Wiley & Sons, New York, 6 (1999).

[14] M. Jaros, "*Physics and Applications of Semiconductor Heterostructures*", Clarendon Press, Oxford, 1999.

[15] J. H. Van der Merwe, "*Crystal Interfaces. Part 1. Semi-Infinite Crystals*", Journal of

Applied Physics 34(1), 117 (1963).

[16] B. J. Spencer, P. W. Voorhees, and S. H. Davis, "*Morphological instability in epitaxially strained dislocation-free solid films*", Physical Review Letters 67(26), 3696 (1991).

[17] J. Tersoff, and R. M. Tromp, "*Shape transition in growth of strained islands: Spontaneous formation of quantum wires*", Physical Review Letters 70(18), 2782 (1993).

[18] E. Palange, G. Capellini, L. Di Gaspare, and F. Evangelisti, "*Atomic force microscopy and photoluminescence study of Ge layers and self-organized Ge quantum dots on Si(100)*", Applied Physics Letters 68, 2982 (1996).

[19] I. Kamiya, I. Tanaka, and H. Sakaki, "*Optical properties of near surface-InAs quantum dots and their formation processes*", Physica E 2, 637 (1998).

[20] P. Chen, Q. Xie, A. Madhukar, L. Chen, and A. Konkar, "*Mechanisms of strained island formation in molecular-beam epitaxy of InAs on GaAs(100)*", Journal of Vacuum Science Technology B124, 2568 (1994).

[21] C. Lobo, and R. Leon, "*InGaAs island shapes and adatom migration behavior on (100), (110), (111), and (311) GaAs surfaces*", Journal of Applied Physics 83(8), 4168 (1998).

[22] J. H. Zhu, K. Brunner, and G. Abstreiter, "*Observation of (105) facetted Ge pyramids inclined towards vicinal Si (001) surfaces*", Applied Physics Letters 72(4), 424 (1998).

[23] H. Saito, K. Nishi, S. Sugou, and Y. Sugimoto, "*Controlling polarization of quantum-dot surface-emitting lasers by using structurally anisotropic self-assembled quantum dots*", Applied Physics Letters 71(4), 590 (1997).

[24] W. Wu, J. R. Tucker, G. S. Solomon, and J. S. Harris Jr., "*Atom-resolved scanning tunneling microscopy of vertically ordered InAs quantum dots*", Applied Physics Letters 71(8), 1083 (1997).

[25] Y. Nabetani, T. Ishikawa, S. Noda, and A. Sakaki, "*Initial growth stage and optical properties of a three-dimensional InAs structure on GaAs*", Journal of Applied Physics 76(1), 347 (1994).

[26] K. Ozasa, Y. Aoyagi, Y. Ju Park, and L. Samuelson, "*Reversible transition between InGaAs dot structure and InGaAsP flat surface*", Applied Physics Letters 71(6), 797-799 (1997).

[27] K. Ozasa, and Y. Aoyagi, "*In situ composition control of self-organized InGaAs dots*", Journal of Crystal Growth 188, 370-376 (1998).

[28] P. Lowdin, "*A note on the quantum-mechanical perturbation theory*", Journal of

Chemistry and Physics 19, 1396 (1951).

[29] J. M. Luttinger, and W. Kohn, "*Motion of electrons and holes in perturbed periodic fields*", Physical Review 97(4), 869 (1955).

[30] D. S. Citrin, and Y. –C. Change, "*Valence-subband structure of GaAs/AlxGa1-xAs quantum wires: The effect of split-off bands*", Physical Review B 40(8), 5507 (1989).

[31] A. I. Ekimov *et al*., "*Absorption and intensity-dependent photoluminescence measurement on CdSe quantum dots: assignment of the first electronic transitions*", Journal of the Optical Society of America B 10(1), 100 (1993).

[32] C. Pryor, "*Eight-band calculations of strained InAs/GaAs quantum dots compared with one-, four-, and six-band approximations*", Physical Review B 57(12), 7190-7195 (1998).

[33] C. R. Pidgeon, and R. N. Brown, "*Interband magneto-absorption and Faraday rotation in InSb*", Physical Review 146, 575 (1966).

[34] C. Y.-P. Chao, and S. L. Chuang, "*Spin-orbit-coupling effects on the valence-band structure of strained semiconductor quantum wells*", Physical Review B 46(7), 4110 (1992).

[35] P. Y. Yu, and M. Cardona, "*Fundamentals of semiconductors*", 3rd corrected printing, Springer Berlin Heidelberg New York, p121 (2005).

[36] G. L Bir, G. E. Pikus, "*Symmetry and Strain-induced Effects in Semiconductors*", Wiley, New York, 1974.

[37] H. D. Robinson, M. G. Muller, B. B. Goldberg, and J. L. Merz, "*Local optical spectroscopy of self-assembled quantum dots using a near-field optical fiber probe to induce a localized strain field*", Applied Physics Letters 72(17), 2081 (1998).

[38] A. Chavez-Pirson, J. Temmyo, and H. Ando, "*Pressure-induced modulation of the confinement in self-organized quantum dots produced and detected by a near-field optical probe*", Physica E 7, 367-372 (2000).

[39] Kazunari Ozasa, Sintaro Nomura, and Yoshinobu Aoyagi, "*Pressure effects on nanoprobe photoluminescence of quasi-zero-dimensional confinement quantum dots*", Superlattices and Microstructures 30(4), 169 (2001).

[40] Kazunari Ozasa, and Yoshinobu Aoyagi, "*Nanoprobe photoluminescence of quasi-zero-dimensional InGaAsP quantum dots*", Physica E 13, 212-215 (2002).

[41] H. T. Johnson, and R. Bose, "*Nanoindentation effect on the optical properties of self-assembled quantum dots*", Journal of the Mechanics and Physics of Solids 51, 2085-2104 (2003).

[42] Kazunari Ozasa, Yoshinobu Aoyagi, Akihiko Yamane, and Yoshio Arai, "*Enhanced photoluminescence of InGaAs/GaAs quantum dots induced by nanoprobe pressure effects*", Applied Physics Letters 83(11), 2247 (2003).

[43] A. M. Mintairov, K. Sun, J. L. Merz, C. Li, A. S. Vlasov, D. A. Vinokurov, O. V. Kovalenkov, V. Tokranov, and S. Oktyabrsky, "*Nanoindentation and near-field spectroscopy of single semiconductor quantum dots*", Physical Review B 69, 155306 (2004).

[44] Kazunari Ozasa, Yoshinobu Aoyagi, Masahiko Hara, Mizuo Maeda, Akihiko Yamane, and Yoshio Arai, "*Enhanced photoluminescence of InGaAs quantum dots induced by nanoprobe indentation*", Physica E 21, 265-269 (2004).

[45] Yuan-Hua Liang, Yoshio Arai, Kazunari Ozasa, Masane Ohashi, and Eiichiro Tsuchida, "*Simultaneous measurement of nanoprobe indentation force and photoluminescence of InGaAs/GaAs quantum dots and its simulation*", Physica E 36, 1-11 (2007).

[46] Yuan-Hua Liang, Masane Ohashi, Yoshio Arai, and Kazunari Ozasa, "*Location of quantum dots identified by microscopic photoluminescence changes during nanoprobe indentation with a horizontal scan*", Physical Review B 75, 195318 (2007).

[47] Kazunari Ozasa, Mizuo Maeda, Masahiko Hara, Masane Ohashi, Yuan-Hua Liang, Hiroki Kakoi, and Yoshio Arai, "*Localized strain effects on photoluminescence of quantum dots induced by nanoprobe indentation*", Physica E 40, 1920-1923 (2008).

Chapter 2

Experimental setup and methodologies

2.1 Self-assembled InGaAs/GaAs QDs

2.1.1 Preparation of the QDs sample

The QDs measured in this study is the InGaAs quantum dots self-organizing on a substrate of GaAs(001) based on the strain-induced Stranski-Krastanow (SK) growth mode. The QDs sample was prepared in a conventional Chemical Beam Epitaxy (CBM) system in three steps.

Chemical Beam Epitaxy (CBM) [1-4] is a variant of molecular beam epitaxy (MBE) that uses the organic precursors of metal-organic chemical vapour deposition (MOCVD), exploiting advantages of both techniques. In the CBE system, the main experimental setups are: an ultra-high vacuum (UHV) growth chamber, a pressure-controlled gas inlet system, as well as the reflection high-energy electron diffraction (RHEED) equipment. The UHV chamber, which is equipped with a liquid nitrogen cryoshield outside surrounding and a rotatable crystal holder inside, is where the epitaxial growth takes place. The crystal holder is heated from the backside to temperatures of 500 to 700 ℃. The gas inlet system is used to supply the gaseous group Ⅲ and Ⅴ alkyls as the material sources into the growth chamber by controlling the input pressure of the gas injection capillary. For the group Ⅴ starting material, the hydrides have also to be precracked into the injector by thermally decomposing with a heated metal or filament. In this study, we have used triethylgallium (TEGa) and trimethylindium (TMIn) for the metal sources and precracked AsH_3 to supply As_2. The supply rates of these sources were specified by giving the control pressures. Figure 2.1 shows a schematic illustration of the epitaxial growth in the CBM system [5]. When the group Ⅲ alkyl molecules (TEGa or TMIn) impinged onto the heated substrate, the group Ⅲ elements (Ga or In) were generated from the pyrolysis of the alkyls on the substrate surface,

$$\begin{aligned} &TEGa \rightarrow Ga+CH_4/C_2H_4, \\ &TMIn \rightarrow In+CH_4/C_2H_4. \end{aligned} \tag{2.1}$$

Meanwhile, the group Ⅴ element (As) was derived from the decomposition of the alkyl with

a heated metal in the gas injection system,

$$AsH_3 \rightarrow As_2 + H_2, \tag{2.2}$$

and reached the substrate surface due to diffusion. As soon as the group Ⅴ atoms migrated into the appropriate lattice sites and deposited near group Ⅲ atoms, the epitaxial growth took place. The in situ monitoring of surface superstructures on the growing surface can be achieved by using the RHEED equipment. In other words, the real-time two-dimensional-to-three-dimensional transition can be obtained through analyzing the intensity changes of the RHEED transmission spot.

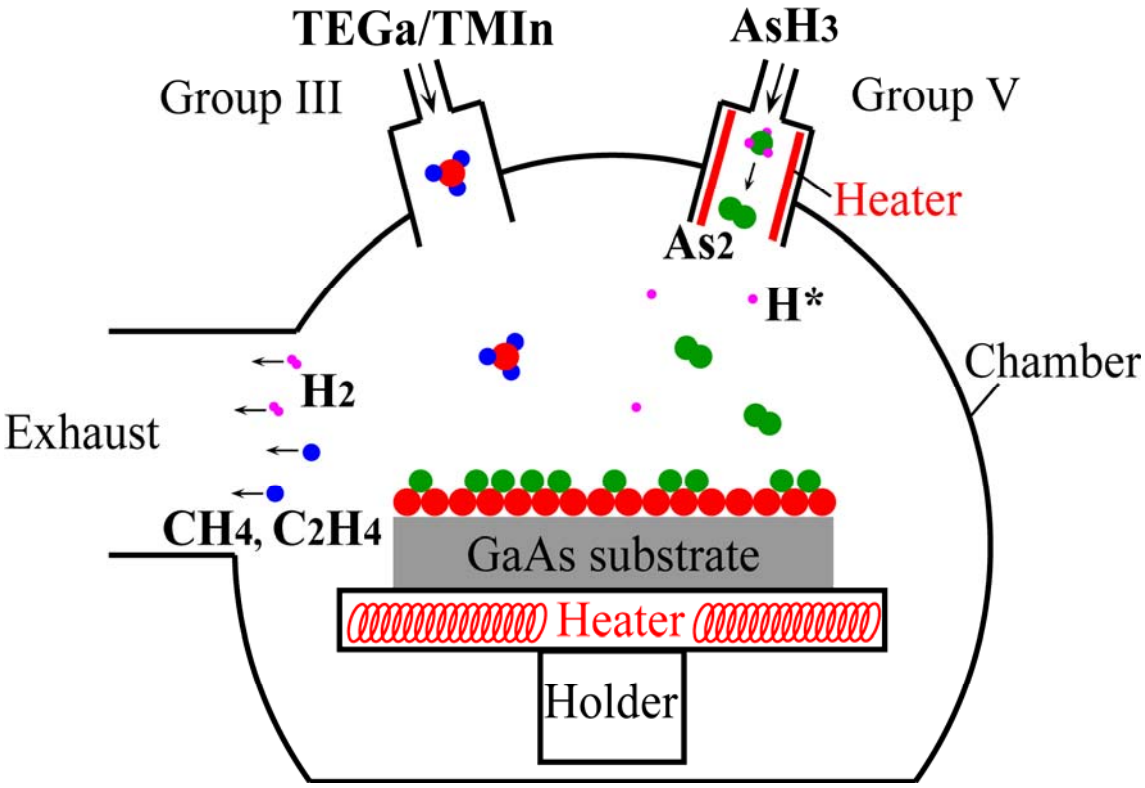

FIG. 2.1 Schematic illustration of the epitaxial growth in the chemical beam epitaxy (CBE) system.

Based on the growth principles and RHEED pattern detections in the CBE system as mentioned above, the preparation of the InGaAs/GaAs quantum dots studied in this research was performed in three steps, as illustrated in Fig. 2.2.

Firstly, a GaAs buffer layer of 70 nm thickness was grown at 580 ℃ on a substrate of

GaAs, the top surface of which was thermally cleaned before. The supply of the TEGa beam had an equivalent pressure of 1.8×10^{-4} Pa, while the precracked AsH_3 was provided with a flow of 1.0 sccm. After the substrate temperature decreased to 480 ℃, the GaAs growth was restarted with the same flux of TEGa and AsH_3.

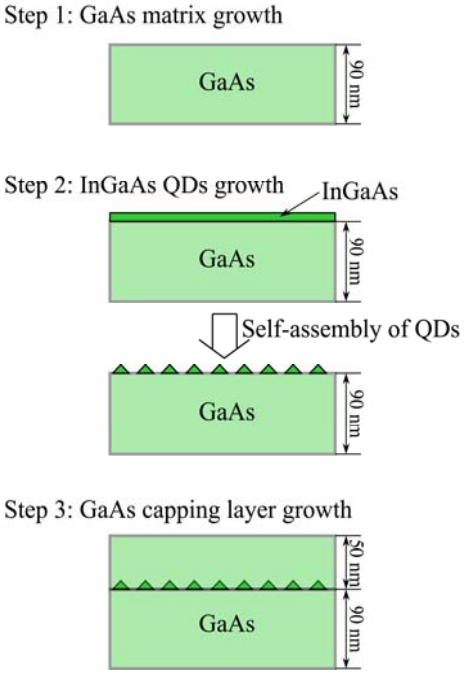

FIG. 2.2 Preparation steps of the self-assembled InGaAs/GaAs QDs sample. The dimensions in the figure are not to scale.

Secondly, when the thickness of the regrown GaAs layer in the first step reached 20 nm, the TMIn beam was delivered into the growth chamber without interrupting the GaAs growth. The equivalent pressure of the TMIn beam was 5.7×10^{-5} Pa. Based on the source beams (TEGa, TMIn, and AsH3) supplied with the above mentioned pressures, the growth rate of InGaAs layer was calculated to be 0.27 monolayers (MLs)/s. From the X-ray diffraction measurement of 1000 nm InGaAs epilayer individually prepared under the same conditions, the indium fraction in InGaAs was estimated to be 0.52 (estimation error was ±6%). The real-time monitoring of the sample surface structures was realized by using the RHEED. From the RHEED intensity increase, the onset of the three-dimensional InGaAs dot formation due to strain-relaxation mechanism (SK mode) was detected [6, 7]. At this point, the supply of

TEGa and TMIn beams was stopped simultaneously, and the deposited InGaAs layer was evaluated to be 8.4 ML at this point from the growth rate as well as taking account of the delay time for the TMIn beam.

Lastly, a GaAs layer with a thickness of 50 nm was grown again at 480 ℃ under the same condition as that in the first step, covering the self-assembled QDs in the matrix, as shown in Fig. 2.2. All the structures prepared in all steps were not intentionally doped. Since the QDs were embedded at the 50-nm deep layer, it is impossible to identify the QDs' location through microscopic observation.

2.1.2 Microscopic observation of the QDs sample

The three-dimensional (3D) observation of the QDs sample, prepared as described in Sec.2.1.1, was achieved by fabricating a fine cylindrical specimen and observing the specimen three dimensionally with specimen rotation using the scanning transmission electron microscope (STEM).

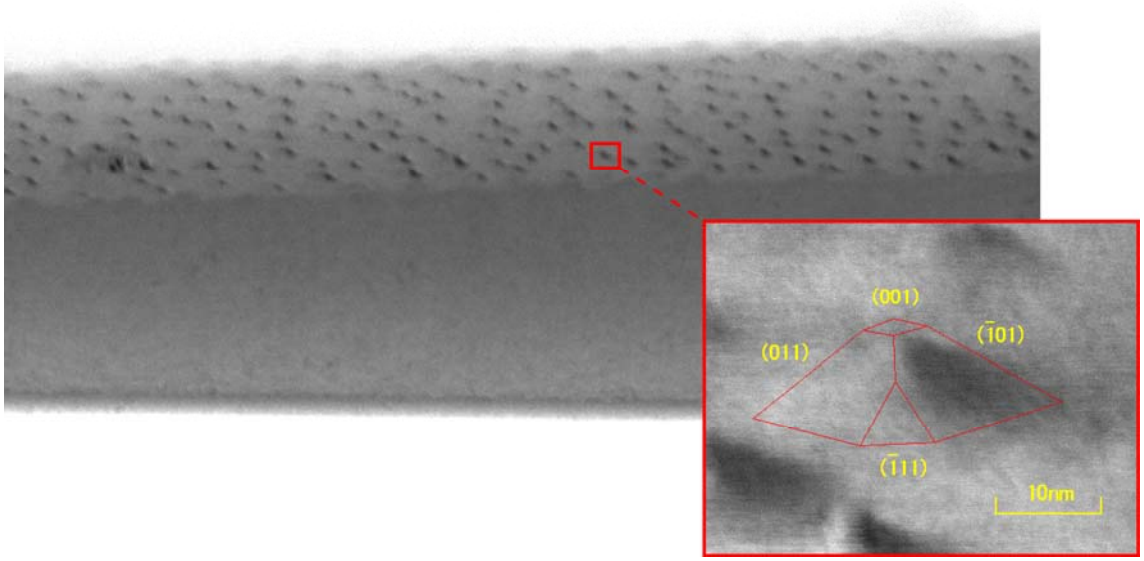

FIG. 2.3 Scanning transmission electron microscopic (STEM) image of the QDs sample. The insert shows the reconstructed facet pyramid of one single QD.

The fabrication of a fine cylindrical specimen was first performed by using focused ion

beam (FIB) and micro sampling for cutting, mounting, and thinning the specimen [8]. After a piece of cylindrical specimen with a diameter of approximately 200 − 300 nm was prepared, the specimen was mounted on a metal (Mo) cylinder base (0.9 mm diameter, 3.9 mm long). In order to obtain both the cross-sectional and plan-view images of the QDs sample, the rotation axis of the cylinder base was adjusted to the <331> direction, along which the specimen contains the interface of QDs/capping layer. For 3D observation, STEM was used. The STEM system was operated with a 300 kV field-emission electron beam (typically 10-30 μA), and equipped with two alternative electron detectors. From the microscopic images of the QDs sample [9], as shown in Fig. 2.3, the density of QDs was estimated to be approximately 5 − 6 $\times 10^{10}$ cm^{-2}. Typical QDs have pyramidal shapes with a square base of 20 nm and a height of 7 nm.

2.2 Nanoprobe fabrication

The nanoprobe, which was used to introduce the strain fields through probing onto the QDs sample in this study, either with a flat cylindrical apex or dome-shaped apex, was obtained by fabricating the tip of transparent tapered probe using FIB. The tapered probe, which is made of quartz, was prepared by using a pulling technique [10, 11] and coated by Au beforehand. FIB technique was then adopted to fabricate the probe tip with a designed shape/size (flat or dome-shaped). The FIB system used in this study was a Hitachi model FB-2000. After the tapered probe was loaded into the FIB machine and adjusted to an appropriate position/direction, clear images of the probe can be seen from the connected monitor, as shown in Fig. 2.4 (a). The FIB machine was working in a low density beam model in the probe imaging. Further modifications of the probe position/direction were carried out until the probe was adjusted to parallel to the vertical edge of the monitor. Then, in the imaging window, a mark of rectangle or dome, depending on the shape of the designed probe, was made to mark the part of the probe tip which will be removed, as illustrated in Fig. 2.4 (b). The marked part of the probe tip was removed with the focused gallium ions beam (10 nm beam) scanned within the marked area. The FIB machine was working in a high power model for the removal of the marked part of the tip. The images of the fabricated flat cylindrical and dome-shaped nanoprobes used in this study are shown in Fig. 2.4 (c) and (d), respectively.

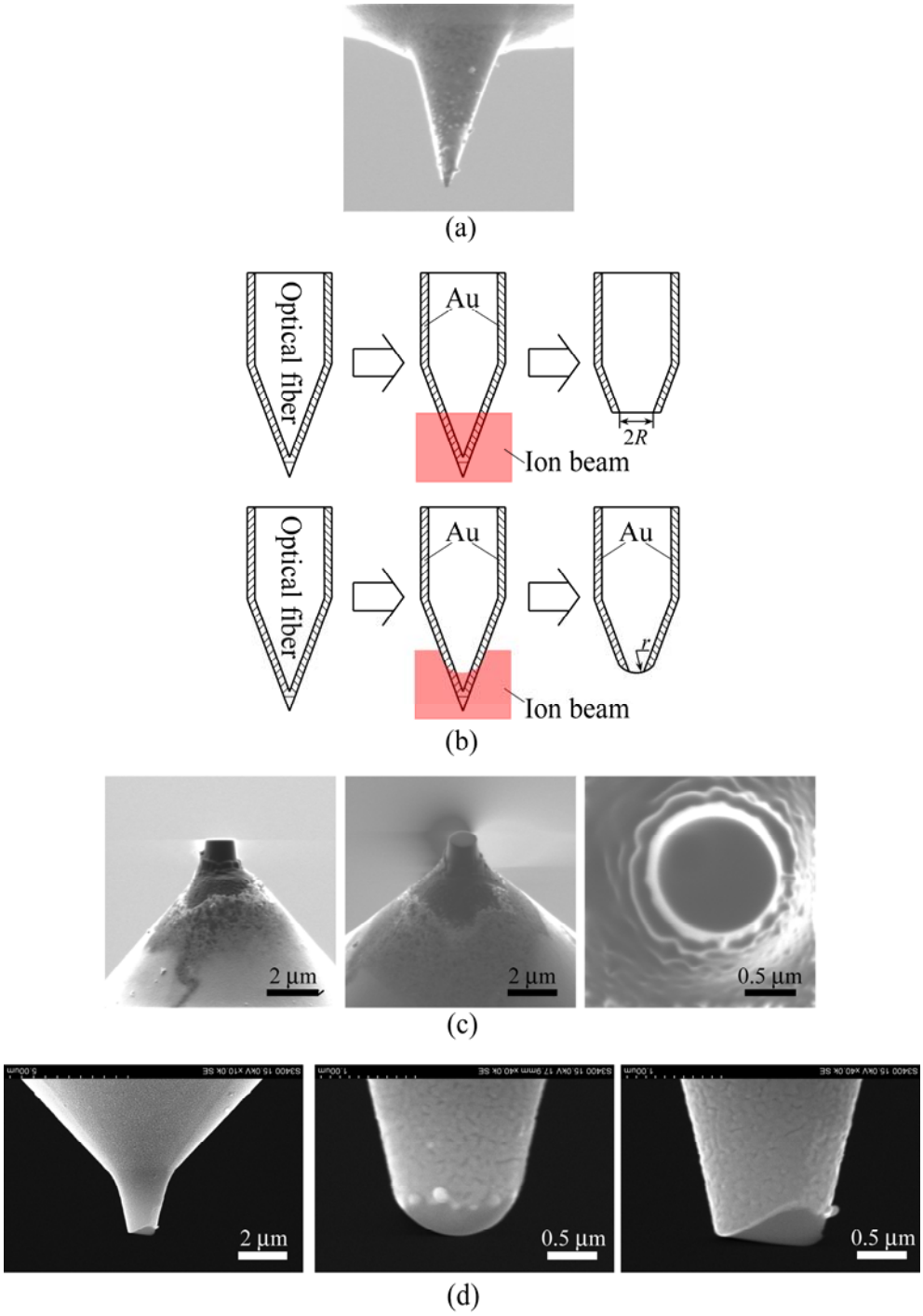

FIG. 2.4 (a) Scanning ion microscopic (SIM) image of the unfabricated nanoprobe, (b) illustration of the design and fabrication of the flat cylindrical (top) and dome-shaped (bottom) apex, (c) SIM images of the fabricated flat cylindrical nanoprobe (R=600 nm) with side view (left), 45 degree view (middle) and top view (right), and (d) scanning electron microscopic (SEM) images of the fabricated dome-shaped nanoprobe from different sides of view (Hitachi, S-3400N). In (d), the bottom length L of the dome-shaped probe was measured as 890 nm (left and right images in (d)), and the dome radius r was 640 nm (middle image in (d)).

2.3 Experiment setup

Near-filed photoluminescence (PL) measurements were carried out in a nanoprobe PL system that can operate the Au-coated fiber probe in a low temperature (10 K) using the apparatus of a liquid-He-cooled scanning tunneling microscope (STM; Unisoku, USM-100R) under ultra-high vacuum (approximately 4×10^{-9} Pa), as schematically depicted in Fig. 2.5. In this system, a so-called collection mode was employed, that is, far-filed excitation to the region around the tip and PL collection through the probe aperture from the direct beneath area. The far-field excitation was realized by a SHG-YAG2 laser (532 nm, 540 mW/cm^2) with an incidence angle of 45°. The PL emission from QDs was collected through the optical fiber aperture, and the PL spectrum was analyzed by a 0.3 m focal length monochromator (SPEX, 270 M) together with a liquid-N2-cooled CCD detector (SPEX, CCD-200). The spectral resolution of our near-field PL system was approximately 0.5 meV. In addition to collecting the PL signal, the other role of the nanoprobe was to introduce indentation onto the sample surface within the elastic limit of probe and QD sample. The indentation force, *F*, was applied through the piezo-driven nanoprobe by increasing the vertical displacement (*z*) of the probe, and measured by a high-sensitivity loadcell (Tokyo Sokki, CLS-1NLS) placed under the QDs sample. The lateral position of the probe was located by the displacement in *x* and *y*. Since the sample surface beneath the probe was shadowed by the probe itself, the PL was caused by the diffusion of photocarriers generated outside of the probe shadow, as illustrated in Fig. 2.5.

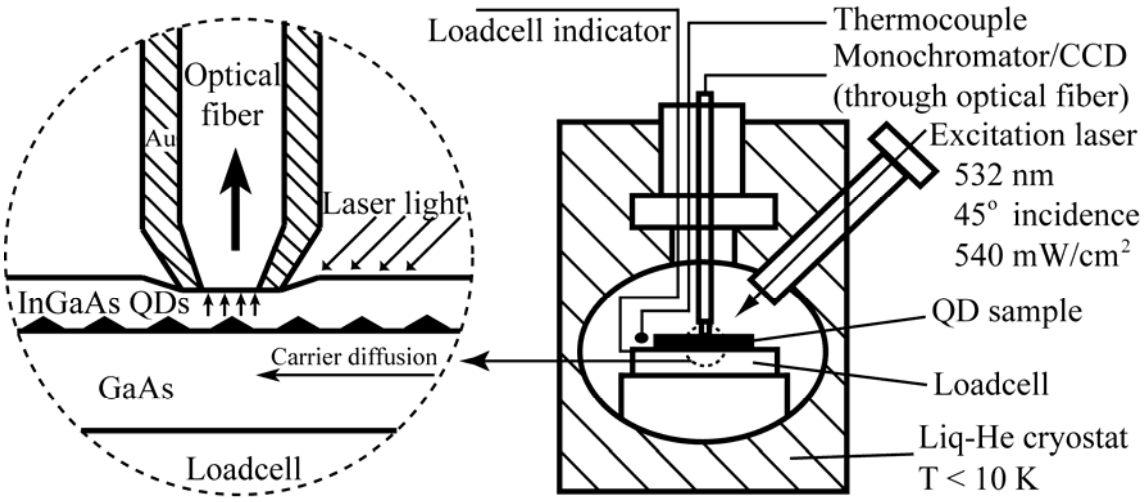

FIG. 2.5 Schematic diagram of nanoprobe PL measurements with a liquid-He-cooled STM. An Au-coated optical fiber was used to detect the PL, while laser excitation was realized through an optical window.

2.4 Nanoprobe indentation experiments

There are two types of nanoprobe indentation experiments (within the limit of elastic deformation) performed in this study, *stationary indentation* and *scanning indentation*.

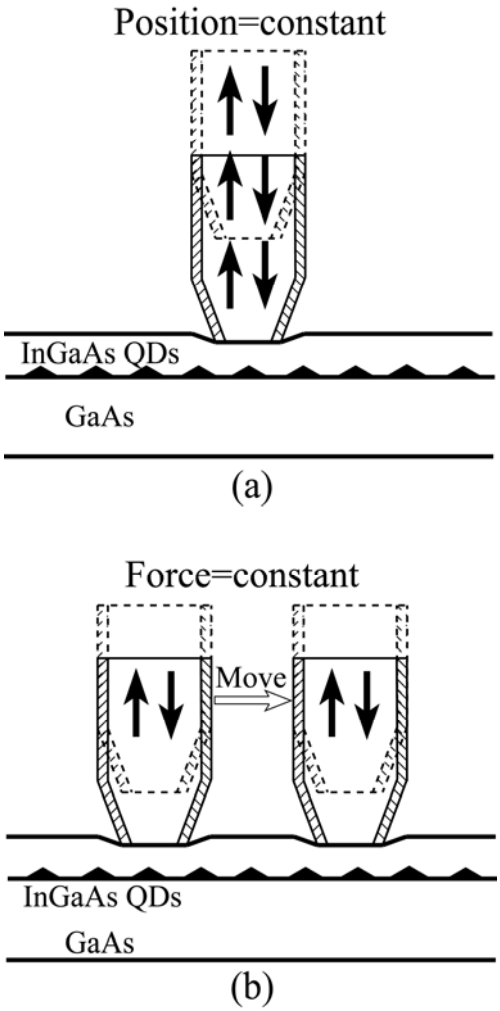

FIG. 2.6 Illustration of the performance of (a) stationary indentation at a fixed indentation position, (b) scanning indentation with a fixed indentation force.

In the stationary indentation, the probe was indented down /up stepwise at a fixed position on the sample surface with the indentation force loaded/unloaded with a constant increment/decrement, as illustrated in Fig. 2.6 (a). The PL spectrum from the strained QDs was measured at each step of the loading/unloading indentation. The PL spectra measured in the stationary indentation were used to obtain the dependence of the PL emission from QDs

on the applied indentation force, as well as the quenching phenomena of the QDs, which will be explained in details in Chapter 3.

In the scanning indentation, the probe was pressed up to a constant value of force at one indentation position, at where one PL spectrum from the QDs was collected. Then the probe was raised above the sample surface to a load-free state, moved with a constant distance, and pressed onto the sample with the same force for the next spectrum collection (horizontal scan of the probe with a fixed indentation force), as shown in Fig. 2.6 (b). The PL measurements in the scanning indentation were used to determine the QDs location by comparing the PL emission from the QDs to the simulation results, as reported in our previous reports [12, 13].

References

[1] W. T. Tang, "*Chemical beam epitaxy of InP and GaAs*", Applied Physics Letters 45, 1234 (1984).

[2] W. T. Tang, "*CBE of Ga0.47In0.53As/InP quantum wells and heterostructure devices*", Journal of Crystal Growth 81, 261 (1987).

[3] M. S. Miller, S. Jeppesen, D. Hessman, B. Kowalski, I. Maximov, B. Junno, and L. Samuelson, "*Assembling strained InAs islands by chemical beam epitaxy*", Solid-State Electronics 40, 609-614 (1996).

[4] http://en.wikipedia.org/wiki/Chemical_beam_epitaxy

[5] http://vcsel-www.pi.titech.ac.jp/coe/vcsel/CBE/CBEindex.html

[6] K. Ozasa, Y. J. Park, Y. Aoyagi, and L. Samuelson, "*Reversible transition between InGaAs dot structure and InGaAsP flat surface*", Applied Physics Letters 71(6), 797 (1997).

[7] K. Ozasa, and Y. Aoyagi, "*In situ composition control of self-organized InGaAs dots*", Journal of Crystal Growth 188, 370-376 (1998).

[8] K. Ozasa, Y. Aoyagi, M. Iwaki, M. Hara, and M. Maeda, "*Nanofabrication of cylindrical STEM specimen of InGaAs/GaAs quantum dots for 3D-STEM observation*", Ultramicroscopy 101, 55-61 (2004).

[9] K. Ozasa, Y. Aoyagi, M. Iwaki, and H. Kurata, "*Facets, indium distribution, and lattice distortion of InGaAs/GaAs quantum dots observed by three-dimensional scanning transmission electron microscope*", Journal of Applied Physics 94(1), 313-317 (2003).

[10] D. W. Pohl, W. Denk, and M. Lanz, "*Optical stethoscopy: Image recording with resolution λ/20*", Applied Physics Letters 44(7), 651 (1984).

[11] A. Lewis, M. Isaacson, A. Harootunian, and A. Muray, "*Development of a 500 A spatial resolution light microscope: I. light is efficiently transmitted through λ/16 diameter apertures*", Ultramicroscopy 13(3), 227-231 (1984).

[12] Yuan-Hua Liang, Masane Ohashi, Yoshio Arai, and Kazunari Ozasa, "*Location of quantum dots identified by microscopic photoluminescence changes during nanoprobe indentation with a horizontal scan*", Physical Review B 75, 195318 (2007).

[13] Yuan-Hua Liang, "*Nanoprobe indentation on quantum dots with photoluminescence measurement: strain distribution, energy shift, and location identification*", Doctoral thesis of Saitama University, (2007).

Chapter 3

Experimental results

3.1 Results of stationary indentation with a flat cylindrical nanoprobe

PL spectrum from the strained QDs was measured at each indentation step in the stationary indentation. Figure 3.1 shows a representative set of PL spectra under different indentation forces introduced by the flat cylindrical nanoprobe with a radius of 600 nm. One step of the indentation force was 0.06 mN. The applied maximum force was approximately F=3.5 mN. The usage of a nanoprobe with dimensions of several hundreds nanometers enables us to achieve the well resolved PL emissions from single QD with the QDs density of $5 - 6\times10^{10}$ cm^{-2} [1-3]. As shown in Fig. 3.1, when a non-zero indentation force was applied, fine PL peaks (about 4 meV in width at half-peak energy) emitted from individual QDs, such as QD1, QD2, QD3, and QD4 in Fig. 3.1, was observed. This means the PL from single QD is noticeably enhanced by the indentation-induced strain. The number of fine peaks observed was 20 － 30 in the full PL spectrum individually for indentation forces from 0.1 up to 3.5 mN, as shown in Fig. 3.1. The spectrum measured at 2.34 mN was necessary to determine the corresponding QDs of these four QDs observed in scanning indentation, which will be explained in Sec. 3.2. As shown in Fig. 3.1, the PL peak energy of each single QD is blueshifted with the increment of indentation force, while the PL intensity first increases, followed by a decrease, and is finally quenched. As presented in our previous reports, the blueshift of the peak energy is mainly attributed to the upward shift of the Γ conduction band due to indentation [4, 5], while the increment of the PL intensity (PL enhancement) is caused by the hole-accumulation around the nanoprobe edge [6].

By combining all the PL spectra measured at step-by-step indentation forces, the dependence of PL peak energy and PL intensity on indentation force can be obtained as shown in a diagram included in Fig. 3.2. Loading and corresponding unloading cases are included in Fig. 3.2. Each diagram consists of 67 narrow slices, and one single slice represents a PL spectrum under a given indentation force. The brightness corresponds to the PL intensity. As reported in Ref. 6, the complete symmetry of the loading and unloading diagrams indicates that the changes in the PL peaks from QDs are reversible even though the

force is applied up to a high level (larger than the quenching force of several QDs). The quenching force of a specific QD in the loading process is the same as the initiating force in the unloading process. In other words, elastic deformation dominated the quenching and restart of PL in our experiment.

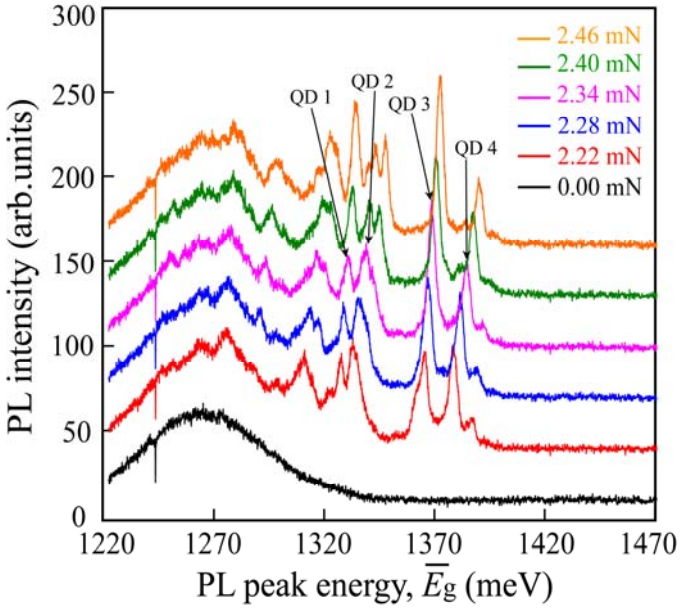

FIG. 3.1 A representative set of the PL spectra from the QDs measured in the stationary indentation at various indentation forces. The probe used for the indentation was a flat cylindrical probe with a radius of 600 nm.

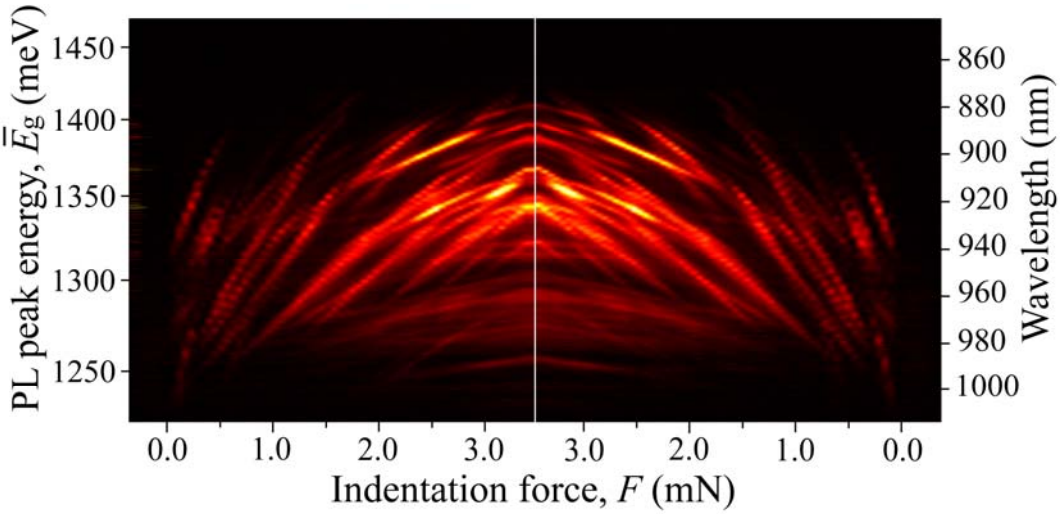

FIG. 3.2 Dependence of PL peak energy/PL-intensity on the indentation force for loading (left) and unloading (right) cases (R=600 nm).

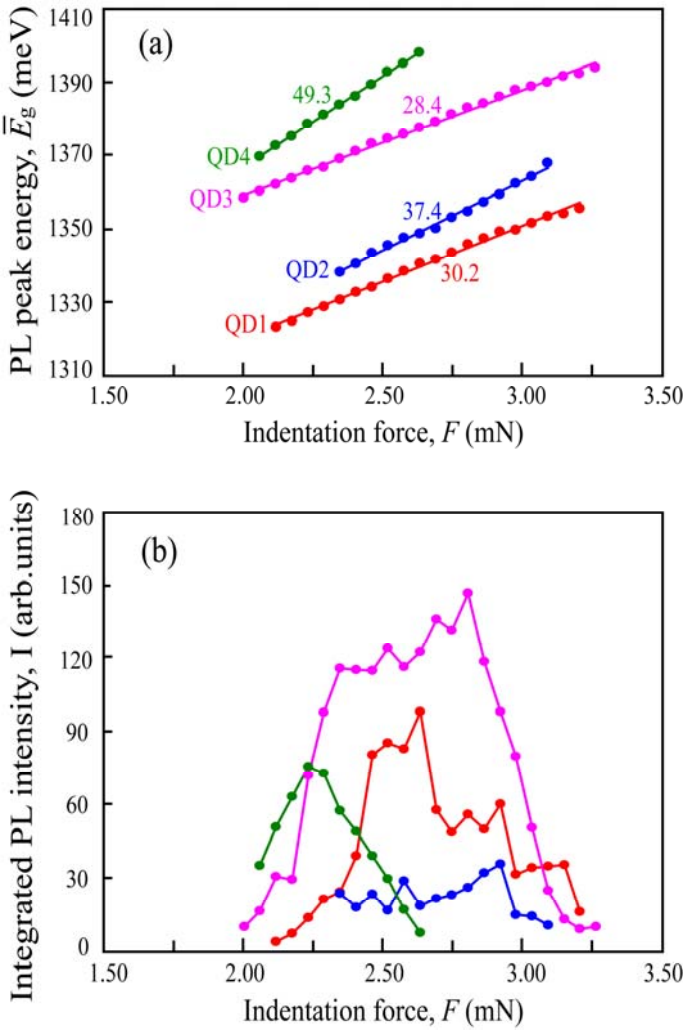

FIG. 3.3 Dependence of (a) PL peak energy and (b) integrated PL intensity of typical QDs on indentation force (R=600 nm). The straight lines in (a) linearly fit the experimental points of one single QD. The slope of each line gives the blueshift rate, $\Delta\overline{E}_g / \Delta F$, values of which are attached to the line (unit: meV/mN). The short lines in (b) are used to connect the neighboring points as a guide for eyes.

By tracing the peak energies and integrating the PL intensity for some typical fine PL peaks with the increment of force, we obtained their dependences on the indentation force. Figure 3.3 shows these dependences for the numbered QDs (QD1, QD2, QD3 and QD4) in Fig. 3.1. From Fig. 3.3, we can see that the integrated PL intensity increases and then decreases with indentation force, while the peak energy is blueshifted linearly. The peak energy shift per unit force is defined as the blueshift rate $\Delta\overline{E}_g/\Delta F$ taking the unit of

meV/mN. The value of $\Delta\overline{E}_g/\Delta F$ for each QD was measured as the slope of the linear fitting line of the experimental data for each QD, labeled with numbers in Fig. 3.3 (a). The measured blueshift rate is used to determine the QD location relative to the probe center, which will be explained in details in Sec. 5.2. In Fig. 3.3 (b), the force at which the integrated PL intensity becomes zero is the quenching force F_q. The PL energy blueshifts and PL intensity changes for bulk GaAs [7] and InGaAs/GaAs QDs [8] have also been reported under the uniform hydrostatic pressure.

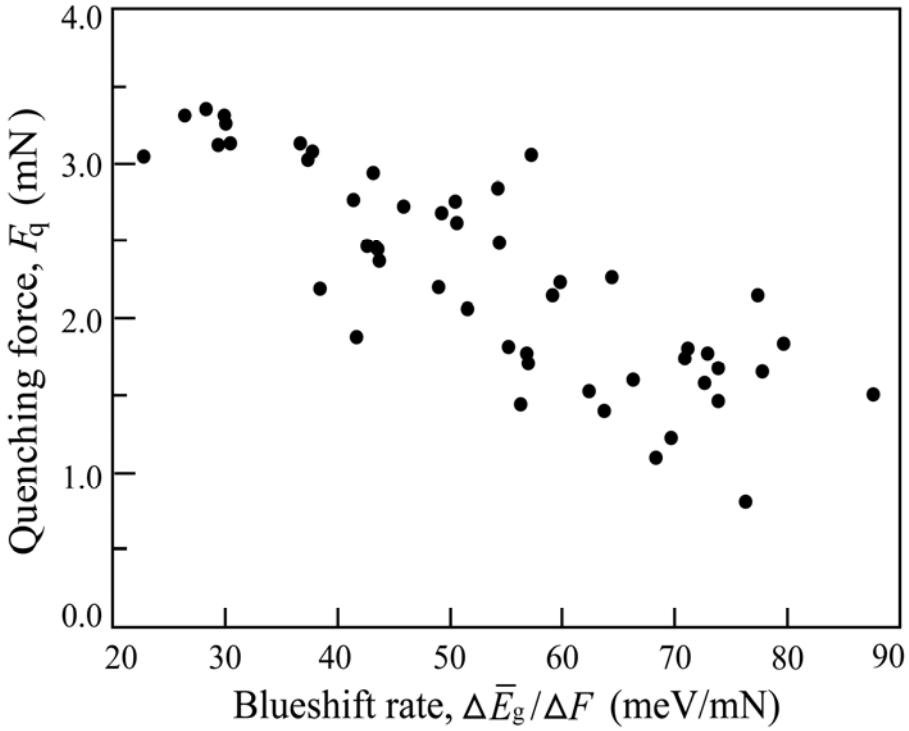

FIG. 3.4 Experimental result of the relationship between quenching force and blueshift rate. The probe radius is 600 nm.

Based on the foregoing analysis, two parameters—blueshift rate and quenching force—are associated with the quenching behavior. The relation between quenching force and blueshift rate obtained from Fig. 3.3 is plotted in Fig. 3.4. Although the experimental data are scattered in Fig. 3.4, it is clear that the indentation force required to quench the PL from a single QD tends to decrease as the blueshift rate increases. This negative trend is attributable to the relative location of the QD from the probe center. As the relative location of the QD decreases, the blueshift rate increases while the quenching force is required to decrease. The

data scattering is probably caused by the imperfect circularity of the nanoprobe apex as well as by the nonuniformity of the shape (height to width ratio) of each QD and the indium composition inside them.

3.2 Results of scanning indentation with a flat cylindrical nanoprobe

As mentioned in Sec. 3.1, the blueshift rate of each QD measured with the stationary indentation will be used to estimate the QD location in Sec. 5.2. In order to evaluate the accuracy of this estimation method, scanning indentation was also performed to identify the QDs' location. In the scanning indentation, the PL spectrum was measured at each indentation position under the fixed force of 2.34 mN. Since the PL enhancement was found for the force from 0.1 up to 3.5 mN in the stationary indentation, the force of 2.34 mN was adopted as a typical one applied in scanning indentation under which the PL emission from single QDs were clearly resolved. The trace of the movement of the indentation position in the scanning indentation included the indentation positions from the experiments with stationary indentation, as shown in Fig. 3.5. In Sec. 3.1, two groups of stationary indentation were performed at the fixed position of (35.5, 0) and (46.7, 0), respectively. In the scanning indentation, the probe was moved with one step of 1.87 nm from (0, 0) to (91.5, 0), as shown in Fig. 3.5. This enabled us to find out the same QDs observed in the stationary and scanning indentations, respectively.

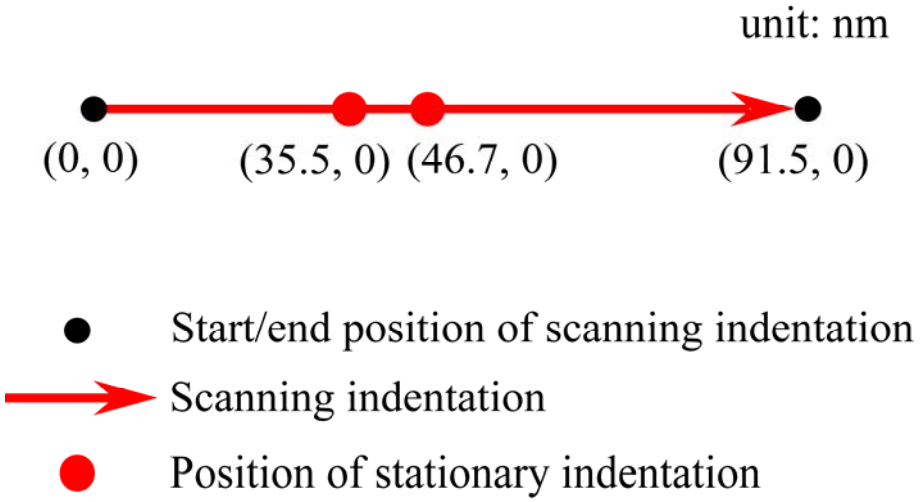

FIG. 3.5 Illustration of the trace of probe movement in the scanning indentation experiment using a flat cylindrical nanoprobe.

The PL result of scanning indentation induced by the flat cylindrical probe (R=600 nm) is shown in Fig. 3.6. In this figure, a vertical slice contains a PL spectrum collected at a given probe location under the constant force of 2.34 mN. The brightness corresponds to the PL intensity. The bright streaks (traces) show the shift of the emission energy of individual QD due to the indentation of nanoprobe with scan. As reported in our previous studies [5, 9], the different shapes in the traces of the emission energy of QDs indicate the different locations of QDs relative to the nanoprobe, and the locations of the embedded InGaAs/GaAs QDs were successfully determined by combining the PL results of scanning indentation and the quantitative analysis of the indentation-induced strains and energy shifts. Details of scanning indentation and the method for identifying the QDs' location through scanning indentation are reported in Ref. 9. In this study, we will directly use the results of the QDs' location identified by scanning indentation for comparison with the estimates from the blueshift rate obtained from stationary indentation.

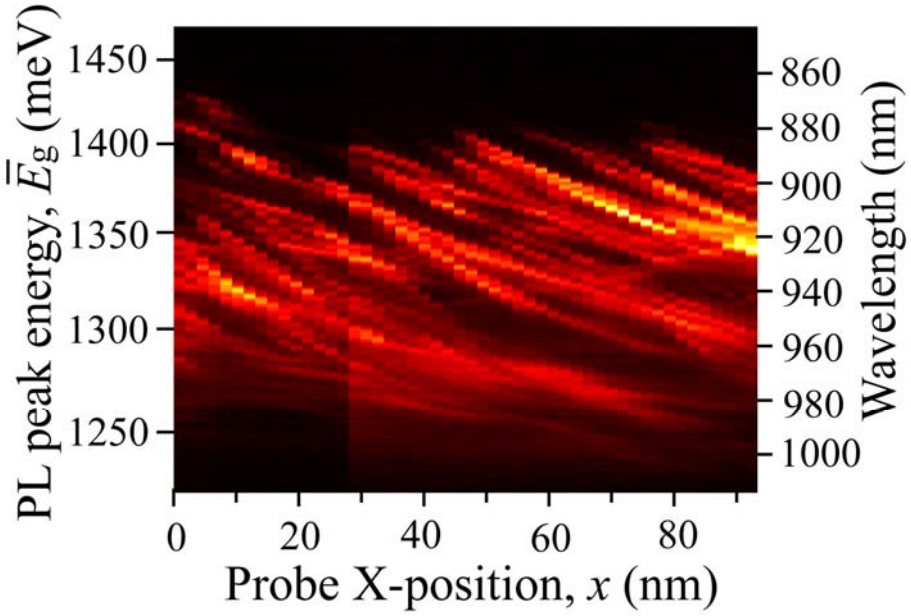

FIG. 3.6 Dependence of PL peak energy/PL-intensity on the probe position in the scanning indentation using a flat cylindrical probe (R=600 nm). The indentation force is F=2.34 mN.

Figure 3.7 shows the spectra collected at the same indentation position and under the same indentation force, but from stationary and scanning indentation, respectively. In Fig. 3.7,

Spectrum-1 was obtained from stationary indentation (at the position of (46.7, 0) in Fig. 3.5) when the applied indentation force equaled the force (F = 2.34 mN) used for scanning indentation. This spectrum is the same as that in Fig. 3.1 at a force level of 2.34 mN. The other spectrum, Spectrum-2 in Fig. 3.7, was obtained from scanning indentation when the probe was indented at (46.7, 0) where stationary indentation was performed. The correspondence of the PL peaks for each QD (QD1, QD2, QD3, and QD4) in these two spectra enabled us to make the QDs observed with stationary and scanning indentation correspond exactly, as shown in Fig. 3.7.

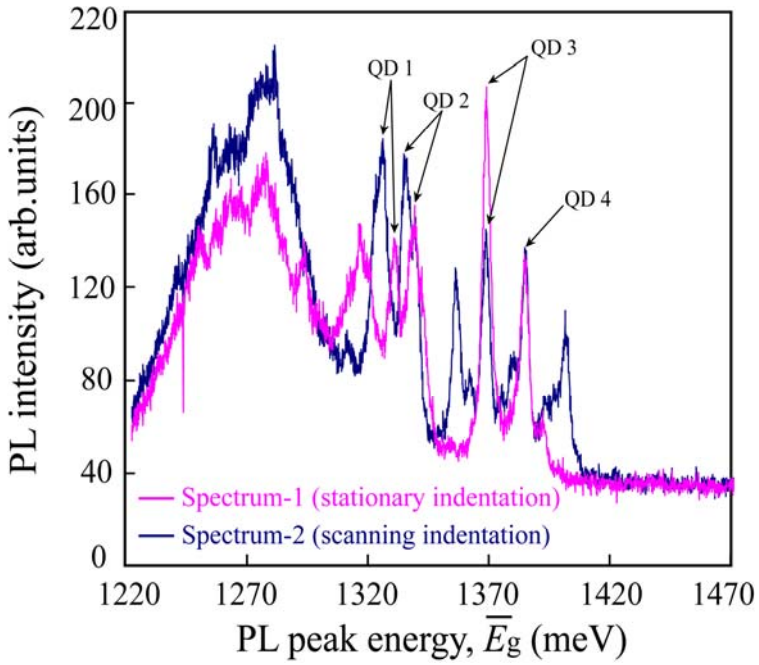

FIG. 3.7 The spectra used to find the QDs observed in the scanning indentation corresponding to those observed in the stationary indentation. The Spectrum-1 was obtained in the stationary indentation (Fig. 3.2), the same as the spectrum in Fig. 3.1 at the force level of 2.34 mN. The Spectrum-2 was obtained in the scanning indentation (Fig. 3.6) at the position of (46.7, 0).

Based on the corresponding spectra as shown in Fig. 3.7, the traces of the emission energy of the QDs, which were observed in stationary indentation (QD1, QD2, QD3, and QD4 in Fig. 3.1), were found in the scanning indentation, as shown in Fig. 3.8. These traces from scanning indentation were used to identify the QDs location with least squares method as reported in Ref. 9.

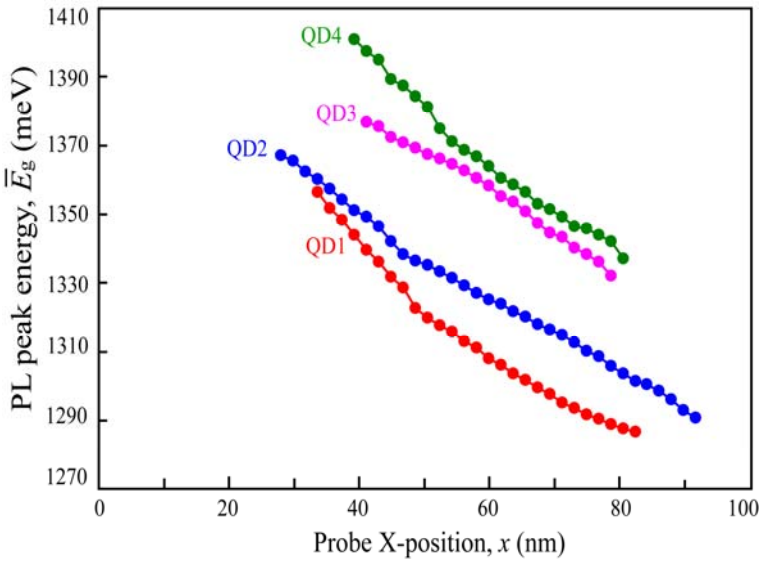

FIG. 3.8 PL peak traces of typical QDs in the scanning indentation.

3.3 Results of scanning indentation with a dome-shaped nanoprobe

Using the dome-shaped nanoprobe (Fig. 2.4(d)), experiment of scanning indentation was carried out. In the experiment, the probe was scanned along the *y*' direction with 6.6 nm in one step of movement. The relative relation between the tip's dome shape and the scan direction is illustrated in Fig. 3.9. The *x'y'z'* coordinate defined in this figure will be adopted in the simulation in following chapter. The scan sequence (so called *y*-scan in the following) was repeated 150 times, deducing a distance of 983 nm in the probe movement. Since the PL enhancement was observed on the contact of probe to the sample surface as found in the flat cylindrical probe case, the force of 1.14 mN was adopted as a typical one applied in the *y*-scan, under which PL emissions from single QD were clearly resolved.

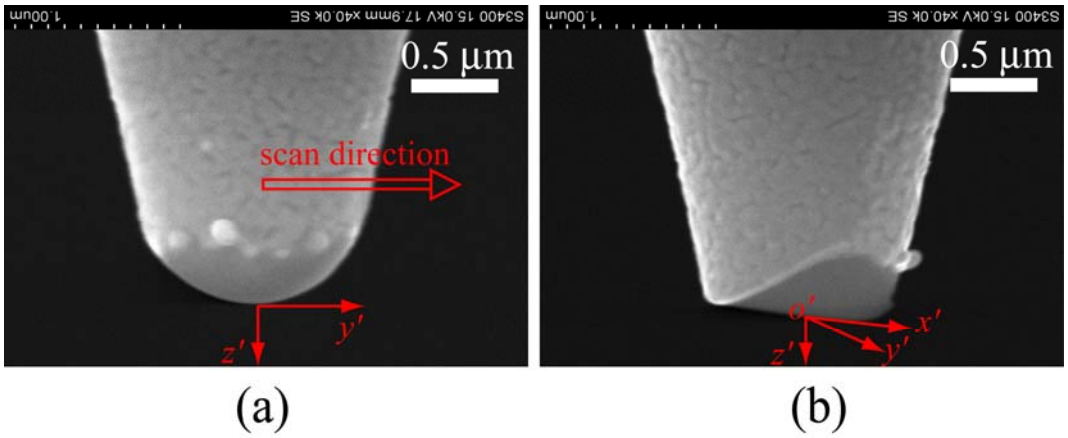

FIG. 3.9 Illustration of the direction of scan relative to the dome-shaped probe.

Figure 3.10 shows the PL results obtained with the *y*-scan under the fixed force of 1.14 mN using the dome-shaped probe. PL emissions from single QDs were enhanced with the indentation and shifted with the probe movement. Most interesting thing in Fig. 3.10 is that the PL emissions from some QDs (QD1 to QD11 as illustrated in Fig. 3.10) were firstly blueshifted then symmetrically redshifted with the probe position movement. This was not observed in the scanning indentation of flat cylindrical probe (Fig. 3.6). From Fig. 3.10, we directly obtained the positions of some QDs (QD1 to QD11 in Fig. 3.10) in the *y* coordinate, at which the PL emissions of those QDs reach the maximum values. Detailed discussions will be presented in Sec. 5.3.

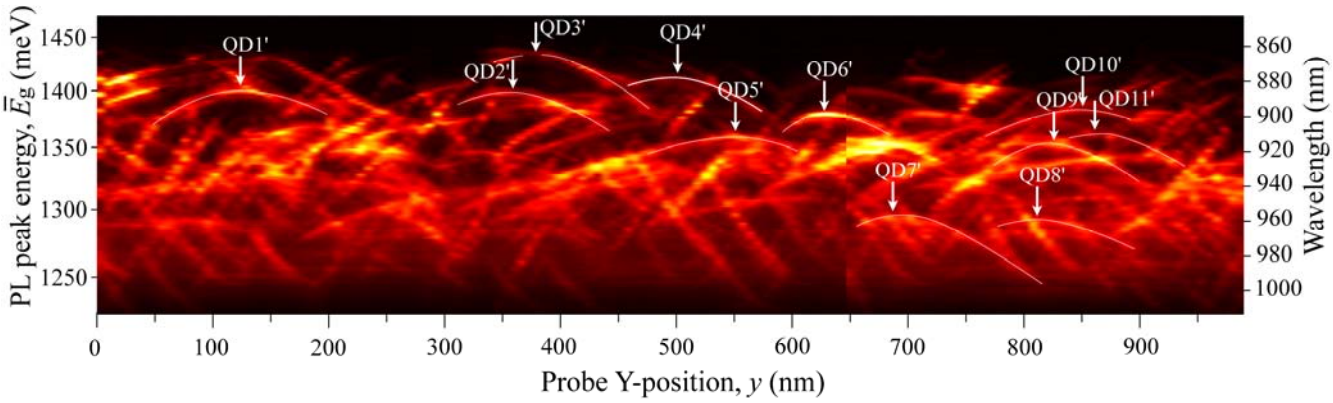

FIG. 3.10 Dependence of PL peak energy/PL-intensity on the probe *y* position in the scanning indentation using a dome-shaped probe (*r*=640 nm, *L*=890 nm). The indentation force is *F*=1.14 mN.

3.4 Summary

With the effect of strain fields induced by the indentation of a flat cylindrical or dome-shaped nanoprobe, PL emissions from InGaAs/GaAs QDs were remarkably enhanced. Under the stationary indentation of flat cylindrical nanoprobe, the enhanced PL emission from single QD was observed to be linearly blueshifted with the indentation force, while the integrated PL intensity first increased, then decreased and finally disappeared. The measured quenching force was found to vary from QD to QD, and therefore can be related to the location of individual QD with respect to the probe center, which can be determined from the measured blueshift of PL emission. Using the dome-shaped probe to perform the *y*-scan indentation, the obtained PL result exhibited characteristics different from that with the scanning indentation of flat cylindrical nanoprobe, since different strain fields were generated under the indentation of dome-shaped probe as compared to the flat cylindrical probe case. By analyzing this *y*-scan result, the locations of some of observed QDs were directly derived from the experiment, at where the PL emissions achieved the maximum values.

References

[1] K. Ozasa, S. Nomura, and Y. Aoyagi, "*Pressure effects on nanoprobe photoluminescence of quasi-zero-dimensional confinement quantum dots*", Superlattices and Microstructures 30(4), 169 (2001).

[2] K. Ozasa, Y. Aoyagi, A. Yamane, and Y. Arai, "*Enhanced photoluminescence of InGaAs/GaAs quantum dots induced by nanoprobe pressure effects*", Applied Physics Letters 83(11), 2247 (2003).

[3] K. Ozasa, Y. Aoyagi, M. Hara, M. Maeda, A. Yamane, and Y. Arai, "*Enhanced photoluminescence of InGaAs quantum dots induced by nanoprobe indentation*", Physica E 21, 265-269 (2004).

[4] Y.-H. Liang, Y. Arai, K. Ozasa, M. Ohashi, and E. Tcuchida, "*Simultaneous measurement of nanoprobe indentation force and photoluminescence of InGaAs/GaAs quantum dots and its simulation*", Physica E 36, 1-11 (2007).

[5] Y.-H. Liang, "*Nanoprobe Indentation on Quantum Dots with Photoluminescence Measurement: Strain Distribution, Energy Shift, and Location Identification*", Doctoral dissertation of Saitama University (2007).

[6] K. Ozasa, M. Maeda, M. Hara, M. Ohashi, Y.-H. Liang, H. Kakoi, and Y. Arai, "*Localized strain effects on photoluminescence of quantum dots induced by nanoprobe indentation*", Physica E 40, 1920-1923 (2008).

[7] D. J. Wolford, and J. A. Bradley, "*Pressure dependence of shallow bound states in gallium arsenide*", Solid State Communications 53(12), 1069-1076 (1985).

[8] S. G. Lyapin, I. E. Itskevich, I. A. Trojan, P. C. Klipstein, A. Polimeni, L. Eaves, P. C. Main, and M. Henini, "*Pressure-Induced Γ-X Crossover in Self-Assembled In(Ga)As/GaAs Quantum Dots*", Physica Status Solid (b) 211, 79 (1999).

[9] Y.-H. Liang, M. Ohashi, Y. Arai, and K. Ozasa, "*Location of quantum dots identified by microscopic photoluminescence changes during nanoprobe indentation with a horizontal scan*", Physical Review B 75, 195318 (2007).

Chapter 4
Calculation of strain and strain–induced energy shifts

4.1 Calculation of strain fields

In order to quantitatively explain the behavior of PL emissions from InGaAs QDs under the nanoprobe indentation as observed in the experiment, analysis of precious strain distribution in and around a QD caused by the lattice mismatch and indentation is of great importance, as well as the analysis of strain-induced modifications in the energy bands of QD and surrounding GaAs. Due to the significant influence of strain on the electronic and optical properties of QDs and the general application of high-performance computer, much work, especially theoretical and numerical work, has been done to calculate the strain/stress distributions in QD in recent years. Until now, a number of calculation methods have been developed, such as the analytical continuum approach based on Eshelby's inclusion theory [1-4], the atomistic calculation approach [5-6], the numerical simulation based on finite difference (FD), finite element (FE) [7-14], and boundary element (BE) [15] method and *etc*. Each method owns its advantages compared to other methods. The numerical methods based on FD, FE and BE, however, have been proven to be especially suitable for the strain/stress simulation in QD system, since it is possible to model the complex geometries of QD self-assembled under various growth condition in the numerical methods. Within the numerical methods, the FE method (FEM) has been most widely employed because of the prevalence of the commercial FEM soft packages, such as ANSYS, ABAQUS, and etc.

In this study, we used the commercial FEM code ABAQUS to calculate the 3-dimensional strain fields in and around the QD. Under microscopic observation, typical QDs have pyramidal shapes with a square base of 20 nm along (100)/(010) and a height of 7 nm along (001). The number of QDs per unit area is approximately $5 - 6 \times 10^{10}$ cm^{-2}, deducing an averaged space for each QD to be 50×50 nm^2. The indium composition is assumed to be uniform inside the QD and the QD shape is (110) faceted pyramid for the ideal case. Elastic small deformation theory was adopted in the FEM calculation. Values of the

elastic constants used in the calculations for GaAs and InGaAs are listed in Table 4.1 [16]. For the nanoprobe, Young's modulus and Poisson's ratio of SiO_2 are taken to be $E = 73.1$ GPa and $\upsilon = 0.17$, respectively [17].

TABLE 4.1 Material parameters used in the strain calculation. The values of $In_{0.52}Ga_{0.48}As$ are linearly interpolated from those of GaAs and InAs.

	GaAs	InAs	$In_{0.52}Ga_{0.48}As$
Lattice constant(Å)	5.6533	6.0583	5.8639
c_{11} (GPa)	122.10	83.29	101.92
c_{12} (GPa)	56.60	45.26	50.70
c_{44} (GPa)	60.00	39.59	49.39

4.1.1 Lattice-mismatched strains

In the calculation, the lattice-mismatched strain and the indentation-induced strain were computed independently. The lattice mismatch between $In_{0.52}Ga_{0.48}As$ and GaAs is expressed as

$$\varepsilon = \frac{a_{In_{0.52}Ga_{0.48}As} - a_{GaAs}}{a_{GaAs}} = 0.0373, \tag{4.1}$$

where $a_{In_{0.52}Ga_{0.48}As}$ and a_{GaAs} are the lattice constants of $In_{0.52}Ga_{0.48}As$ and GaAs, respectively. According to Mura's theory [18-20], the eigenstrains for InGaAs and GaAs due to the lattice mismatch can be calculated by the following equations

$$\begin{aligned} \varepsilon_{ij}^{*} = \delta_{ij}\varepsilon = \begin{cases} \varepsilon & i = j \\ 0 & i \neq j \end{cases} \quad &\text{(InGaAs)}, \\ \varepsilon_{ij}^{*} = 0 \quad &\text{(GaAs)}, \end{aligned} \tag{4.2}$$

where i and j take the value x, y, or z. Meanwhile, to represent the effect of the lattice mismatch between InGaAs and GaAs, we applied the lattice mismatch ε as the coefficient of thermal expansion in the QD and raised the temperature by 1 K in the thermoelastic simulation. The total strain e_{ij} is regarded as the sum of the eigenstrain ε_{ij}^{*}

and the elastic strain ε_{ij} :

$$e_{ij} = \varepsilon_{ij}^{*} + \varepsilon_{ij}, \tag{4.3}$$

where the elastic strain ε_{ij} is related to stress by Hooke's law.

For convenience of superposition with the indentation-induced strain in the following step, half QD or whole QD was modeled to calculate the lattice-mismatched strain. The geometry of half QD for FEM modeling is illustrated in Fig. 4.1. The origin was set at the top surface and the *xoz*-plane was taken as the symmetry plane. A substrate with thickness 150 nm, length 50 nm, and width 25 nm was used in the calculation, and the QD layer was embedded at the depth of 50 nm. As for the boundary conditions, a stress-free condition was applied at the top surface, while the bottom of the substrate was forced to remain flat, because the thickness of GaAs is much larger than the size of the QD. The symmetric boundary was set on the symmetry plane (y=0), and the periodic boundary conditions were set to the other three planes (x=±25, y=25).

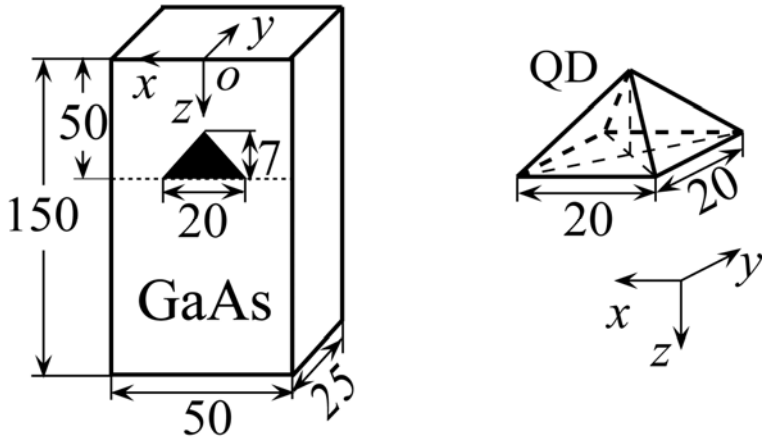

FIG. 4.1 Geometry for finite element modeling of lattice-mismatched strain calculation (half model). The solid pyramid represents one single QD. The insert illustrates the pyramidal shape of QD and its orientation relative to the *xyz* coordinate. All lengths are taken in the unit of nanometer, but not to scale in the illustrations.

4.1.2 Indentation-induced strains

For simulation of the indentation-induced strain, the submodel technique was introduced

because of the large difference between the dimensions of the QD and the nanoprobe size. Additionally, half of the global model is created due to the symmetry of the flat cylindrical nanoprobe/dome-shaped probe.

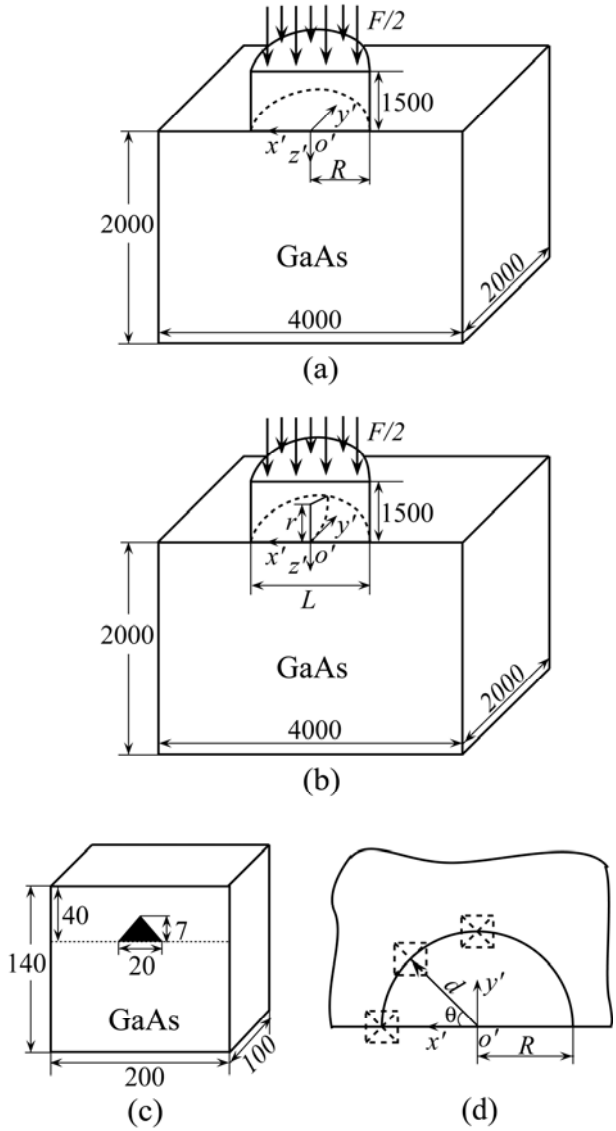

FIG. 4.2 Geometry for finite element modeling of indentation-induced strain calculation, consisting of global model (a)/(b) in the case of flat cylindrical probe/dome-shaped probe, and submodel (c). (d) illustrates the QDs array in the matrix with respect to the flat cylindrical nanoprobe from the top view of (a). One single QD is represented as a solid pyramid in (c), and as a dashed square with a cross in (d). All lengths are taken in the unit of nanometer, but not to scale in the illustrations. According to the experiments, two cases with different probe shapes, flat cylindrical probe with a radius of R=600 nm or dome-shaped probe with L=890 nm and r=640 nm, were examined in the simulation.

In the global model (Fig. 4.2 (a)/(b)), a homogeneous GaAs matrix with dimensions of $4\ \mu\text{m} \times 2\ \mu\text{m} \times 2\ \mu\text{m}$, indented by the nanoprobe with a flat circular apex or dome-shaped apex, was used. In Fig. 4.2 (a), half flat cylindrical nanoprobe with a radius of *R*=600 nm is illustrated. In the case of dome-shaped probe, half probe model corresponding to that (*L*=890 nm, *r*=640 nm, Fig. 2.4(d)) used in the experiment was created in Fig. 4.2 (b). The relation between the tip dome-shape and $x'y'z'$ coordinate is shown in Fig. 3.9. The origin of the $x'y'z'$ coordinate is set at the top surface of the matrix, as shown in Fig. 4.2 (a)/(b). The x', y', z' directions are parallel to the x, y, z directions in Fig. 4.1, respectively, and lie along the principal axis of the crystal. The bottom plane of the matrix was fixed along the z' direction, the $x'o'z'$ plane was applied to the symmetric boundary condition, and the other four planes were set to be stress-free. A uniform pressure was loaded on the top surface of the probe as the indentation force. The indentation effect of the probe's flat/domed apex on the top surface of the matrix was calculated using a small sliding contact without any friction in the global model. The displacement fields obtained in the global model were used to drive the boundary nodes of the submodel (half submodel in Fig. 4.2(c)). The submodel was created for a depth of 10 nm to 150 nm in the global model. The dimensions along the x' and y' directions were 200 nm and 100 nm for half submodel or 200 nm and 200 nm for whole submodel. By placing this submodel at any position in the global model (half submodel at $y'=0$ or whole submodel at $y'\neq 0$), the indentation-induced strains in and around the QD were calculated with dependence on the QD location. In the case of using the flat cylindrical nanoprobe, the location of one single QD (at the depth of $z'=50$ nm) can be represented by *d* (the distance from the QD center to the probe center) and θ (the angle of the QD center relative to the *x'* axis), as illustrated in Fig. 4.2 (d). The largest difference of the strain components in the principle axis of crystal is created by the QDs located at $\theta=45^\circ$ relative to those at $\theta=0^\circ$.

4.1.3 Superposed strains

After the lattice-mismatched and indentation-induced strains were calculated independently, the final strain fields in and around the QDs were derived by superposing these two. As mentioned in Sec. 1.2.3, the hydrostatic strain (ε_h), biaxial strain (ε_s), and shear strain components (ε_{xy}, ε_{yz}, and ε_{xz}) are important to evaluate the strain effect on the energy

bands. The hydrostatic strain is defined as $\varepsilon_{\mathrm{h}} = \varepsilon_{xx} + \varepsilon_{yy} + \varepsilon_{zz}$ representing the relative volume change of the unit cell, and the biaxial strain is $\varepsilon_{\mathrm{s}} = \varepsilon_{yy} - \left(\varepsilon_{zz} + \varepsilon_{xx}\right)/2$ when the x, z axes are taken as the biaxial strain axes.

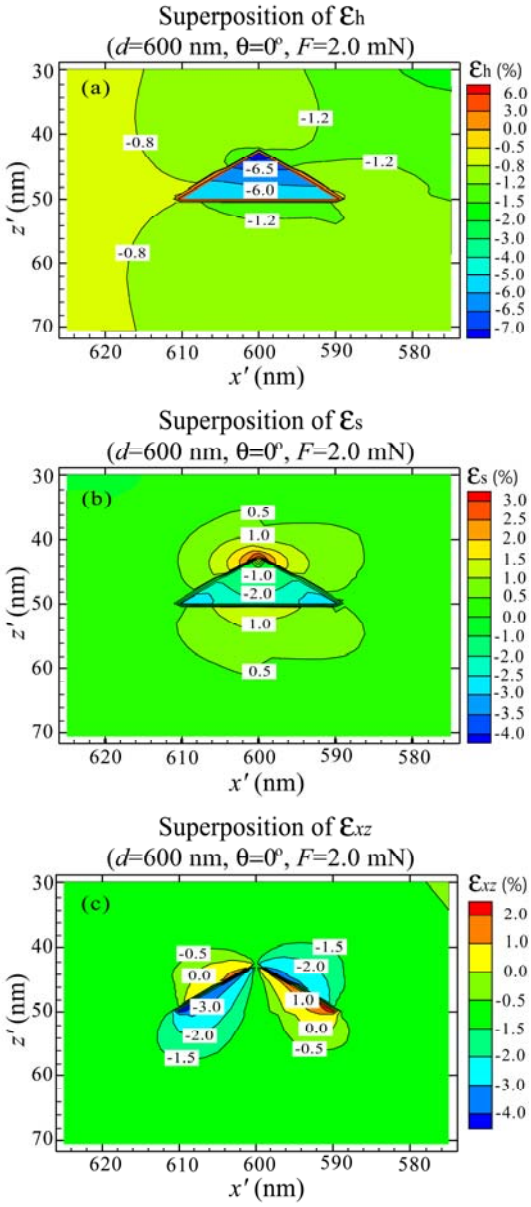

FIG. 4.3 Distribution of superposed strains in the $x'-z'$ plane at the QD location of *d*=600 nm, θ=0° under an indentation force of 2.0 mN (flat cylindrical probe with *R*=600 nm): (a) hydrostatic strain ε_{h} ($\varepsilon_{\mathrm{h}} = \varepsilon_{xx} + \varepsilon_{yy} + \varepsilon_{zz}$), (b) biaxial strain ε_{s} ($\varepsilon_{\mathrm{s}} = \varepsilon_{yy} - \left(\varepsilon_{zz} + \varepsilon_{xx}\right)/2$), and (c) shear strain component ε_{xz} (strain expressed in %).

Figure 4.3 shows the distributions of the superposed hydrostatic strain ε_{h}, biaxial strain ε_{s}, and shear strain component ε_{xz} in the *x'o'z'* plane at the QD location of *d*=600 nm, θ=0° under the indentation force of 2.0 mN with the 600-nm radius flat cylindrical probe. The other two shear strain components ε_{xy} and ε_{yz} are zero in this plane. High hydrostatic, biaxial, and shear strains are induced under the nanoprobe edge by the combined effect of lattice mismatch and indentation (Fig. 4.3). The hydrostatic strain ε_{h} is compressive within the QD and in the surrounding matrix. The interior of the QD exhibits a nearly homogenous hydrostatic strain (−6.5%), while the surrounding matrix experiences a relatively small hydrostatic strain (−1.2%). The biaxial strain is negative in the QD and positive around the QD.

To obtain the dependence of averaged strain in a QD on the location relative to the probe center, we averaged the spatially distributed strain in the QD based on the volume according to

$$\bar{\varepsilon}_{ij} = \frac{1}{V_0}\int_{V_0} \varepsilon_{ij}(x,y,z)\mathrm{d}V\,, \tag{4.4}$$

where V_0 is the total volume of a single QD, $\varepsilon_{ij}(x,y,z)$ is the strain component calculated at the position of (x,y,z), and i and j take values x, y, or z. The lattice-mismatched strains are independent of the QD location, and the volume-averaged values of a single QD are −4.8% in $\bar{\varepsilon}_{\mathrm{h}}^{\mathrm{L}}$, −2.2% in $\bar{\varepsilon}_{\mathrm{s}}^{\mathrm{L}}$, and almost zero in $\bar{\varepsilon}_{xz}^{\mathrm{L}}$. The indentation-induced strains, indented by the flat cylindrical nanoprobe, were calculated for the QDs, both at $\theta = 0^{\circ}$ and $\theta = 45^{\circ}$, to check the influence of the angle θ on strain, as mentioned previously (Fig. 4.2 (d)).

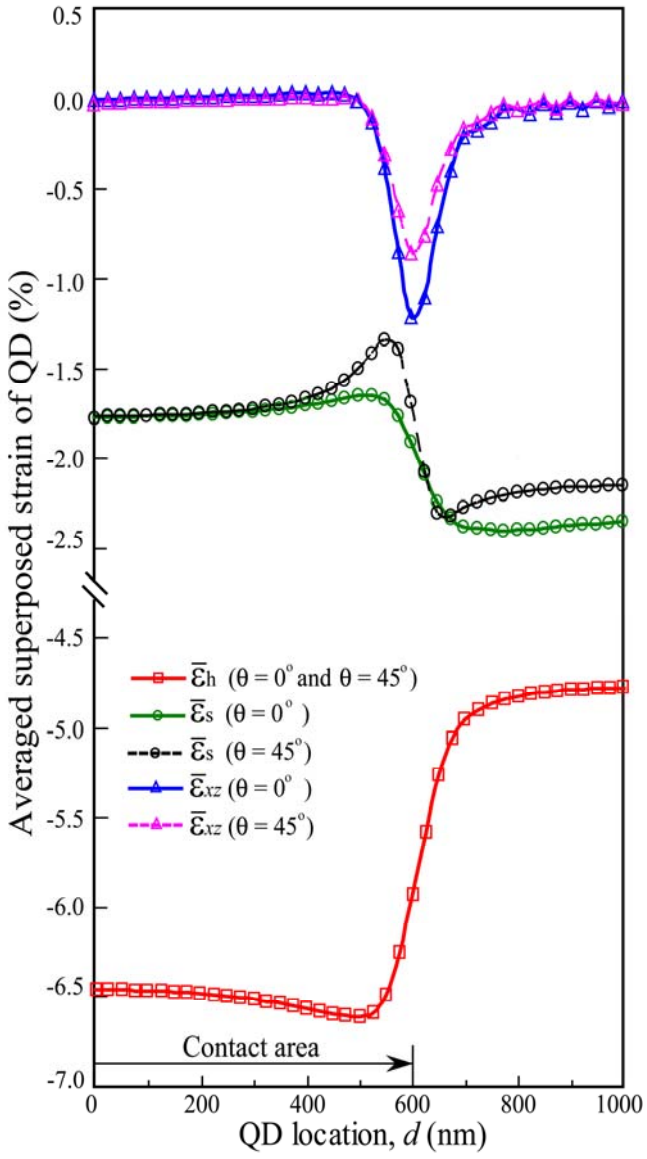

FIG. 4.4 Dependence of superposed strain $\bar{\varepsilon}_h$, $\bar{\varepsilon}_s$ and $\bar{\varepsilon}_{xz}$ of single QD on QD location d at $\theta = 0^\circ$ and $\theta = 45^\circ$ based on the volume averaged values (in flat cylindrical probe case). The distribution of $\bar{\varepsilon}_h$ is independent of θ. The indentation force is 2.0 mN, and the nanoprobe radius is 600 nm.

Figure 4.4 shows the dependence of the superposed strain components $\bar{\varepsilon}_h$, $\bar{\varepsilon}_s$, and $\bar{\varepsilon}_{xz}$ of a single QD on QD location d at $\theta = 0^\circ$ and $\theta = 45^\circ$ based on the volume averaging (in the flat cylindrical probe case). From Fig. 4.4, it is clear that fields of hydrostatic, biaxial, and shear strains are generated with a rapid decay outside the nanoprobe edge ($R = 600$ nm). Under the center of nanoprobe (within the area with a radial distance of $d / R < 0.83$), almost

homogenous biaxial strain field ($\varepsilon_{xx} = \varepsilon_{yy} \neq \varepsilon_{zz}$, $\varepsilon_{xy} = \varepsilon_{yz} = \varepsilon_{xz} = 0$) was created, since the shear strain is mainly induced by the indentation. Under the nanoprobe edge ($0.83 \leq d/R \leq 1.17$), both the hydrostatic and biaxial strains decay dramatically to the lattice-mismatched values due to the loss of the constraint effect. The shear strain $\bar{\varepsilon}_{xz}$, however, is first induced with a negative value and then increases dramatically to zero because of the sudden change of pressure on the contact surface from a finite value to zero at the nanoprobe edge. Similar strain distributions have also been reported in Ref. 21. The factor θ affects the distribution of $\bar{\varepsilon}_{\mathrm{s}}$ and $\bar{\varepsilon}_{xz}$ but has no influence on that of $\bar{\varepsilon}_{\mathrm{h}}$ (Fig. 4.4). The maximum value of $\bar{\varepsilon}_{\mathrm{s}}$ increased from −1.7% to −1.4% as θ increased from 0° to 45°. For $\bar{\varepsilon}_{xz}$, the minimum value was −1.2% for the QD located at $\theta = 0^\circ$, while it increased to −0.9% for $\theta = 45^\circ$. The shapes of the distributions of $\bar{\varepsilon}_{\mathrm{s}}$ and $\bar{\varepsilon}_{xz}$ remained the same.

In the case of using the dome-shaped probe, the superposed strain components of a single QD are shown in Fig. 4.5 with dependences on the *y'* distance from the probe *x'* axis at different *x'* coordinate. The indentation force was 1.14 mN. Under the indentation of the dome-shaped probe, high localized strains were generated beneath the contact area of a rectangular. The length of this contact rectangular along *x*' axis was equal to the bottom length of probe (890 nm), while the width along *y*' axis varied with the applied force. A contact width of approximately 300 nm under the force of 1.14 mN was deduced from the zero stress region (on sample surface) in the FEM simulation, agreeing well with 297 nm estimated from Hertzian contact theory [22] (without friction). Since the contact width, i.e. indentation effect in *y*' direction, increased continuously with force, the superposed/indentation-induced hydrostatic and biaxial strains achieved their minimum and maximum values, respectively, at *y*'=0 and decayed dramatically outside, as shown in Fig. 4.5. This different strain distribution, especially of hydrostatic strain which is predominant in the blueshift of PL of QDs, compared to that in the case of flat cylindrical probe (Fig. 4.4) resulted in the different behavior of the PL emissions from QDs under the nanoprobe indentation, which will be discussed in details in Chapter 5. The shear strain component, $\bar{\varepsilon}_{yz}$, was created with the minimum value under the contact edge, as shown in Fig. 4.5, similar to that in flat cylindrical probe case (Fig. 4.4). The strain distributions (hydrostatic, biaxial and shear strains) in Fig. 4.5 remained almost the same for the distance $0 \leq |x'|/(L/2) \leq 0.84$, but decreased in the magnitude with increasing

$|x'|/(L/2)$ from 0.84, because of the loss of contact constraint in *x*' direction, as shown of hydrostatic strain in Fig. 4.5.

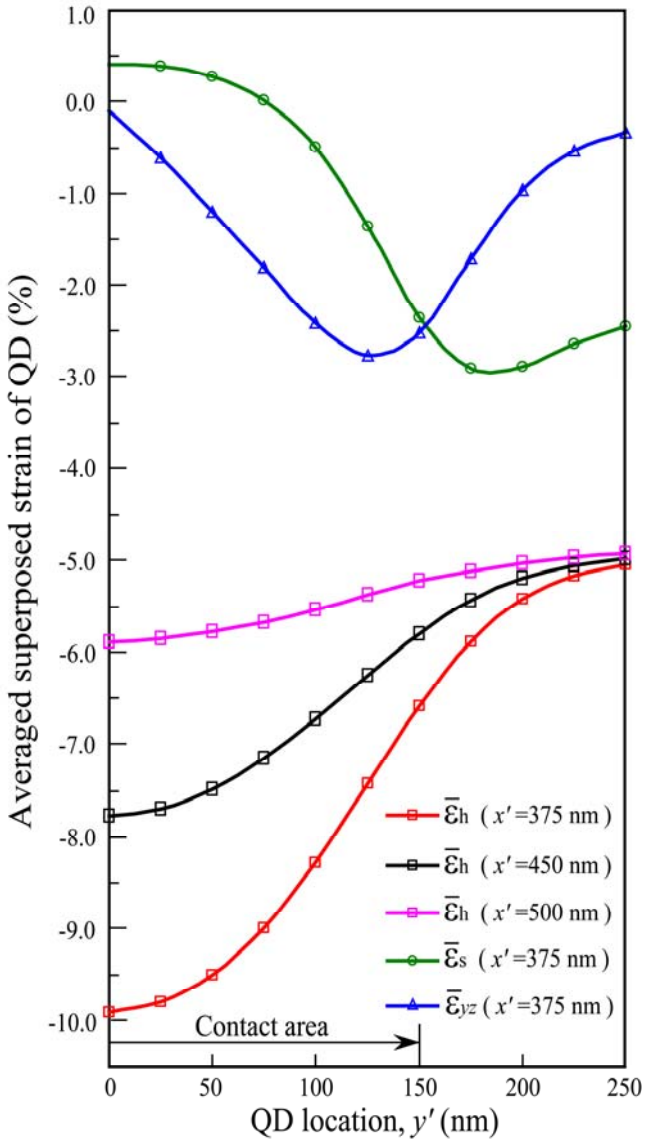

FIG. 4.5 Dependence of superposed strains $\bar{\varepsilon}_h$, $\bar{\varepsilon}_s$ and $\bar{\varepsilon}_{yz}$ of single QD on QD location y' at different *x'* coordinate based on the volume averaged values (in dome-shaped probe case). The indentation force is 1.14 mN.

4.2 Calculation of strain-induced energy shifts

Based on the strain fields obtained in Sec. 4.1, the strain-induced modifications of the

electronic band structures were then calculated according to the deformation potential theory for the bulk material [23], as mentioned in Sec. 1.2.3. In this theory, the elastic strain filed is coupled to the quantum mechanical behavior of the charged carriers in semiconductors through the deformation potentials of the materials. All values referring to the deformation potentials and band structures of GaAs and $In_{0.52}Ga_{0.48}As$ are listed in Table 4.2 [16, 24-29].

TABLE 4.2 Material parameters used in the calculation. The values of $In_{0.52}Ga_{0.48}As$ are linearly interpolated from those of GaAs and InAs considering the bowing parameters. All values are taken from Ref. 16 except several items, VBO and Ξ_u^X from Ref. 24, Ξ_d^X from Ref. 25, L band deformation potentials of GaAs from Ref. 26 while those of InAs from Ref. 27. Except the X and L band gap, all values of $In_{0.52}Ga_{0.48}As$ are calculated according to the recommended bowing parameters in Ref. 16.

	GaAs	InAs	$In_{0.52}Ga_{0.48}As$	Bowing Parameter
E_g^Γ (eV)	1.5188	0.4167	0.8267	0.477
E_g^X (eV)	1.9808	1.4327[a] 2.0000[b]	1.6758---1.3464 1.9708---1.6413	0.080---1.400
E_g^L (eV)	1.8147	1.1327[a] 1.4300[b]	1.3777---1.2804 1.5323---1.4349	0.330---0.720
Δ_0 (eV)	0.341	0.390	0.329	0.150
VBO (eV)	-6.806	-6.543	-6.680	---
a_c (eV)	-7.17	-5.08	-6.735	2.61
a_v (eV)	-1.16	-1.00	-1.077	---
b (eV)	-2.00	-1.80	-1.896	---
d (eV)	-4.80	-3.60	-4.176	---
Ξ_d^X (eV)	-0.87	0.09	-0.371	---
Ξ_u^X (eV)	8.61	4.50	6.473	---
Ξ_d^L (eV)	-8.67	-5.68	-7.119	---
Ξ_u^L (eV)	14.50	11.35	12.862	---

[a]Ref. 16, Extrapolation from the values in Ref. 28 at room temperature to 10 K
[b]Ref. 29

4.2.1 Shifts of energy bands due to strain

The energy shifts of valence band $\Delta E_{\mathrm{v}}^{\Gamma}$ due to strain are calculated as the eigenvalues of the six-band Hamiltonian matrix $H_{\varepsilon}^{\mathrm{v}}$ by the equation

$$\left| H_{\varepsilon}^{\mathrm{v}} - \Delta E_{\mathrm{v}}^{\Gamma} I \right| = 0, \tag{4.5}$$

where I is an identity matrix and "$\left|\ \right|$" denotes the determinant. In Equation (4.5), the six-band Hamiltonian matrix $H_{\varepsilon}^{\mathrm{v}}$ is expressed in Equation (1.28) and (1.29).

For the Γ, X, and L conduction bands of bulk GaAs and InGaAs, the calculations of the energy shift resulting from strain can be obtained by the Herring–Vogt theory [30, 31]. The energy shift of the Γ-band (an s-type state of full cubic symmetry) is proportional to the hydrostatic component of strain according to the equation

$$\Delta E_{\mathrm{c}}^{\Gamma} = a_{\mathrm{c}} \left(\varepsilon_{xx} + \varepsilon_{yy} + \varepsilon_{zz} \right) = a_{\mathrm{c}} \varepsilon_{\mathrm{h}}, \tag{4.6}$$

where a_{c} is the hydrostatic deformation potential of the Γ-conduction band. The energy shifts of the X-band (the point with coordinate (π / a) (100) in reciprocal lattice space, a is the lattice constant, combined states of s- and p-type) due to strain are given as

$$\begin{aligned}
\Delta E_{\mathrm{c}}^{X[100]} &= \left(\Xi_d^X + \frac{1}{3} \Xi_u^X \right) \varepsilon_{\mathrm{h}} + \frac{2}{3} \Xi_u^X \left[\varepsilon_{xx} - \frac{1}{2} \left(\varepsilon_{yy} + \varepsilon_{zz} \right) \right], \\
\Delta E_{\mathrm{c}}^{X[010]} &= \left(\Xi_d^X + \frac{1}{3} \Xi_u^X \right) \varepsilon_{\mathrm{h}} + \frac{2}{3} \Xi_u^X \left[\varepsilon_{yy} - \frac{1}{2} \left(\varepsilon_{zz} + \varepsilon_{xx} \right) \right], \\
\Delta E_{\mathrm{c}}^{X[001]} &= \left(\Xi_d^X + \frac{1}{3} \Xi_u^X \right) \varepsilon_{\mathrm{h}} + \frac{2}{3} \Xi_u^X \left[\varepsilon_{zz} - \frac{1}{2} \left(\varepsilon_{xx} + \varepsilon_{yy} \right) \right],
\end{aligned} \tag{4.7}$$

where Ξ_d^X and Ξ_u^X are the deformation potentials of the X-band. For the L-band ((π / a) (111) in reciprocal lattice space, combined states of s- and p-type), the equations can be written as

$$
\begin{aligned}
\Delta E_{\mathrm{c}}^{L[111]} &= \left(\Xi_d^L + \frac{1}{3}\Xi_u^L\right)\varepsilon_{\mathrm{h}} + \frac{2}{3}\Xi_u^L\left(\varepsilon_{xy}+\varepsilon_{yz}+\varepsilon_{xz}\right),\\
\Delta E_{\mathrm{c}}^{L[\bar{1}11]} &= \left(\Xi_d^L + \frac{1}{3}\Xi_u^L\right)\varepsilon_{\mathrm{h}} + \frac{2}{3}\Xi_u^L\left(-\varepsilon_{xy}+\varepsilon_{yz}-\varepsilon_{xz}\right),\\
\Delta E_{\mathrm{c}}^{L[1\bar{1}1]} &= \left(\Xi_d^L + \frac{1}{3}\Xi_u^L\right)\varepsilon_{\mathrm{h}} + \frac{2}{3}\Xi_u^L\left(-\varepsilon_{xy}-\varepsilon_{yz}+\varepsilon_{xz}\right),\\
\Delta E_{\mathrm{c}}^{L[11\bar{1}]} &= \left(\Xi_d^L + \frac{1}{3}\Xi_u^L\right)\varepsilon_{\mathrm{h}} + \frac{2}{3}\Xi_u^L\left(\varepsilon_{xy}-\varepsilon_{yz}-\varepsilon_{xz}\right),
\end{aligned}
\tag{4.8}
$$

where Ξ_d^L and Ξ_u^L are the deformation potentials of the L-band.

Based on the energy shifts of the valence and Γ-conduction band, the change of the Γ-band gap of bulk GaAs and InGaAs due to strain is obtained as

$$
\Delta E_{\mathrm{g}}^{\Gamma}\left(x,y,z\right) = \Delta E_{\mathrm{c}}^{\Gamma}\left(x,y,z\right) - \Delta E_{\mathrm{v}}^{\Gamma}\left(x,y,z\right). \tag{4.9}
$$

4.2.2 Energy shifts of single QD and surrounding GaAs

The energy shifts of the conduction and valence bands and the change of the band gap were all calculated with the strain fields at the position (x,y,z). The corresponding values of a single QD or those of the GaAs matrix surrounding the QD were then obtained by averaging the distributed $\Delta E_{\mathrm{c}}^{\Gamma}(x,y,z)$, $\Delta E_{\mathrm{c}}^{X}(x,y,z)$, $\Delta E_{\mathrm{c}}^{L}(x,y,z)$, $\Delta E_{\mathrm{v}}^{\Gamma}(x,y,z)$, and $\Delta E_{\mathrm{g}}^{\Gamma}(x,y,z)$ over the volume according to

$$
\Delta\overline{E}_{(\mathrm{c,v,g})}^{(\Gamma,X,L)} = \frac{1}{V_0}\int_{V_0}\Delta E_{(\mathrm{c,v,g})}^{(\Gamma,X,L)}(x,y,z)\mathrm{d}V, \tag{4.10}
$$

where V_0 is the volume of the QD or the matrix surrounding the QD. Since the strain-induced energy shifts in the GaAs matrix are mainly concentrated in a thin layer of 5-nm thickness surrounding the QD, the V_0 of GaAs was taken as the volume of this 5-nm-thickness layer.

Note the deviation of the confinement energies of the electrons and holes in the QD from the bulk energy levels of the strained InGaAs. Since the dimension of the QD is far smaller than the radius of the nanoprobe, the materials in and around the QD exhibit similar energy shift behaviors. As a result, the depth of the potential well for the electrons/holes confined in the conduction/valence bands remains almost constant before and after indentation (within a difference of 5% due to the small difference in the deformation potentials between InGaAs

and GaAs). Therefore, we assumed that the indentation-induced change of the ground state difference between the electrons and holes in the QDs is equal to the change of the band gap $\Delta\overline{E}_{\mathrm{g}}^{\Gamma}$ of bulk InGaAs resulting from the indentation-induced strain. Then, the experimentally observed blueshift of the PL-peak energy emitted by recombination of the ground state electrons and holes in the QDs (Fig. 3.1 and Fig. 3.3 (a)) can be ascribed to the enlargement of the band-gap energy of bulk InGaAs resulting from the indentation-induced strain. Calculations have shown this band-gap enlargement of bulk InGaAs is mainly due to the upward shift of the Γ-conduction band, which depends linearly on the hydrostatic strain (Eq. (4.6)). Therefore, the PL peak energy was observed linearly blueshifting with the indentation force, as shown in Fig. 3.3 (a), in spite of the nonlinear energy shift in the valence band with force resulting from the influence of indentation-induced biaxial and shear strain components. The blueshift rate corresponding to that obtained in the experiment (Fig. 3.3 (a)) was calculated as the change in the band-gap energy of bulk InGaAs induced by the indentation of unit force on the basis of QD volume averaging, $\Delta\overline{E}_{\mathrm{g}}/\Delta F$.

Figure 4.6 shows the simulated relationship between the blueshift rate $\Delta\overline{E}_{\mathrm{g}}/\Delta F$ and distance d of QD from the center of flat cylindrical probe (R=600 nm) at both θ = 0° and 45°. The shape of the relationship curves in Fig. 4.6 is mainly determined by the distribution of hydrostatic strain in Fig. 4.4, because the hydrostatic strain dominates in the blueshift of InGaAs band-gap energy. The range of the blueshift rate derived from the simulation (from 0 to 79.4 meV/mN) covers the experimentally obtained blueshift rate, except for one QD, as shown in Fig. 4.6. The excess of the blueshift rate of this QD is probably caused by the large difference in its shape (height to base width ratio) or the indium composition inside it, compared with most of the QDs, based on which we assumed the shape (a pyramidal shape with a 20 nm base and 7 nm height) and the indium composition (52% of indium composition uniform inside the QD) of the QD in the strain- and energy-shift calculations. The blueshift rates obtained in this study (from both experiment and simulation) give an order of magnitude agreement with 0.024 — 0.073 meV/nm for InAlAs/AlGaAs QDs [12, 32] and 0.5 — 3.5 meV/nm for InAs/GaAs QDs [21] under nanoprobe indentation, in which the indentation force was estimated from the vertical displacement of the probe with approximately 5 μN/nm. Since the hydrostatic strain dominates in the blueshift of PL in our study, the obtained blueshift rate can be approximately expressed in the form of hydrostatic strain with a simulation-derived

value from -88.7 to 0 meV per unit percent of indentation-induced hydrostatic strain. This agrees well with the blueshift rate of bulk GaAs of 10.73 meV/kbar [33] and of InGaAs/GaAs QDs of 8.0 – 8.6 meV/kbar [34] measured under hydrostatic pressure. The obtained relationship in Fig. 4.6 will be used to determine the QD location in the case of using flat cylindrical probe for indentation, as will be discussed in Sec. 5.2.

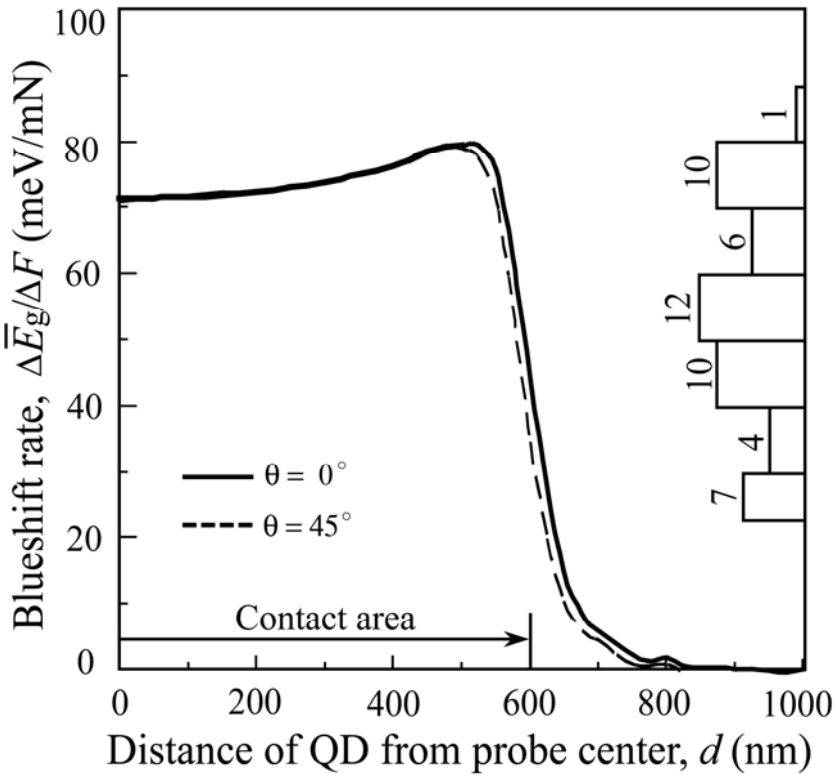

FIG. 4.6 Simulated relationship between the blueshift rate, $\Delta\overline{E}_g/\Delta F$, and the distance *d* of QD from the center of flat cylindrical probe at both $\theta = 0°$ and 45°. The nanoprobe radius is 600 nm. The right-side bars show the number of the observed QDs in each range of the blueshift rate (Fig. 3.4).

4.3 Summary

By employing the finite element method, we succeeded in simulating and calculating the 3-dimensional strain fields (composed of lattice-mismatched and indentation-induced strains) in and around a single QD. Calculations have shown that highly localized strain fields were generated under the indentation of nanoprobe, either with flat cylindrical probe or dome-shaped probe. The change of the tip shape of used probe modified the generated

localized strain fields, leading to the different behavior of PL emissions observed in the indentation experiment. Based on the obtained strain fields, the influence of strains on the band structures of QDs were evaluated according to the deformation potential theory. The calculation-derived blueshift rate, using the flat cylindrical nanoprobe, agreed well with the experimentally measured values in the stationary indentation. The simulated relationship between blueshift rate and QD location will be used to estimate the QDs in the case of flat cylindrical probe.

References

[1] J. D. Eshelby, "*The determination of the elastic field of an ellipsoidal inclusion, and related problems*", Proceedings of the Royal Society of London, Series A Mathematical and Physical Sciences 241, 376-396 (1957).

[2] J. D. Eshelby, "*The elastic field outside an ellipsoidal inclusion*", Proceedings of the Royal Society of London, Series A Mathematical and Physical Sciences 252, 561-569 (1959).

[3] G. Springholz *et al.*, "*Vertical and lateral ordering in self-organized quantum dot superlattices*", Physica E: Low-dimensional Systems and Nanostructures 9(1), 149-163 (2001).

[4] F. Glas, "*Elastic relaxation of truncated pyramidal quantum dots and quantum wires in a half space: An analytical calculation*", Journal of Applied Physics 90(7), 3232-3241 (2001).

[5] M. A. Cusack, P. R. Briddon, and M. Jaros, "*Electronic structure of InAs/GaAs self-assembled quantum dots*", Physical Review B 54(4), R2300-R2303 (1996).

[6] Y. Kikuchi, H. Sugii, and K. Shintani, "*Strain profiles in pyramidal quantum dots by means of atomistic simulation*", Journal of Applied Physics 89(1), 1191-1196 (2001).

[7] S. Christiansen *et al.*, "*Strained state of Ge(Si) Islands on Si: Finite element calculations and comparison to convergent beam electron-diffraction measurement*", Applied Physics Letters 64(26), 3617-3619 (1994).

[8] T. Benabbas *et al*., "*Stress relaxation in highly strained InAs/GaAs structures as studied by finite element analysis and transmission electron microscopy*", Journal of Applied Physics 80(5), 2763-2767 (1996).

[9] A. Carlsson *et al*., "*Strain state in semiconductor quantum dots on surfaces: a comparison of electron microscopy and finite element calculations*", Surface science 406, 48-56 (1998).

[10] T. Benabbas, Y. Androussi, and A. Lefebvre, "*A finite-element study of strain fields in vertically aligned InAs Islands in GaAs*", Journal of Applied Physics 86(4), 1945-1950 (1999).

[11] G. Muralidharan, "*Strain in InAs quantum dots embedded in GaAs: A finite element study*", Japanese Journal of Applied Physics, Part 2 39(7A), L658-L660 (2000).

[12] H. T. Johnson, and R. Bose, "*Nanoindentation effect on the optical properties of self-assembled quantum dots*", Journal of Mechanics and Physics of Solids 51, 2085-2104 (2003).

[13] H. T. Johnson *et al*., "*Effects of externally applied stress on the properties of quantum dot*

nanostructures", International Journal for Multiscale Computational Engineering 1(1), 33-41 (2003).

[14] Y.-H. Liang, Y. Arai, K. Ozasa, M. Ohashi, and E. Tsuchida, "*Simultaneous measurement of nanoprobe indentation force and photoluminescence of InGaAs/GaAs quantum dots and its simulation*", Physica E 36, 1-11 (2007).

[15] B. Yang, and E. Pan, "*Elastic analysis of an inhomogeneous quantum dot in multilayered semiconductor using a boundary element method*", Journal of Applied Physics 92(6), 3084-3088 (2002).

[16] I. Vurgaftman, J. R. Meyer, and L. R. Ram-Mohan, "*Band parameters for Ⅲ－Ⅴ compound semiconductors and their alloys*", Journal of Applied Physics 89(11), 5815 (2001).

[17] E. H. Bogardus, "*Third-Order Elastic Constants of Ge, MgO, and Fused SiO_2*", Journal of Applied Physics 36(8), 2504 (1965).

[18] T. Mura, "*Micromechanics of Defects in Solids*", Martinus Nijhoff Publishers, second revised version, Boston (1987).

[19] Valeria-Gabriela Stoleru, Debdas Pal, and Elias Towe, "*Self-assembled (In,Ga)As/GaAs quantum-dot nanostructures: strain distribution and electronic structure*", Physica E 15, 131-152 (2002).

[20] O. Stier, M. Grundmann, and D. Bimberg, "*Electronic and optical properties of strained quantum dots modeled by 8-band k·p theory*", Physical Review B 59, 5688 (1999).

[21] A. M. Mintairov, K. Sun, J. L. Merz, C. Li, A. S. Vlasov, D. A. Vinokurov, O.V. Kovalenkov, V. Tokranov, and S. Oktyabrsky, "*Nanoindentation and near-field spectroscopy of single semiconductor quantum dots*", Physical Review B 69, 155306 (2004).

[22] H. Hertz, Journal of Reine Angew. Math. 92, 156 (1182).

[23] G. L Bir, and G. E. Pikus, "*Symmetry and Strain-induced Effects in Semiconductors*", Wiley, New York, 1974.

[24] Chris G. Van de Walle, "*Band lineups and deformation potentials in the model-solid theory*", Physical Review B 39(3), 1871 (1989).

[25] M. C. Munoz, and G. Armelles, "*X-point deformation potentials of Ⅲ－Ⅴ semiconductors in a tight-binding approach*", Physical Review B 48(4), 2839 (1993).

[26] D. N. Mirlin, V. F. Sapega, I. Ya. Karlik, and R. Katilius, "*Hot photoluminescence spectroscopy investigations of L-valley splitting and intervalley scattering in uniaxially stressed gallium arsenide*", Solid State Communications 61(12), 799-802 (1987).

[27] R. Santoprete, Belita Koiller, R. B. Capaz, P. Kratzer, Q. K. K. Liu, and M. Scheffler, "*Tight-binding study of the influence of the strain on the electronic properties of InAs/GaAs quantum dots*", Physical Review B 68, 235311 (2003).

[28] Sadao Adachi, "*Band gaps and refractive indices of AlGaAsSb, GaInAsSb, and InPAsSb: Key properties for a variety of the 2-4-μm optoelectronic device applications*", Journal of Applied Physics 61(10), 4869 (1987).

[29] Sandip Tiwari, and David J. Frank, "*Empirical fit to band discontinuities and barrier heights in Ⅲ-Ⅴ alloy*", Applied Physics Letters 60(5), 630 (1992).

[30] Conyers Herring, and Erich Vogt, "*Transport and Deformation-Potential Theory for Many-Valley Semiconductors with Anisotropic Scattering*", Physical Review 101(3), 944 (1956).

[31] I. Balslev, "*Influence of Uniaxial Stress on the Indirect Absorption Edge in Silicon and Germanium*", Physical Review 143(2), 636-647 (1966).

[32] H. D. Robinson, M. G. Muller, B. B. Goldberg, and J. L. Merz, "*Local optical spectroscopy of self-assembled quantum dots using a near-field optical fiber probe to induce a localized strain field*", Applied Physics Letters 72(17), 2081 (1998).

[33] D. J. Wolford, and J. A. Bradley, "*Pressure dependence of shallow bound states in gallium arsenide*", Solid State Communications 53(12), 1069-1076 (1985).

[34] S. G. Lyapin, I. E. Itskevich, I. A. Trojan, P. C. Klipstein, A. Polimeni, L. Eaves, P. C. Main, and M. Henini, "*Pressure-Induced Γ-X Crossover in Self-Assembled In(Ga)As/GaAs Quantum Dots*", Physica Status Solid (b) 211, 79 (1999).

Chapter 5
Estimation of the location of embedded InGaAs QDs

5.1 Introduction

Determining the location of quantum dots (QDs), which are usually embedded in the nanostructure, is of great importance in developing single QD devices with new functionalities such as single photon emission and qubit operations [1-2]. Nanoprobe photoluminescence (PL) measurement[3-10], in which a nanoprobe made from optical fiber is used to induce pressure effects onto the QDs as well as to collect the emission PL, makes it possible to distinguish QD from QD embedded in the structure, because PL emission from each single QD is observable due to the generation of localized strains near the aperture of the probe. Most nanoprobe work focused on the dependence of the PL emission spectra of single QD on the exerted pressure [5-7] as well as the effect of different nanoprobe tip shapes and sizes [8]. Little research examines the location of individual QDs, mainly due to lack of information on the nanoprobe-induced strain fields [5] or the failure in the quantitative measurement of the applied force [5-6, 8]. In our previous reports [9, 10], the location of the embedded InGaAs/GaAs QDs was determined by combining PL measurement during elastic indentation with a horizontal scan (scanning indentation is described in Chapter 2) using a flat cylindrical nanoprobe and quantitative analysis of the indentation-induced strains and energy shifts. The observed QDs were estimated to be located around the probe edge. We also proven that photoexcited holes accumulated at the probe edge because of indentation, leading to the enhancement and observation of the PL emitted only from the QDs at the probe edge. In Ref. 10, determination of the QDs' location required more than 840 strain- and energy-shift calculations of a single QD (when using a flat cylindrical nanoprobe with a radius of 600 nm), by placing the single QD at different positions on the QD layer plane with a 25 nm spatial resolution (Fig. 5.2 (a)).

In this study, we prose another method for estimating the distance of QDs from the center of a flat cylindrical nanoprobe using elastic indentation. This method is much simpler

than the scanning indentation method reported in Ref. 10 (drastically reduced simulation requirements for the same spatial resolution of the QDs' location) but equally reliable (the QDs were also estimated to be located around the probe edge with distance from 550 to 650 nm from the probe center). The PL peak energy of a single QD is observed to blueshift linearly with the applied force under the indentation of a flat cylindrical nanoprobe. The shift of the peak energy per unit force, i.e., the blueshift rate, of each single QD varies from QD to QD; therefore, it might relate to its distance from the probe center. Corresponding to the experimental conditions, the energy shift of the QD ground state induced by nanoprobe indentation is calculated on the basis of quantitative analysis of the indentation-induced strain fields. As a result, a simulated relationship between the blueshift rate and distance of the QD from the probe center is obtained. Using this relationship, we successfully estimate the distance of the QD from the probe center from the experimentally obtained blueshift rate. The estimated relative distance of the QD is compared to that from using the method reported in Ref. 10.

In addition, we also used a dome-shaped nanoprobe to induce elastic indentation of scan onto the QDs sample (*y*-scan in Sec. 3.3). With the PL results of scanning indentation, the locations of some of observed QDs in the *y* coordinate (scan direction) were directly obtained from the PL results, at where the PL energy of single QD reached a maximum value. This direct determination of QDs location from indentation experiments can not be achieved by the usage of a flat cylindrical probe, because different indentation-induced strain fields were generated by the modification of the probe tip shape.

5.2 Estimation of the QDs location using a flat cylindrical probe

5.2.1 Estimation method

As described in Fig. 4.2 (d), the location of single QD relative to the center of a flat cylindrical nanoprobe was presented by the distance d and angle θ. In this section, we proposed a method to estimate the distance d from the blueshift rate obtained with stationary indentation with a simulated relationship between the blueshift rate and distance d.

The blueshift rate of QDs was obtained experimentally from the PL spectra measured with stationary indentation at different indentation forces, as discussed in Fig. 3.3 (a). The simulated relationship between the blueshift rate and the distance d was derived from the numerical calculation, as shown in Fig. 4.6. In the location estimation, the curves in Fig. 4.6

with the distance *d* from 550 to 650 nm were used to determine *d* of a single QD from the experimentally obtained blueshift rate (from 22.7 to 87.8 meV/mN except for the excess in Fig. 4.6), because only the PL emission from the QDs around the probe edge can be enhanced and observed under nanoprobe indentation because of the hole accumulation at the probe edge, as reported in Refs. 9 and 10. Based on the estimation method described above, *d* of each QD was determined over a range of θ from 0° to 45°.

5.2.2 Estimation results

In order to quantitatively evaluate the reliability and accuracy of the estimation method introduced above, the distances *d* of QDs estimated from the blueshift rate were compared to those derived from scanning indentation. The comparison was performed as follows:

Firstly, the QDs corresponding to those observed with stationary indentation were found with scanning indentation by using two PL spectra, as described in Fig. 3.7. The two spectra in Fig. 3.7, as discussed, were measured under the same indentation force and at the same indentation position but from stationary and scanning indentation, respectively. These two spectra enabled us to exactly correspond the QDs observed with stationary and scanning indentation through the correspondence of the PL peaks for each QD (QD1, QD2, QD3, and QD4 in Fig .3.7). More corresponding QDs (QD5, QD6, QD7, and QD8) were found by using other groups of spectra observed at other indentation positions (at (35.5, 0) in Fig. 3.5).

Secondly, location of the corresponding QDs found in the first step, for example, QD1, QD2, QD3, and QD4 in Fig. 3.7, were determined individually using scanning indentation, as reported in Ref. 10.

Finally, the distances *d* of the QDs estimated from the blueshift rate were compared to those from the scanning indentation, as plotted in Fig. 5.1. The value of *d* derived from the scanning indentation was assumed to be the exact distance of the QD from the probe center. Both scanning and stationary indentation provide high spatial resolution for the QDs' location in the range of 100 nm (*d* = 550~650 nm), as shown in Fig. 5.1. The relative error between the distance *d* estimated from stationary indentation at $\theta = 0°$ (square)/ $\theta = 45°$ (triangle symbol) and that from scanning indentation (circle) was measured as error-1/error-2, as shown in Fig. 5.1. From the comparison in Fig. 5.1, good agreement was obtained between the distance *d* estimated by stationary and scanning indentations, especially for QD1, QD5, QD7, and QD8. The maximum relative errors measured for QD3 were found to be 6.9% and 4.4% in error-1

and error-2, respectively.

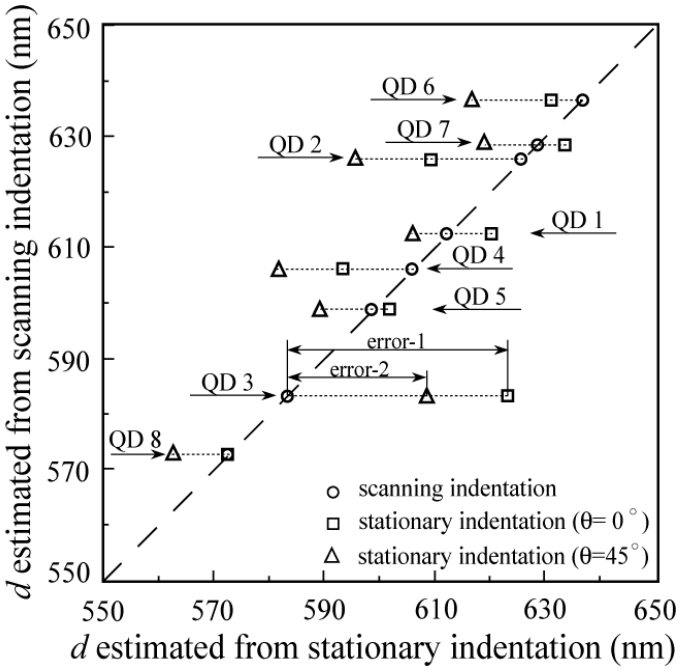

FIG. 5.1 Comparison of the distances *d* of several QDs estimated from the blueshift rate obtained with stationary indentation with those from scanning indentation. The circles represent the results of scanning indentation, while the squares and triangles are the results of stationary indentation at $\theta = 0°$ and $\theta = 45°$, respectively. The dashed line is for convenience in comparing the results on the horizontal scale and the dotted lines are a visual guideline for connecting the estimated results for a single QD.

5.2.3 Advantage of present estimation method

Compared to the scanning indentation method, determination of the QD distances *d* from the blueshift rate (Fig. 4.6) required 70 strain- and energy-shift calculations of a single QD, at most (only about one twelfth of that with scanning indentation) with a nanoprobe of the same radius to obtain the same spatial resolution of the QDs' location, as illustrated in Fig. 5.2 (b). Therefore, estimating *d* using stationary indentation is much simpler than that using scanning indentation.

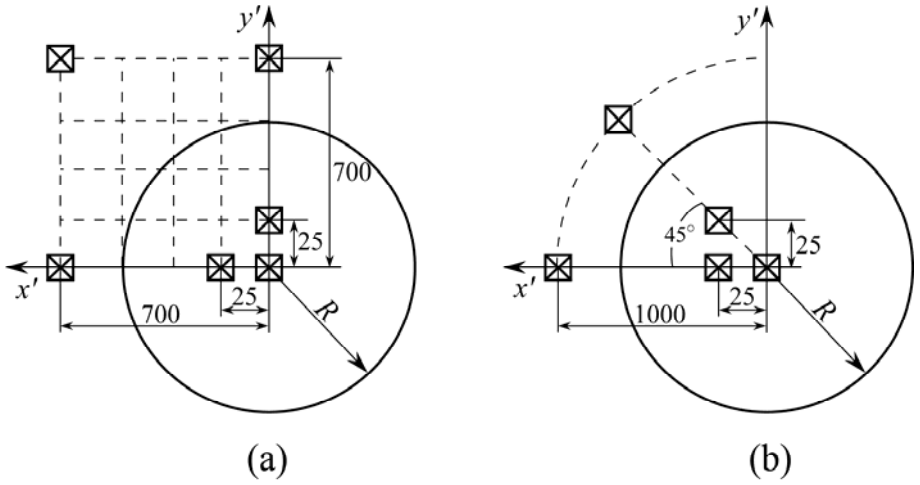

FIG. 5.2 Comparison of the required quantity of times of single QD strain/energy-shift calculations in the location estimation using (a) scanning indentation (840 times at least) and (b) stationary indentation (70 times at most). The radius of the flat cylindrical probe is R=600 nm, and the spatial resolution of QD location is 25 nm. A single QD is represented as the open rectangular with a cross inside.

5.3 Estimation of the QDs location using a dome-shaped probe

5.3.1 Estimation method

As discussed in Fig. 3.10, the PL emissions from some QDs (QD1 to QD11 in Fig. 3.10), observed with the *y*-scan of dome-shaped probe, exhibited symmetric blue- and red-shifts with the movement of probe indentation position. This PL emission behavior was caused by the indentation-induced strain fields of dome-shaped probe, as shown in Fig. 4.5.

The solid curves in Fig. 5.3 show the changes of band-gap energy of QDs ($\Delta\overline{E}_{\mathrm{g}}^{\Gamma}$ of bulk InGaAs), induced by the indentation of 1.14 mN, with dependences on the *y*' distance from the probe *x*' axis at different *x*' coordinates. Under the indentation of the dome-shaped probe, highly localized strains were generated beneath the contact area of a rectangular, as shown in Fig. 4.5. The indented strain field, especially the hydrostatic strain, determined the energy shift of QDs in Fig. 5.3 to have the *y*'-distance dependence similar to that of hydrostatic strain (Fig. 4.5).

In the experiment of *y*-scan, the movement of probe changed the *y*' distance of QDs relative to the probe *x*' axis. When the probe is close enough to one QD, i.e. with a $|y'|$ distance within 150 nm (half contact width along *y'* direction), the PL emission from this QD

will be enhanced due to the strain effect. With further closer to the probe *x*' axis, the emitted PL peak energy will be blueshifted since the hydrostatic strain experienced by the QD increases (high strain, high energy shift), until it reaches the maximum value when the QD is just located under the probe *x*' axis (*y*'=0). Reverse procedure occurs in the followed leaving of probe from QD, observed as symmetric redshift of PL energy. These presumed symmetric blue- and red-shifts of PL energy were observed from some QDs (QD1 to QD11 in Fig. 3.10) in the scan experiment. Therefore, the locations at where the PL energy of these QDs achieved the maximum value provided their locations in the *y* coordinate.

As discussed above, the *y* locations of some observed QDs in the *y*-scan were directly obtained in Fig. 3.10. The *x* locations of those QDs ($|x'|$ distance from the probe *y*' axis) then can be determined by comparing the PL energy shift measured in scan to the simulated value due to indentation, as shown in Fig. 5.3, using the least squares method [10, 11].

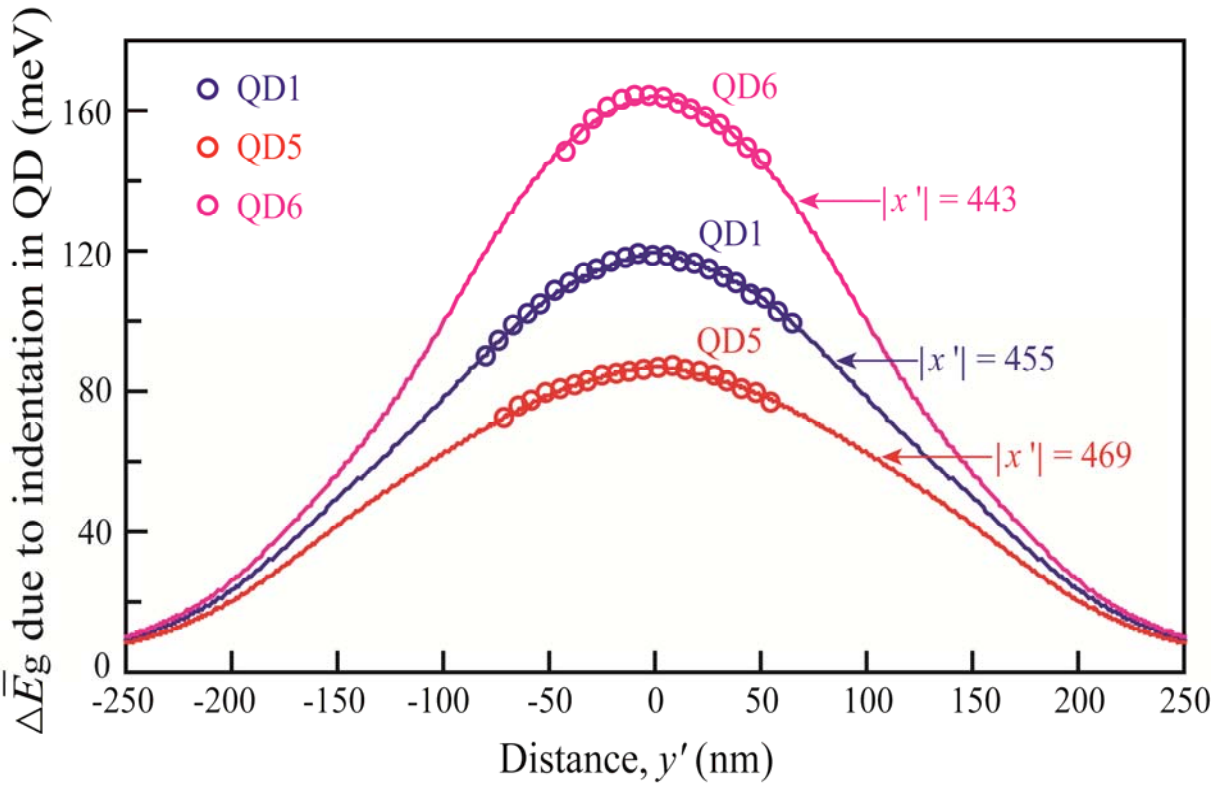

FIG. 5.3 Determination of the QDs location in the *x* coordinate by fitting the experimental PL energy shift (open circles) to the simulation (solid lines). $|x'|$ represents the absolute *x*' distance from the *y*' axis line. The indentation force is 1.14 mN.

5.3.2 Estimation results

Figure 5.4 shows the results of location determination of QD1 to QD11 in Fig. 3.10. All these QDs were located under the contact edge in the probe *x*' direction. This may probably caused by the hole-accumulation under the probe edge, as reported in the flat cylindrical probe case [9]. Since the other part of PL emissions from single QDs in Fig. 3.10, rather than QD1 to QD11, didn't exhibit the symmetric blue- and red-shifts, the examination of these PL emissions as well as the influence of probe tip-shape on the region of observed QDs, will be examined in the future work.

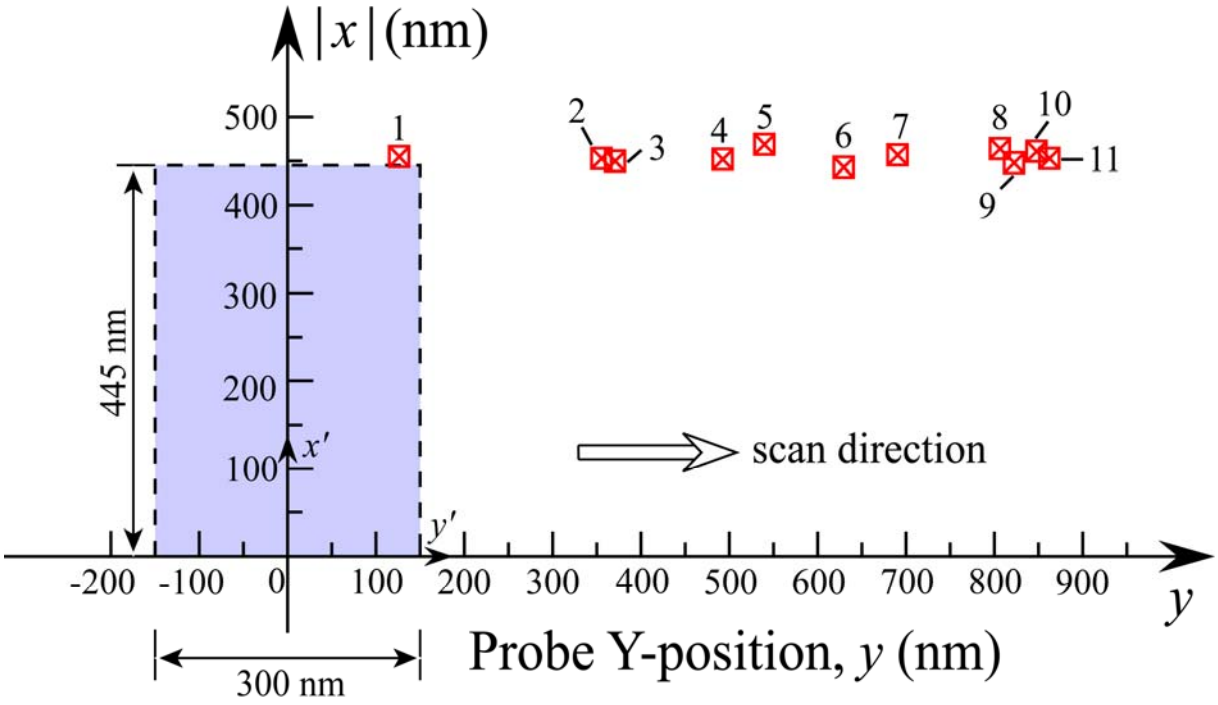

FIG. 5.4 Locations of some of observed QDs (QD1 to QD11) in Fig. 3.10. The open rectangular with a cross inside represents one single QD, while the solid rectangular illustrates the half contact area of the dome-shaped probe under the force of 1.14 mN.

5.3.3 Discussion

The symmetric blue- and red-shift of PL emissions from QDs (QD1 to QD11 in Fig. 3.10) has not been observed in the scanning indentation of the flat cylindrical nanoprobe (Fig. 3.6).

This is because the indentation-induced strain fields by dome-shaped probe and by flat cylindrical probe differ from each other. Under the indentation of a flat cylindrical probe, almost homogeneous biaxial strain fields were generated under the probe centre, within the area with a radial distance from 0 to approximately 550 nm from the probe centre in the case of 600 nm in the probe radius (Fig. 4.4). From 550 to 650 nm (under the probe edge), this biaxial strain decayed rapidly to zero. Consequently, the strain-induced energy shift of QDs exhibited a shoulder at the maximum value level within the probe centre (Fig. 4.6), making it impossible to observe the symmetric blue- and red-shifts of PL emissions from single QD within a scan range of 1.1 μm. Actually, the PL emissions from QDs were observed to be quenched when the flat cylindrical probe was too close to the QD [10] or the indentation force was applied up to a high level [9]. Therefore, the locations of QDs observed in the scan of a flat cylindrical probe can only be determined from the comparison of PL energy shift to simulation, as reported in Ref. 10 and 11.

5.4 Summary

In Sec. 5.2, we proposed a method for estimating the distance of embedded InGaAs/GaAs QDs from the probe center by measuring the blueshift of the PL peak energy induced by stationary indentation of a flat cylindrical nanoprobe. Fine PL peaks from single QDs were enhanced with the indentation force, and the peak energy was observed to blueshift with a linear dependence on the force. The blueshift rate measured in the stationary indentation experiment was used to derive the distance of a single QD from the probe center by analyzing the quantitative relation between these two on the basis of a numerical simulation. All QDs observed with stationary indentation were determined to be located around the probe edge. Furthermore, good agreement was obtained between the derived distance of the QDs from the blueshift rate and that from scanning indentation. Although estimation of d from the blueshift rate obtained from stationary indentation cannot provide the exact position of the QD (θ = 0°~45°), it introduces a much simplified but equally reliable method for evaluating the relative location of the QD from the probe center using nanoprobe indentation.

In Sec. 5.3, by introducing localized strain fields using a domed-apex probe, which is different from that by a flat cylindrical probe, we achieved an advantageous improvement in estimating the location of embedded InGaAs/GaAs QDs with nanoprobe indentation. The

locations of some observed QDs in a *y*-scan were directly obtained from the PL results, at where the PL energy of the QD reached a maximum value. This direct obtainment of QD location from the indentation experiment can not be achieved by using the flat cylindrical nanoprobe.

References

[1] E. Knill, R. Laflamme, and G. J. Milburn, "*A scheme for efficient quantum computation with linear optics*", Nature 409, 46 (2001).

[2] A. Shields, "*Quantum Logic with Light, Glass, and Mirrors*", Science 297, 1821 (2002).

[3] Y. Oshikane, T. Kataoka, M. Okuda, S. Hara, H. Inoue, and M. Nakano, "*Observation of nanostructure by scanning near-field optical microscope with small sphere probe*", Science and Technology of Advanced Materials 8, 181-185 (2007).

[4] P. W. Kolb, and H. D. Drew, "*Investigation of coupling in naturally occurring GaAs quantum dots*", Physica E 40, 594-599 (2008).

[5] H. D. Robinson, M. G. Muller, B. B. Goldberg, and J. L. Merz, "*Local optical spectroscopy of self-assembled quantum dots using a near-field optical fiber probe to induce a localized strain field*", Applied Physics Letters 72(17), 2081 (1998).

[6] H. T. Johnson and R. Bose, "*Nanoindentation effect on the optical properties of self-assembled quantum dots*", Journal of the Mechanics and Physics of Solids 51, 2085-2104 (2003).

[7] Yuan-Hua Liang, Yoshio Arai, Kazunari Ozasa, Masane Ohashi, and Eiichiro Tsuchida, "*Simultaneous measurement of nanoprobe indentation force and photoluminescence of InGaAs/GaAs quantum dots and its simulation*", Physica E 36, 1-11 (2007).

[8] A. M. Mintairov, K. Sun, J. L. Merz, C. Li, A. S. Vlasov, D. A. Vinokurov, O.V. Kovalenkov, V. Tokranov, and S. Oktyabrsky, "*Nanoindentation and near-field spectroscopy of single semiconductor quantum dots*", Physical Review B 69, 155306 (2004).

[9] Kazunari Ozasa, Mizuo Maeda, Masahiko Hara, Masane Ohashi, Yuan-Hua Liang, Hiroki Kakoi, and Yoshio Arai, "*Localized strain effects on photoluminescence of quantum dots induced by nanoprobe indentation*", Physica E 40, 1920-1923 (2008).

[10] Yuan-Hua Liang, Masane Ohashi, Yoshio Arai, and Kazunari Ozasa, "*Location of quantum dots identified by microscopic photoluminescence changes during nanoprobe indentation with a horizontal scan*", Physical Review B 75, 195318 (2007).

[11] Yuan-Hua Liang, "*Nanoprobe Indentation on Quantum Dots with Photoluminescence Measurement : Strain Distribution, Energy Shift, and Location Identification*", Doctoral Thesis of Saitama University (2007).

Chapter 6
Mechanism of PL quenching of InGaAs/GaAs QDs resulting from indentation using a flat cylindrical nanoprobe

6.1 Introduction

In the last few decades, much work has been done to study the influence of strain on the electronic and optical properties of quantum dots (QDs) [1-3]. It has been proven that the optical properties of the QD-related heterostructure can be greatly improved by introducing an external strain field, for example, with diamond anvil cells [4-7], nanoprobe indentations [8-13], or uniaxial loading [14,15]. Photoluminescence (PL) spectroscopy is a powerful technique to gain understanding of the discrete quantum levels in QDs [16,17] and to quantitatively evaluate the dependence of electronic and optical properties of QDs on strain [10,18-20]. The information on quantum energy levels relative to strain is essential to develop QD heterostructures having higher performance in optoelectronic applications [21].

One of the most effective schemes to study the influence of strain on the optical properties of QD is to observe the PL changes with respect to the externally imposed strain. Several detailed studies of the PL change/decrement from InGaAs/GaAs QDs and InAs/GaAs QDs under hydrostatic pressure have been reported [4-7]. Lyapin [6] attributed the decrement of PL intensity to the crossover between the Γ-band energy confined in the InGaAs/GaAs QD and the X-band energy in the matrix. Compared to the hydrostatic pressure experiment, nanoprobe indentation induces inhomogeneous strain fields in the vicinity of the probe tip, including biaxial and shear strains [13]. As a result, the mechanism of PL quenching under nanoprobe indentation might differ from that under hydrostatic pressure. The PL quenching in the InGaAs/GaAs QDs was also observed under the indentation of a rounded-apex probe by Ozasa *et al* [12]. In their report, the PL quenching was elucidated to be caused by the de-tuning of the position of hole-accumulation from the QDs layer depth with indentation force. In the case of using a flat-apex probe, however, the photoexcited holes were accumulated to the region under the probe edge, and the hole-accumulation increased monotonically with

indentation force [13, 20]. Therefore, this mechanism can be excluded in our present experiment. Robinson [8] and Johnson [9] have reported the quenching of PL in InAlAs/AlGaAs QDs induced by the indentation of a flat-apex nanoprobe. In the former work [8], possible mechanisms for the PL quenching, such as the direct-to-indirect gap transition (including $\Gamma - X$ crossover), the potential gradient and the valence band mixing were discussed. Unfortunately, information on strain fields and the strained band structures was lacking; thus, it was hard to investigate the mechanisms quantitatively. In the latter work [9], generation of dislocation was assumed to be responsible for the PL quenching. However, the generation of dislocation was not elucidated in their study, and their results do not agree with the observation in our previous experiment that both loading and unloading indentation processes show elastic characteristics [13], as also discussed in Fig. 3.2. In the case of dislocation, no symmetrical reversion of PL peak would show up in the unloading diagram in Fig. 3.2. Therefore, generation of dislocation, as quoted in Ref.9, is excluded as the mechanism for the PL quenching observed in the present study.

In this chapter, we discuss the mechanism of PL quenching observed in InGaAs/GaAs QDs under the indentation of a flat cylindrical nanoprobe, as $\Gamma - X / \Gamma - L$ crossover of InGaAs or electron-repulsion resulting from the indentation-induced potential gradient. The experimentally observed quenching force was found to vary from QD to QD under the indentation, as discussed in Fig. 3.4. This variation can be related to the location of each QD relative to the probe. In order to figure out the PL quenching mechanism, we focused on the energy levels of the conduction/valence bands with the effect of superposed strains. Comparison of the experimental and simulation results indicated that the $\Gamma - X / \Gamma - L$ crossover of InGaAs, based on the assumption of low $X - / L -$ band gap energy of InAs and high bowing parameter for the $X - / L -$ band gap energy of InGaAs, or electron-repulsion resulting from the indentation-induced potential gradient is the possible mechanism responsible for the observed PL quenching.

6.2 Calculation of the edge energies of conduction bands of strained InGaAs and GaAs

With the stationary indentation of the flat cylindrical nanoprobe (R=600 nm), as discussed in Sec. 3.1, the PL emissions from QDs were observed to be quenched when the indentation force was applied up to a relatively high value. The experimentally measured

quenching force, F_q, was found to vary from QD to QD (Fig. 3.4). This variation can be related to the location of each QD relative to the probe center, deducing the dependence of quenching force on the QD location, by using the estimation method of QD location proposed in Sec. 5.2. The most possible mechanisms responsible for the observed PL quenching under the nanoprobe indentation, as mentioned above, are the $\Gamma - X$ / $\Gamma - L$ crossover and the electron-repulsion resulting from the strain-induced potential gradient. In order to discuss these two possible mechanisms, we calculated the edge energies of the conduction bands of strained InGaAs and GaAs.

The conduction band edges of strained InGaAs and GaAs (E_c^{Γ}, E_c^{X}, and E_c^{L}) with the effect of superposed strains are calculated as

$$E_c^{(\Gamma,X,L)} = VBO + E_g^{(\Gamma,X,L)} + \Delta\overline{E}_c^{(\Gamma,X,L)}, \tag{6.1}$$

where VBO is the valence band offset as listed in Table 4.2, $E_g^{(\Gamma,X,L)}$ are the band gap energies of unstrained InGaAs and GaAs, and $\Delta\overline{E}_c^{(\Gamma,X,L)}$ are the energy shifts of each conduction band resulting from the superposed strain. The values of $\Delta\overline{E}_c^{(\Gamma,X,L)}$ were obtained based on volume averaging as described in Equation (4.10). The band gap energies $E_g^{(\Gamma,X,L)}$ of unstrained GaAs are determined with great precision on the basis of experiment [22], while those of unstrained InGaAs are usually derived from the corresponding values of InAs and GaAs taking into account the bowing parameters. The derivation is written as [23]

$$E_g^{(\Gamma,X,L)}(\mathrm{In}_{0.52}\mathrm{Ga}_{0.48}\mathrm{As}) = 0.52E_g^{(\Gamma,X,L)}(\mathrm{InAs}) + 0.48E_g^{(\Gamma,X,L)}(\mathrm{GaAs}) - 0.52\times 0.48\times C_{(\Gamma,X,L)}, \tag{6.2}$$

where $C_{(\Gamma,X,L)}$ are the bowing parameters of the Γ, X, and L band gaps. The values of $E_g^{(X,L)}(\mathrm{InAs})$ have not yet been experimentally confirmed, partly because of the structural phase transition of bulk InAs under the high pressure [24]. Concerning the bowing parameters, the value of $C_{\Gamma} = 0.477$ eV agrees well with the recent experimental results [25-28]. The values of C_X and C_L, however, show large differences when predicted by different methods ($C_X = 1.40$ eV, $C_L = 0.72$ eV[29], $C_X = 0.08$ eV, $C_L = 0.50$ eV [30]). Since there are no reliable estimates for $E_g^{(X,L)}(\mathrm{InAs})$ and $C_{(X,L)}$, we will examine the cases of different

predictions of $E_g^{(X,L)}$(InAs) , and regard the bowing parameters of the X and L band gaps for InGaAs as fitting parameters in this study.

6.3 Direct-to-indirect transitions

Considering the conduction-band crossover, it is either the $\Gamma - X$ / $\Gamma - L$ crossover of bulk InGaAs (Γ (InGaAs) $- X$ (InGaAs)/ Γ (InGaAs) $- L$ (InGaAs) crossover) or the crossover between the Γ-band energy confined in the QD and the X-/L- band energy in the matrix (Γ (QD) $- X$ (GaAs)/ Γ (QD) $- L$ (GaAs) crossover). Both types of crossovers cause the optical direct-to-indirect transition, leading to the quenching of PL. We deduced that the former type is the possible crossover in our indentation experiment.

E_g^X (InAs)=1.43 eV, E_g^L (InAs)=1.13 eV [23, 29], $C_X = 1.05$ eV and $C_L = 0.70$ eV were selected to decide the energy levels of the X and L bands of strained InGaAs. This selection makes the simulated $\Gamma - X$ / $\Gamma - L$ crossover agree well with the present experimental observation of PL quenching within possible ranges of the parameters, as will be explained below. Figure 6.1 is a plot of the dependence of the Γ, X, and L band edge energies (E_c^Γ, E_c^X, and E_c^L) of bulk InGaAs on QD location d at $\theta = 0^\circ$ under the effect of superposed strain. Modified by the negative hydrostatic strain, the Γ band is shifted upward, X band downward, and L band upward. In addition to the energy shift, the X and L bands are also split because of the biaxial and shear strains, respectively. The X band is split into three according to Equation (4.7). The band of $E_c^{X[010]}$ was proven to be the lowest X band as the contribution of $\bar{\varepsilon}_s$ to lower the energy was significant. The L band is split into two according to Equation (4.8), because the shear strain components $\bar{\varepsilon}_{xy}$ and $\bar{\varepsilon}_{yz}$ are almost zero in the QD. The bands of $E_c^{L[111]} = E_c^{L[1\bar{1}1]}$ are the lowest L band due to the downward energy shift induced by $\bar{\varepsilon}_{xz}$. The Γ band edge energy at non-zero indentation force decays dramatically for the QDs around the nanoprobe edge, while the X band energy is almost homogenous for all QDs (Fig. 6.1). This almost homogenous distribution of the X band edge energy is caused by the combined effect of the hydrostatic strain $\bar{\varepsilon}_h$ and biaxial strain $\bar{\varepsilon}_s$ (Fig. 4.4). The L band edge energy was modified mainly by the hydrostatic strain $\bar{\varepsilon}_h$ for the QDs around the probe center but modified by the shear strain $\bar{\varepsilon}_{xz}$ for the QDs

around the edge. Moreover, in Fig. 6.1, the Γ band edge energy E_c^{Γ} crosses over the X or L band edge energy E_c^{X} or E_c^{L} around the nanoprobe edge under the effect of superposed strains, namely $\Gamma - X$ or $\Gamma - L$ crossover, written as

$$E_c^{\Gamma} \geq E_c^{X} \quad \text{or} \quad E_c^{\Gamma} \geq E_c^{L}. \tag{6.3}$$

The point where the band energies intersect is defined as the crossover point. The $\Gamma - X$ and $\Gamma - L$ crossovers provide the thresholds that decide whether the PL emitted from the QD is quenched or not, i.e., direct to indirect transition, respectively. Taking, for example, the $\Gamma - X$ crossover under an indentation force of 2.0 mN, the PL emitted from the QDs that are located inside the area around the crossover point is quenched. With the increment of the indentation force, the distance of the QD from the nanoprobe center at the $\Gamma - X$ crossover point increases (Fig. 6.1 (a)). In Fig. 6.1 (b), two crossover points appear for the $\Gamma - L$ crossover under an indentation force because of the sharp peak of $\bar{\varepsilon}_{xz}$ distribution under the probe edge. The distance of the QD from the nanoprobe center at one crossover point increases while the other decreases with increasing indentation force. These changes of the distance of the QD from the prober center at the $\Gamma - X$ and $\Gamma - L$ crossover points with the indentation force could be the mechanism for the relationship between quenching force and blueshift rate observed experimentally (Fig. 3.4). We obtained the simulated $\Gamma - X$ and $\Gamma - L$ crossover results (quenching force versus QD location) as the boundaries of direct (Γ)-to-indirect (X or L) transitions by tracing the crossover points under continuous change of the indentation force.

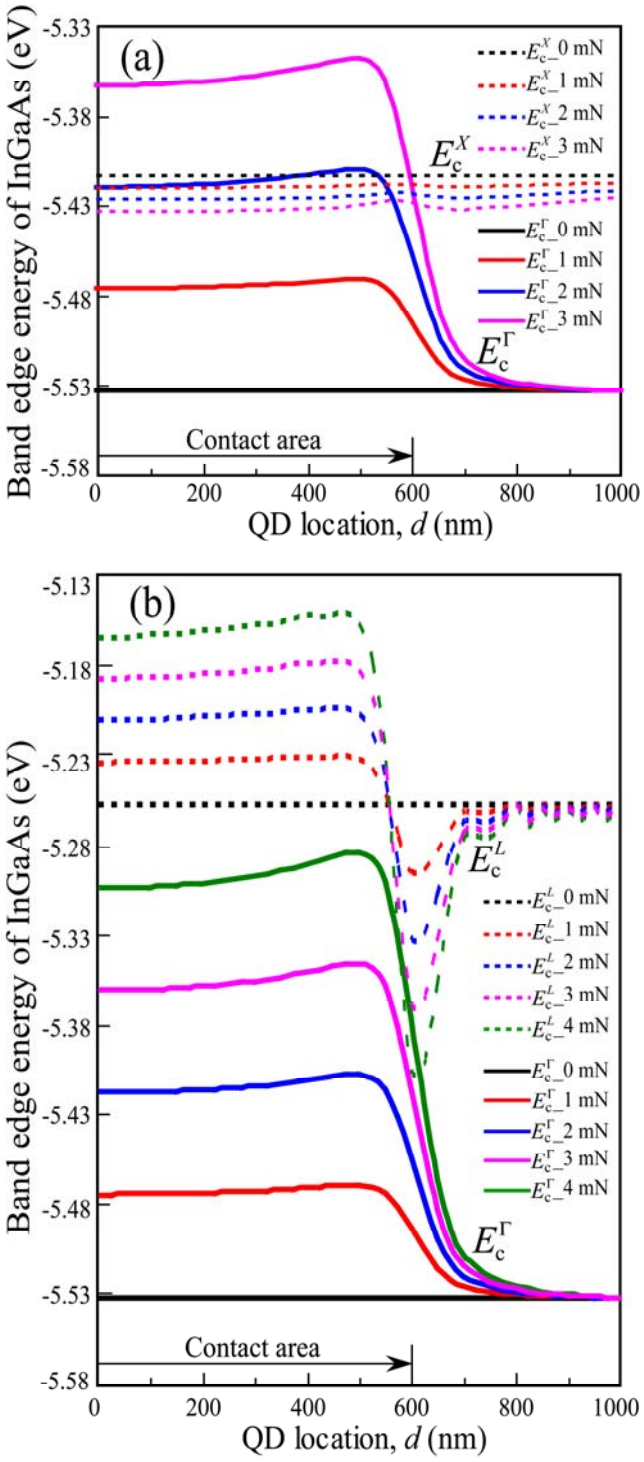

FIG. 6.1 Dependence of (a) Γ and X band-edge-energies, and (b) Γ and L band-edge-energies of bulk InGaAs due to the superposed strain on QD location d for $\theta = 0^\circ$, based on the volume-averaged energy shifts. The indentation forces were set to be 1 mN, 2 mN, 3 mN and 4 mN, and 0 mN represented the lattice-mismatched state. The bowing parameters of the X and L band gaps for InGaAs are set as $C_X = 1.05$ eV and $C_L = 0.70$ eV. The nanoprobe radius is 600 nm.

The simulated $\Gamma - X$ and $\Gamma - L$ crossovers obtained above were compared to the experimental results of PL quenching (Fig. 6.2). As shown in Fig. 6.2, the experimental data indicate a positive trend: the quenching force increases as the QD location relative to the probe center increases. The simulated $\Gamma - X$ or $\Gamma - L$ crossover is given with a range of the bowing parameter. The uncertainty in the other parameters (such as the deformation potentials) also contributes to the range of the $\Gamma - X / \Gamma - L$ crossover, but with a minor contribution compared to the bowing parameters. Both of the $\Gamma - X$ and $\Gamma - L$ crossovers are affected by the factor θ (Fig. 6.2). These crossovers provide the boundaries of direct (Γ) to indirect (X or L) transitions, as presented in Fig. 6.1. Therefore, the direct or indirect transition can be determined with a combination of $\Gamma - X$ and $\Gamma - L$ crossovers including the effect of θ, as shown in Fig. 6.2. The $\Gamma - X$ crossover agrees well with the experimental data by fitting the bowing parameter of the *X* band gap for InGaAs to the value of 0.90 — 1.20 eV. We note that part of the simulated $\Gamma - L$ crossover, especially at $\theta = 45^\circ$, is involved in the range of $\Gamma - X$ crossover with the QD location $d / R \geq 1.0$. In other words, the L band edge energy is close or equal to the energy of the X band for strained InGaAs at $d / R \geq 1.0$. As a result, both $\Gamma - X$ and $\Gamma - L$ crossovers could be the mechanism of PL quenching for the QDs located outside the nanoprobe edge. The same analysis in the case of E_g^X(InAs)=2.00 eV, E_g^L(InAs)=1.43 eV [30] indicated a pair of fitted bowing parameters of $C_X = 2.05 \sim 2.30$ eV and $C_L = 1.20 \sim 1.30$ eV, which exceed the possible ranges of the theoretical estimates. We also evaluated the minimum indentation forces required to achieve the Γ(QD) $- X$(GaAs) crossover and Γ(QD) $- L$(GaAs) crossover to be approximately $F_q = 4.7$ mN at $d / R = 0.9$ and $F_q = 5.1$ mN at $d / R = 1.0$ respectively. These values are far larger than the quenching force obtained in our experiment (Fig. 3.4, Fig. 6.2). Therefore, the Γ (InGaAs) $- X$ (InGaAs)/ Γ (InGaAs) $- L$ (InGaAs) crossover (assuming low $E_g^{(X,L)}$(InAs) and high $C_{(X,L)}$), rather than the Γ(QD) $- X$(GaAs)/ Γ(QD) $- L$(GaAs) crossover, is one of the possible mechanisms of PL quenching in our nanoprobe indentation.

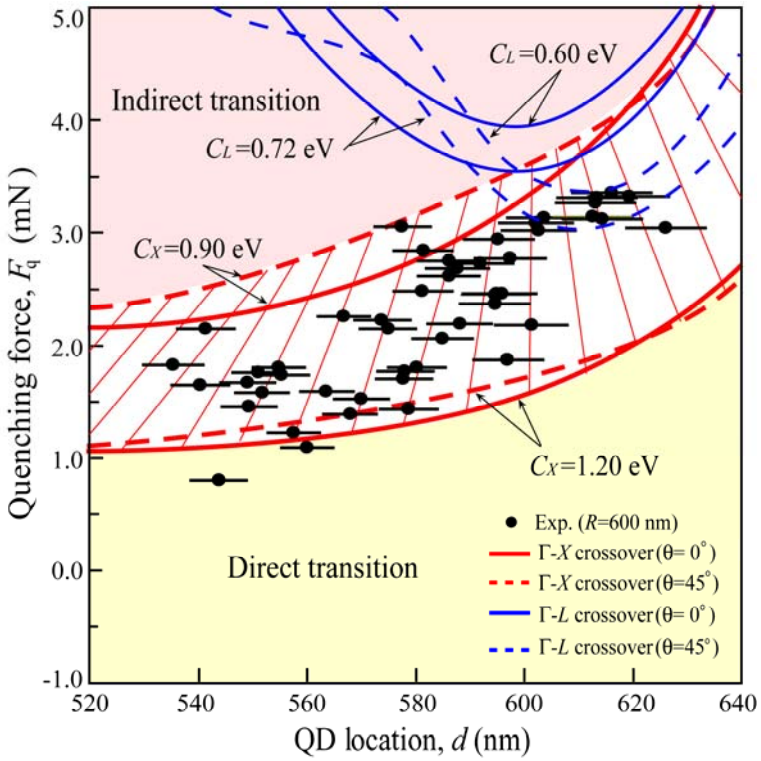

FIG. 6.2 Comparison of the experimental results to the simulated $\Gamma - X$ and $\Gamma - L$ crossover results. The symbols represent the experimental results which are plotted with an error bar in the QD location ($\theta = 0^\circ \sim 45^\circ$). The $\Gamma - X$ or $\Gamma - L$ crossover result is given with a range derived from the simulation with uncertainty of the bowing parameter. The crossovers with solid curve are for the QDs at $\theta = 0^\circ$ while those with dashed curve are for $\theta = 45^\circ$. The bowing parameter C_X for the $\Gamma - X$ crossover is from 0.90 (upper curve) to 1.20 (lower curve) eV, and the bowing parameter C_L for the $\Gamma - L$ crossover is from 0.60 (upper curve) to 0.72 (lower curve) eV.

As analyzed above, the $\Gamma - X$ crossover explains the experimental PL quenching well on the basis of a low E_g^X(InAs) and a large bowing parameter C_X (Fig. 6.2). There is a contrary argument that the position of the X-band in InGaAs/GaAs QD can't be so low, because the experimental result of the pressure-induced $\Gamma - X$ crossover in InGaAs/GaAs QD is similar to that of InAs/GaAs QD [6]. Their argument stands for a large E_g^X(InAs), i.e., higher X-band edge of unstrained InAs than GaAs (such as E_g^X(InAs) = 2.27 eV in Ref. 31), and therefore deduces a large value of E_g^X(InGaAs) (small bowing parameter C_X). The deduced high level of the X-band in InGaAs/GaAs QD may decrease the possibility of

Γ (InGaAs) – X (InGaAs) crossover to be the mechanism of PL quenching observed in this study.

6.4 Electron-repulsion resulting from the indentation-induced potential gradient

We now discuss another possible mechanism of PL quenching, the electron-repulsion resulting from the strain-induced potential gradient. As analyzed in Fig. 4.4, inhomogeneous strain fields are induced by the nanoprobe indentation (flat cylindrical nanoprobe). These strain fields modify the energy levels of the Γ -conduction band and valence band of bulk GaAs with a dependence on the QD location, as shown in Fig. 6.3. The GaAs within a thin layer of 5-nm thickness surrounding the QD was considered. As shown in Fig. 6.3, a large gradient of the electron potential in the GaAs matrix is induced under the probe edge by the hydrostatic strain in Fig. 4.4. Because of this potential gradient, the optically excited electrons outside the probe shadow were prevented from diffusing to the region beneath the probe (Fig. 2.5). As a result, the capture ratio of electrons by the QDs in the probe vicinity is reduced with the indentation force. On the other hand, very different strain-induced potential change is experienced by holes, as shown in Fig. 6.3. The holes are accumulated in the deep potential peak in the QDs located under the probe edge, because of the shear strain $\bar{\varepsilon}_{xz}$ in Fig. 4.4. Both of the electron-repulsion and the hole-accumulation increase continuously with the increment of the indentation force. At low indentation force, the predominant effect of the hole-accumulation enhances the PL intensity emitted from the QDs. At high indentation force, however, the electron-repulsion becomes dominant, leading to a lack of electrons in the QDs in the probe vicinity. As a result, the recombination of electrons and holes from the QDs will be reduced, experimentally observed as the decrement of the PL intensity or the quenching of PL.

Based on the linear dependence of the energy shift of Γ -conduction band on the indentation force, we calculated the indentation-induced potential height (indentation-induced energy shift of the Γ -conduction band of bulk GaAs) at quenching for the observed QDs in Fig. 3.4 and plotted the experimental data in Fig. 6.3. According to the experimental data, an indentation-induced potential height (P.H.) at quenching from 43.5 to 133.5 meV was derived. In other words, the PL emissions from QDs may probably be quenched when the

indentation-induced energy shift of the Γ -conduction band of bulk GaAs reaches the value of 43.5 ~ 133.5 meV, because of the electron-repulsion resulting from the potential gradient.

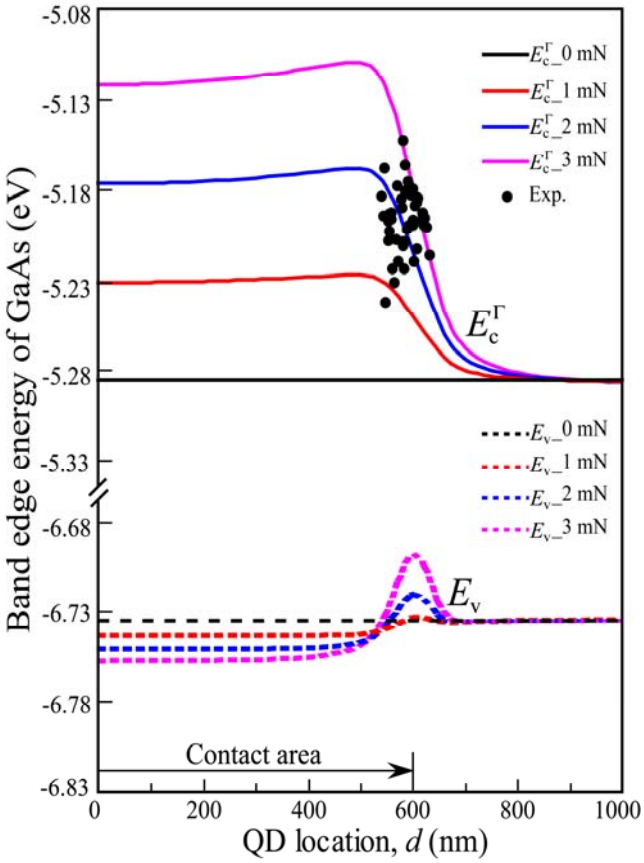

FIG. 6.3 Dependence of the Γ -conduction and valence band edge energies of bulk GaAs on QD location with the effect of superposed strains (0 mN, 1mN, 2 mN, 3 mN). The GaAs is selected as a 5-nm-thinckness layer surrounding the QD. The probe radius is 600 nm. The solid circles represent the experimental data.

Figure 6.4 shows the comparison of the experimental results to the simulation results of electron-repulsion resulting from the strain-induced potential gradient. The simulation results were derived from setting the indentation-induced potential height (P.H.) at quenching to be from 43.5 to 133.5 meV as obtained in Fig. 6.3. From Fig. 6.4, we can see that the mechanism of electron-repulsion due to the potential gradient agrees well with the experimental results, suggesting this mechanism to be probably responsible for the PL quenching observed in the stationary indentation of flat cylindrical nanoprobe.

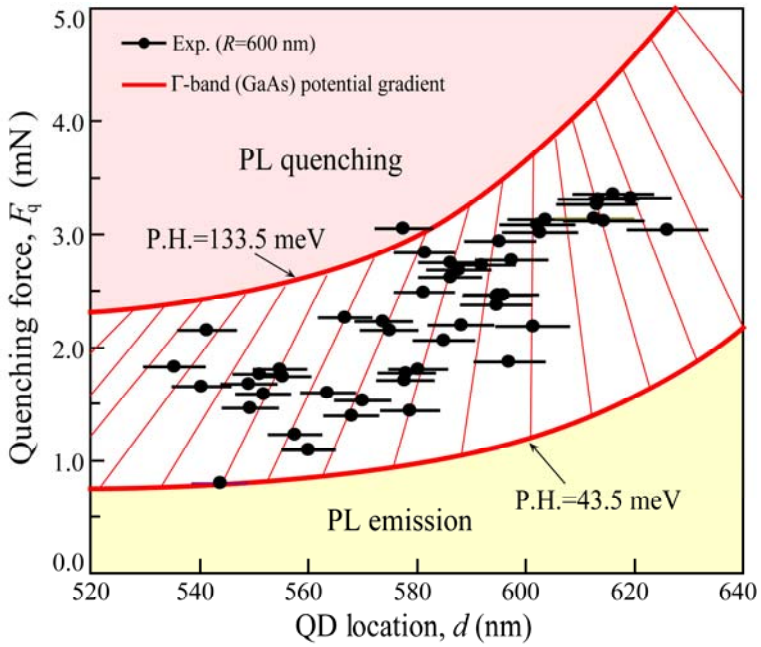

FIG. 6.4 Comparison of the experimental results to the simulation-derived electron-repulsion due to potential gradient. The symbols represent the experimental results which are plotted with an error bar in the QD location ($\theta = 0^{\circ} \sim 45^{\circ}$). The electron-repulsion due to potential gradient is given with a range of the indentation-induced potential height (P.H.) at quenching from 43.5 to 133.5 meV.

As analyzed in Fig. 6.2 and 6.4, two possible mechanisms, the Γ-*X* crossover of InGaAs and the electron-repulsion resulting from the indentation-induced potential gradient, are probably responsible for the PL quenching (Fig. 3.4), since both mechanisms explain well the experimentally obtained dependence of quenching force on the QD location. Using the flat cylindrical nanoprobe, it is hard to determine which one of these two possible mechanisms is the exact cause of PL quenching. This is because the distribution of the *X*-conduction band edge is almost homogeneous with the QD location under the combined effect of hydrostatic and biaxial strains, as shown in Fig. 6.1 (a). As a result, the dependence of quenching force on the QD location due to Γ-*X* crossover is mainly controlled by the distribution of the Γ-conduction band edge, which is also the case of electron-repulsion due to potential gradient. Therefore, the result of Γ-*X* crossover of InGaAs exhibits similar dependence of quenching force on QD location as that of electron-repulsion, as shown in Fig. 6.2 and 6.4.

6.5 Summary

In conclusions, we observed the quenching of PL emitted from InGaAs/GaAs QDs under the indentation of a flat cylindrical nanoprobe. The experimentally obtained variation of the quenching force can be related to the QD location relative to the probe center, which was determined through the experimentally measured blueshift rate with a simulated relationship between the blueshift rate and QD location. Based on the quantitative analysis of the indented strain fields and the modifications of the band structures resulting from the strains, the experimentally observed PL quenching can be ascribed to two possible mechanisms, the Γ (InGaAs) versus X (InGaAs) and L (InGaAs) crossovers and the electron-repulsion induced by the potential gradient in the GaAs matrix. The mechanism of $\Gamma(\text{InGaAs}) - X(\text{InGaAs}) / \Gamma(\text{InGaAs}) - L(\text{InGaAs})$ crossover was derived to be possible only based on the assumption of low $E_g^{(X,L)}(\text{InAs})$ and high bowing parameter $C_{X,L}$. On the other hand, if the electron-repulsion resulting from the strain-induced potential gradient was responsible for the PL quenching, an indentation-induced potential height at quenching was deduced to be from 435. to 133.5 meV. The simulation revealed that the large inhomogeneous hydrostatic strain generated around the nanoprobe edge by indentation plays an important role in the PL quenching through the $\Gamma - X / \Gamma - L$ crossover or the electron-repulsion due to the potential gradient.

References

[1] L. B. Freund, and H. T. Johnson, "*Influence of strain on functional characteristics of nanoelectronic devices*", Journal of the Mechanics and Physics of Solids 49, 1925-1935 (2001).

[2] R. Santoprete, Belita Koiller, R. B. Capaz, P. Kratzer, Q. K. K. Liu, and M. Scheffler, "*Tight-binding study of the influence of the strain on the electronic properties of InAs/GaAs quantum dots*", Physical Review B 68, 235311 (2003).

[3] C. Cornet, A. Schliwa, J. Even, F. Dore, C. Celebi, A. Letoublon, E. Mace, C. Paranthoen, A. Simon, P. M. Koenraad, N. Bertru, D. Bimberg, and S. Loualiche, "*Electronic and optical properties of InAs/InP quantum dots on InP(100) and InP(311) B substrates: Theory and experiment*", Physical Review B 74, 035312 (2006).

[4] G. H. Li, A. R. Goni, K. Syassen, O. Brandt, and K. Ploog, "*State mixing in InAs/GaAs quantum dots at the pressure-induced Γ-X crossing*", Physical Review B 50(24), 18420 (1994).

[5] I. E. Itskevich, S. G. Lyapin, I. A. Troyan, P. C. Klipstein, L. Eaves, P. C. Main, and M. Henini, "*Energy levels in self-assembled InAs/GaAs quantum dots above the pressure-induced Γ-X crossover*", Physical Review B 58(8), R4250 (1998).

[6] S. G. Lyapin, I. E. Itskevich, I. A. Trojan, P. C. Klipstein, A. Polimeni, L. Eaves, P. C. Main, and M. Henini, "*Pressure-Induced Γ-X Crossover in Self-Assembled In(Ga)As/GaAs Quantum Dots*", Physica Status Solid (b) 211, 79 (1999).

[7] I. E. Itskevich, M. S. Skolnick, D. J. Mowbray, I. A. Trojan, S. G. Lyapin, L. R. Wilson, M. J. Steer, M. Hopkinson, L. Eaves, and P. C. Main, "*Exited states and selection rules in self-assembled InAs/GaAs quantum dots*", Physical Review B 60(4), R2185 (1999).

[8] H. D. Robinson, M. G. Muller, B. B. Goldberg, and J. L. Merz, "*Local optical spectroscopy of self-assembled quantum dots using a near-field optical fiber probe to induced a localized strain field*", Applied Physics Letters 72(17), 2081 (1998).

[9] H. T. Johnson, and R. Bose, "*Nanoindentation effect on the optical properties of self-assembled quantum dots*", Journal of the Mechanics and Physics of Solids 51, 2085-2104 (2003).

[10] A. M. Mintairov, K. Sun, J. L. Merz, C. Li, A. S. Vlasov, D. A. Vinokurov, O.V. Kovalenkov, V. Tokranov, and S. Oktyabrsky, "*Nanoindentation and near-field spectroscopy of single semiconductor quantum dots*", Physical Review B 69, 155306 (2004).

[11] Kazunari Ozasa, Sintaro Nomura, and Yoshinobu Aoyagi, "*Pressure effects on nanoprobe photoluminescence of quasi-zero-dimensional confinement quantum dots*", Superlattices and Microstructures 30, 169-179 (2001).

[12] Kazunari Ozasa, Yoshinobu Aoyagi, Akihiko Yamane, and Yoshio Arai, "*Enhanced photoluminescence of InGaAs/GaAs quantum dots induced by nanoprobe pressure effects*", Applied Physics Letters 83(11), 2247 (2003).

[13] Kazunari Ozasa, Mizuo Maeda, Masahiko Hara, Masane Ohashi, Yuan-Hua Liang, Hiroki Kakoi, and Yoshio Arai, "*Localized strain effects on photoluminescence of quantum dots induced by nanoprobe indentation*", Physica E 40, 1920-1923 (2008).

[14] Stefan Seidl, Martin Kroner, Alexander Hogele, Khaled Karrar, Richard J. Warburton, Antonio Badolato, and Pierre M. Petroff, "*Effect of uniaxial stress on excitons in a self-assembled quantum dot*", Applied Physics Letters 88, 203113 (2006).

[15] S. Seidl, A. Hogele, M. Kroner, K. Karrai, A. Badolato, P. M. Petroff, and R. J. Warburton, "*Tuning the cross-gap transition energy of a quantum dot by uniaxial stress*", Physica E 32, 14-16 (2006).

[16] Susumu Noda, Tomoki Abe, and Masatoshi Tamura, "*Mode assignment of excited states in self-assembled InAs/GaAs quantum dots*", Physical Review B 58(11), 7181 (1998).

[17] H. L. Wang, F. H. Yang, S. L. Feng, H. J. Zhu, D. Ning, H. Wang, and X. D. Wang, "*Experimental determination of local strain effect on InAs/GaAs self-organized quantum dots*", Physical Review B 61(8), 5530 (2000).

[18] A. R. Goni, C. Kristukat, F. Hatami, S. Dressler, W. T. Masselink, and C. Thomsen, "*Electronic structure of self-assembled InP/GaP quantum dots from high-pressure photoluminescence*", Physical Review B 67, 075306 (2003).

[19] Yuan-Hua Liang, Yoshio Arai, Kazunari Ozasa, Masane Ohashi, and Eiichiro Tsuchida, "*Simultaneous measurement of nanoprobe indentation force and photoluminescence of InGaAs/GaAs quantum dots and its simulation*", Physica E 36, 1-11 (2007).

[20] Yuan-Hua Liang, Masane Ohashi, Yoshio Arai, and Kazunari Ozasa, "*Location of quantum dots identified by microscopic photoluminescence changes during nanoprobe indentation with a horizontal scan*", Physical Review B 75, 195318 (2007).

[21] Tao Yang, Jun Tatebayashi, Masao Nishioka, and Yasuhiko Arakawa, "*Effects of accumulated strain on the surface and optical properties of stacked 1.3 μm InAs/GaAs quantum dot structures*", Physica E 40, 2182-2184 (2008).

[22] D. E. Aspnes, "*GaAs lower conduction-band minima: Ordering and properties*", Physical Review B 14(12), 5331(1976).

[23] I. Vurgaftman, J. R. Meyer, and L. R. Ram-Mohan, "*Band parameters for Ⅲ-Ⅴ compound semiconductors and their alloys*", Journal of Applied Physics 89(11), 5815 (2001).

[24] G. D. Pitt and M. K. R. Vyas, "*Electrical properties of InAs to very high pressures*", Journal of Physics C: Solid State Physics 6, 274(1973).

[25] Sajal Paul, J. B. Roy, and P. K. Basu, "*Empirical expressions for the alloy composition and temperature dependence of the band gap and intrinsic carrier density in* $Ga_xIn_{1-x}AS$", Journal of Applied Physics 69, 827 (1991).

[26] Dong-Su Kim, Stephen R. Forrest, Michael J. Lange, Marshall J. Cohen, Gregory H. Olsen, Ray J. Menna, and Richard J. Paff, "*Study of* $In_xGa_{1-x}As/InAs_yP_{1-y}$ *structures lattice mismatched to InP substrates*", Journal of Applied Physics 80, 6229 (1996).

[27] J. R. Jensen, J. M. Hvam, and W. Langbein, "*Optical properties of InAlGaAs quantum wells: Influence of segregation and band bowing*", Journal of Applied Physics 86(5), 2584 (1999).

[28] Z. Hang, D. Yan, Fred H. Pollak, G. D. Pettit and J. M. Woodall, "*Temperature dependence of the direct band gap of* $In_xGa_{1-x}As$ *(x=0.06 and 0.15)*", Physical Review B 44(19), 10546 (1991).

[29] Sadao Adachi, "*Band gaps and refractive indices of AlGaAsSb, GaInAsSb, and InPAsSb: Key properties for a variety of the 2-4* μ*m optoelectronic device applications*", Journal of Applied Physics 61, 4869 (1987).

[30] Sandip Tiwari, and David J. Frank, "*Empirical fit to band discontinuities and barrier heights in Ⅲ-Ⅴ alloy systems*", Applied Physics Letters 60, 630 (1992).

[31] A. J. Williamson, and Alex Zunger, "*Effect of interfacial states on the binding energies of electrons and holes in InAs/GaAs quantum dots*", Physical Review B 58(11), 6724 (1998).

Chapter 7
Conclusions and recommendations for future work

7.1 General conclusions

InGaAs/GaAs quantum dots, grown by self-assembling Stranski-Krastanow techniques, have attracted lots of interest in recent years due to their 3-dimensional confinement effect and very high radiative efficiency, close to 100%. They have been widely applied in the electronic and optoelectronic devices, such as semiconductor lasers, light emitting diodes, single electron transistors, infrared detectors and etc. During the self-assembling organization, strains are inevitably created in QD in order to release the strain energy between the lattice-mismatched two semiconductors, resulting in the significant influence of generated strains on the electronic and optical properties of QDs, thus on the performance of QD-based devices. Therefore, the study of the strain effect on QDs properties is of great importance. To investigate the strain effects on QDs, one of the most efficient means is to measure the PL emissions from QDs under the nanoprobe indentation, since inhomogeneous strain fields are introduced through the indentation and the measured PL emissions from QDs provide direct information on the consequence of strain on the QDs. Compared to the previous literatures [1-8], our research group has made significant improvements [9] in the nanoprobe indentation, including to fabricate the probe apex well with the FIB technique, to simultaneously collect the PL emissions from QDs as well as to preciously measure the applied indentation force with a high-sensitivity loadcell. These improvements enabled us to investigate the strain effects on the QDs electronic and optical properties quantitatively. On the other hand, the simulation of 3-dimensional strain fields have been realized by applying the finite element method, and the strained band structures were calculated based on the deformation potential theory. The calculation results agreed well with the experimentally measured shifts of PL emissions. By comparing the simulation/experimental results, the location of single QD has been for the first time identified [10]. Furthermore, we made it clear that only the PL emissions from those QDs located under the probe edge were enhanced and observable [11], because the photoexcited holes were accumulated into the edge region with the effect of large

indentation-induced shear strain under the probe edge. In our previous studies [9-11], however, the quenching of PL emissions observed at relatively high force levels has not yet been examined. Although the effects of strains on the direct band edges have been clarified, the behavior of indirect band edges under strains has not yet been figured out. Moreover, only the probe with flat shape apex has been used for the indentation in the previous studies, while the effect of the tip shapes on the electronic and optical properties of QDs has not been studies.

By investigating the behavior of PL emissions from InGaAs/GaAs QDs under the indentation of a flat cylindrical or dome-shaped probe, we made further study on the strain effect on the QDs electronic and optical properties, based on our previous researches. Different types of indentation experiments, stationary indentation and scanning indentation, were designed for different purposes of research.

With the effect of strain fields induced by the indentation of a flat cylindrical or dome-shaped nanoprobe, PL emissions from InGaAs/GaAs QDs were remarkably enhanced. Under the stationary indentation of the flat cylindrical nanoprobe, the enhanced fine PL peak from single QD was observed to be linearly blueshifted with the indentation force, the shift rate of which was measured to be different from QD to QD. On the other hand, the intensity of PL peak of single QD first increased, then decreased and finally disappeared with the indentation force. The measured quenching force, at where the integrated PL intensity became zero, was also found to vary from QD to QD, and therefore can be related to the location of individual QD, which can be determined from the measured blueshift rate of PL emission. With the *y*-scan indentation performed by using the dome-shaped probe, the obtained PL result exhibited characteristics different from that with the scanning indentation of flat cylindrical nanoprobe, since different strain fields were generated under the indentation of dome-shaped probe compared to the flat cylindrical probe case. By analyzing this *y*-scan result, the locations of some of observed QDs were directly derived from the experiment, at where the PL emissions achieved the maximum values.

In order to quantitatively explain the behavior of PL emissions observed in the indentation experiments, the simulation of 3-dimensional strain fields, induced by the lattice mismatch and nanoprobe indentation, in and around a single QD was carried out by employing finite element method. Highly localized strain fields were found to be generated within the contact effective area, either in the case of flat cylindrical probe or dome-shaped

probe. In the flat cylindrical probe case, almost homogeneous strain field was induced under the nanoprobe center, and this strain field dramatically decayed to zero outside the probe edge. The change of the tip shape from flat apex to dome-shaped probe resulted in the modification in the generated strain field. The strain field showed the maximum magnitude of strains at the probe center and decayed outside the center in the dome-shaped probe case. The difference in the generated strain fields by the flat cylindrical and dome-shaped probe led to the different behavior of PL emissions in the indentation experiment. Based on the obtained strain fields, the influence of strains on the band structures of QDs were evaluated according to the deformation potential theory. The calculation-derived blueshift rate, using the flat cylindrical nanoprobe, agreed well with the experimentally measured values in the stationary indentation.

With the simulated relationship between the blueshift rate and QD location, we proposed a new method for estimating the location of individual QD through the blueshift rate experimentally measured with the stationary indentation of flat cylindrical nanoprobe. This method has been proven to be equally reliable but much simpler compared to the method proposed in our previous study, in which the QD location was identified by comparing the simulation results and the energy shift of PL emission measured in the scanning indentation. All QDs observed with stationary indentation were determined to be located around the probe edge through the present method, agreeing with the previous results that only the PL emissions from QDs under the probe edge was enhanced and observable. The method proposed in this study provides a simple way to evaluate the location of single QD using nanoprobe indentation. By introducing localized strain fields using the dome-shaped nanoprobe, which is different from that by a flat cylindrical probe, we achieved an advantageous improvement in estimating the location of embedded InGaAs/GaAs QDs with nanoprobe indentation. The locations of some observed QDs in a *y*-scan were directly obtained from the PL results, at where the PL energies of those QDs reached the maximum values. This direct determination of QD location from the indentation experiment can not be achieved by using the flat cylindrical nanoprobe.

Based on the identification of the location of QDs observed with the stationary indentation of flat cylindrical nanoprobe, the mechanism of PL quenching was examined quantitatively by investigating the influence of strain on the indirect band edges as well as on the band edges of GaAs barrier. Two of four possible mechanisms as proposed in the previous literatures, dislocation and de-tuning of hole accumulation from the QD layer, were definitely

excluded as the mechanism for the PL quenching in this study. Both of the $\Gamma(\mathrm{InGaAs}) - X(\mathrm{InGaAs})$ / $\Gamma(\mathrm{InGaAs}) - L(\mathrm{InGaAs})$ crossover and the electron-repulsion resulting from the indentation-induced potential gradient were derived to be probably responsible for the observed PL quenching by comparing the experiment/simulation results. The mechanism of $\Gamma(\mathrm{InGaAs}) - X(\mathrm{InGaAs}) / \Gamma(\mathrm{InGaAs}) - L(\mathrm{InGaAs})$ crossover was found to be possible only on the basis of assuming low $E_g^{(X,L)}(\mathrm{InAs})$ and high bowing parameter $C_{X,L}$. Otherwise, the observed PL quenching couldn't be ascribed to the crossover. On the other hand, if the electron-repulsion resulting from the indentation-induced potential gradient was responsible for the PL quenching, an indentation-induced potential height at quenching from 43.5 to 133.5 meV can be deduced from the experimental results.

In summary, we have gained fruitful achievements in investigating the influence of strain on the electronic and optical properties of QDs by using nanoprobe indentation. The experimentally observed energy shift of PL emission from single QD was quantitatively analyzed, as well as the observed PL quenching, based on the 3-dimensional simulation of the strain field and the calculation of strained band structures according to the deformation potential theory. By comparing the experimentally measured energy shift of PL emission with the simulation results, we succeeded in determining the location of individual QD embedded in the GaAs matrix. The consequence of the change of probe tip shape in the PL emissions from QDs was also successfully evaluated, and we achieved an advantageous improvement in the location determination by using the dome-shaped nanoprobe. From the quantitative analysis of strained band structures, especially the indirect bands, we excluded several possible mechanisms for the PL quenching observed in this study, and ascribed it to two possible mechanisms, the $\Gamma(\mathrm{InGaAs}) - X(\mathrm{InGaAs}) / \Gamma(\mathrm{InGaAs}) - L(\mathrm{InGaAs})$ crossover and the electron-repulsion resulting from the indentation-induced potential gradient

7.2 Future work

However, there are still several unsolved topics in our present study.

1) Using the flat cylindrical nanoprobe, it is hard to determine which one of the two possible mechanisms, the $\Gamma(\mathrm{InGaAs}) - X(\mathrm{InGaAs})$ / $\Gamma(\mathrm{InGaAs}) - L(\mathrm{InGaAs})$ crossover or the electron-repulsion due to the indentation-induced potential gradient, is the exact mechanism responsible for the observed PL quenching,

since it is impossible to distinguish these two mechanisms based on the present study. The strained *X*-band edge energy of QDs remained almost constant with the QD location under the indentation of flat cylindrical nanoprobe with the combined effect of hydrostatic and biaxial strains, resulting in the similarity of the result of $\Gamma(\mathrm{InGaAs}) - X(\mathrm{InGaAs})$ crossover and electron-repulsion.

2) In Fig. 3.10, we only examined the locations of those QDs, whose PL emissions exhibited symmetric blue- and red-shifts with the movement of probe position. All the examined QDs were found to locate under the probe edge along the *x* direction, where the photoexcited holes were accumulated into. However, it is difficult to conclude that the reason for the enhancement and observability of PL emissions from QDs under the indentation of dome-shaped probe is still due to the hole-accumulation as in the case of flat cylindrical nanoprobe, since not all observed QDs were examined.

3) The influence of strain on the QDs PL emission was examined only for the InGaAs/GaAs QDs when the QDs sample was prepared with a constant capping layer depth (50 nm). The effect of the capping layer depth has not yet been clarified.

In order to solve the above listed topics and furthermore to improve the application of this study, the following works are recommended in the future:

1) To research the strained PL emissions from other types of QDs under nanoprobe indentation, such as the InAs/GaAs QDs. In the InAs/GaAs QDs, there is no such issue of bowing parameter as in the InGaAs QDs. Therefore, the mechanism of PL quenching under the nanoprobe indentation may probably be clarified.

2) To investigate the influence of experimental conditions on the PL results, such as modulating the excitation power density, changing the present collection mode into the illumination mode. The excitation power density may probably determine whether we can observe the redshift of PL energy or not after the blueshift in the stationary indentation. If we can observe the redshift in the stationary indentation, the reason for the decrement of PL intensity or the PL quenching is probably ascribed to the crossover. By changing the experimental setup from the collection mode into the illumination mode, in which the tip is used to optically excite the

sample locally and the PL is collected with far-field optics, the diffusion direction of the photoexcited carriers becomes inversed. Measuring the quenching force in both modes and comparing the measure quenching force, the exact quenching mechanism may probably be clear, since the crossover mechanism is not influenced by the carrier diffusion.

3) To carry out more detailed analysis in the case of dome-shaped probe and furthermore to employ the nanoprobe with other tip shapes like the rounded-apex probe. Since different strain fields are generated with the usage of nanoprobe of different tip shapes, the principle of PL enhancement, the location of observable QDs as well the mechanism of PL quenching may differ from each other. By modifying the *X*-band edge energy with a strong dependence on the QD location through introducing different strain field, it may probably be possible to distinguish the $\Gamma - X$ crossover and electron-repulsion mechanisms.

4) To examine the effect of the depth of capping layer by preparing the QDs sample with different capering layer depths.

5) To estimate the strain field in the QD through the information provided by the PL quenching. If we can determine the exact mechanism of PL quenching, it may be possible to estimate the strain field in the QD, since the quenching of PL emission provides some critical values of band energy level and thus reflects the strain field.

6) To seek for the possible applications of this study in the semiconductor material field and the mechanical field. By modulating the discrete energy levels in the QD through the introduction of external strain fields, the absorption or emission of photon with energy at various levels can be realized, leading to the prospect in improving the performance of present QD-based devices, such as the QDs solar cells, semiconductor lasers, light emitting diodes, single electron transistors, infrared detectors and etc, and developing new QD devices. Based on the strain engineering of semiconductors, the semiconductor materials also become the candidate for pressure sensors.

References

[1] H. D. Robinson, M. G. Muller, B. B. Goldberg, and J. L. Merz, "*Local optical spectroscopy of self-assembled quantum dots using a near-field optical fiber probe to induce a localized strain field*", Applied Physics Letters 72(17), 2081 (1998).

[2] A. Chavez-Pirson, J. Temmyo, and H. Ando, "*Pressure-induced modulation of the confinement in self-organized quantum dots produced and detected by a near-field optical probe*", Physica E 7, 367-372 (2000).

[3] Kazunari Ozasa, Sintaro Nomura, and Yoshinobu Aoyagi, "*Pressure effects on nanoprobe photoluminescence of quasi-zero-dimensional confinement quantum dots*", Superlattices and Microstructures 30(4), 169 (2001).

[4] Kazunari Ozasa, and Yoshinobu Aoyagi, "*Nanoprobe photoluminescence of quasi-zero-dimensional InGaAsP quantum dots*", Physica E 13, 212-215 (2002).

[5] H. T. Johnson, and R. Bose, "*Nanoindentation effect on the optical properties of self-assembled quantum dots*", Journal of the Mechanics and Physics of Solids 51, 2085-2104 (2003).

[6] Kazunari Ozasa, Yoshinobu Aoyagi, Akihiko Yamane, and Yoshio Arai, "*Enhanced photoluminescence of InGaAs/GaAs quantum dots induced by nanoprobe pressure effects*", Applied Physics Letters 83(11), 2247 (2003).

[7] A. M. Mintairov, K. Sun, J. L. Merz, C. Li, A. S. Vlasov, D. A. Vinokurov, O. V. Kovalenkov, V. Tokranov, and S. Oktyabrsky, "*Nanoindentation and near-field spectroscopy of single semiconductor quantum dots*", Physical Review B 69, 155306 (2004).

[8] Kazunari Ozasa, Yoshinobu Aoyagi, Masahiko Hara, Mizuo Maeda, Akihiko Yamane, and Yoshio Arai, "*Enhanced photoluminescence of InGaAs quantum dots induced by nanoprobe indentation*", Physica E 21, 265-269 (2004).

[9] Yuan-Hua Liang, Yoshio Arai, Kazunari Ozasa, Masane Ohashi, and Eiichiro Tsuchida, "*Simultaneous measurement of nanoprobe indentation force and photoluminescence of InGaAs/GaAs quantum dots and its simulation*", Physica E 36, 1-11 (2007).

[10] Yuan-Hua Liang, Masane Ohashi, Yoshio Arai, and Kazunari Ozasa, "*Location of quantum dots identified by microscopic photoluminescence changes during nanoprobe indentation with a horizontal scan*", Physical Review B 75, 195318 (2007).

[11] Kazunari Ozasa, Mizuo Maeda, Masahiko Hara, Masane Ohashi, Yuan-Hua Liang, Hiroki Kakoi, and Yoshio Arai, "*Localized strain effects on photoluminescence of quantum*

dots induced by nanoprobe indentation", Physica E 40, 1920-1923 (2008).